# Aeroelastic Tailoring of Composite Wings with High-Fidelity Aerodynamic Drag and Blending Constraints

Bordogna, M.T.

**DOI**
10.4233/uuid:63d60e4b-95e4-4a6a-ad59-79dcc4357623

**Publication date**
2024

**Document Version**
Final published version

**Citation (APA)**
Bordogna, M. T. (2024). *Aeroelastic Tailoring of Composite Wings with High-Fidelity Aerodynamic Drag and Blending Constraints*. [Dissertation (TU Delft), Delft University of Technology].
https://doi.org/10.4233/uuid:63d60e4b-95e4-4a6a-ad59-79dcc4357623

**Important note**
To cite this publication, please use the final published version (if applicable).
Please check the document version above.

# Aeroelastic Tailoring of Composite Wings with High-Fidelity Aerodynamic Drag and Blending Constraints

# Aeroelastic Tailoring of Composite Wings with High-Fidelity Aerodynamic Drag and Blending Constraints

## Dissertation

for the purpose of obtaining the degree of doctor

at Delft University of Technology,

by the authority of the Rector Magnificus,
prof. dr. ir. T.H.J.J. van der Hagen,

chair of the Board for Doctorates,

to be defended publicly on

Wednesday 4th of September 2024 at 12:30

by


## Marco Tito BORDOGNA

Master of Science in Mechanical Engineering,

Royal Institute of Technology (KTH), Sweden

born in Bergamo, Italy.

This dissertation has been approved by the promotors.

Composition of the doctoral committee:

| | | |
|---|---|---|
| Rector Magnificus, | Chairperson | |
| Dr. ir. R. De Breuker, | Promotor | Delft University of Technology |
| Prof. dr. C. Bisagni, | Promotor | Delft University of Technology |

Independent members:

| | |
|---|---|
| Dr. M. Cinefra | Politecnico di Bari, Italy |
| Prof. dr. ing. W.R. Krüger | Technische Universität Berlin / DLR, Germany |
| Prof. dr. J. Morlier | ISAE-SUPAERO, France |
| Prof. dr. F. Scarano | Delft University of Technology |
| Prof. dr. ir. R. Benedictus | Delft University of Technology, reserve member |

Other members:

| | |
|---|---|
| Dr. D. Bettebghor | ONERA / Schneider Electric, France |

*This research work was supported by Delft University of Technology, ONERA and the AMEDEO project, part of the European Union Seventh Framework Program and a Marie Curie Initial Training Network.*

*AMEDEO project partners:*

*Keywords:* Aeroelastic tailoring, Composite materials, Blending constraints, Surrogate model, Aerodynamic Drag

*Printed by:* Ipskamp Drukkers B.V., Enschede, The Netherlands

*Cover:* Design by Simon Binder



ISBN 978-94-6473-556-7

An electronic version of this dissertation is available at
http://repository.tudelft.nl/.

*To my grandparents Cicci, Gianni, Grazia and Tina.*

# PREFACE

Writing this thesis has been an incredible journey filled with numerous challenges, learning experiences, setbacks, and moments of personal and professional growth. As I look back to the path that led to the completion of my PhD, I am filled with immense gratitude.

First and foremost, I would like to express my deepest gratitude to my promotors, Roeland De Breuker and Chiara Bisagni, for their continuous support, guidance, and insightful comments on my dissertation. I would also like to thank my supervisor at ONERA, Dimitri Bettebghor, for his constant support and feedback throughout the years of my PhD.

I extend my sincere thanks to the chairperson, Dr. M. Cinefra, Prof. dr. ing. W.R. Krüger, Prof. dr. J. Morlier, Prof. dr. F. Scarano, and Prof. dr. Rinze Benedictus for accepting to be in my doctoral committee and for their valuable feedback on my dissertation.

My gratitude also extends to all the colleagues and researchers from the Department of Aerospace Structures and Materials (ASM) at TU Delft and from the Department of Modélisation et Simulation pour l'AéroElasticité (MSAE) at ONERA. I deeply appreciate the many conversations we had, your shared knowledge, professionalism, and support over these years. Additionally, working on the AMEDEO EU projects with numerous academic, research, and industrial partners was extremely enriching, and I thank everyone involved in the consortiums.

A big thank you to Christophe Blondeau for his patience and the many brainstorming sessions that were crucial throughout my PhD. Many thanks to Paul and Terence for the impactful work we did on structural optimization. Special thanks to Timothée for the day-to-day life at ONERA, the fun during conference trips, and your patience in teaching me French. Finally, I would like to acknowledge all the PhDs, post-docs, and friends I met during this journey: Andrea, il Presidente, Peppe, Ilias, Fabio, Rawan, Rocco, Quentin, Fabrizio, Kristofer, Jurij, Erik, Darwin, Javier, Ronan, Sebastian, Tigran, Mario, Ines, Marta, and many others I may have forgotten.

Most importantly, I would like to thank my parents. Your continuous support and encouragement in following my path wherever it led me have been invaluable.

Lastly, thanks to Giudi for always believing in me. None of this would have been possible without you. To Giorgio, whose fascination with planes and helicopters reminds me of my passion, and to our new arrival, for providing the hard deadline to finish my PhD.

# SUMMARY

Aircraft efficiency and its environmental impact are primarily influenced by three key areas: aircraft weight, aerodynamic efficiency, and engine performance. While engine performance is typically addressed as a separate topic, weight reduction and aerodynamic efficiency can be concurrently addressed by leveraging the directional stiffness properties of composite materials. This field is known as aeroelastic tailoring. Its potential applications have been studied since the '80s and have recently gained momentum, thanks to advancements in computational power and the widespread use of composite materials in aerospace.

In this dissertation, the author focuses on developing a framework for performing wing aeroelastic tailoring during the preliminary design phase of an aircraft. The framework's applicability to preliminary design studies favours the use of low-fidelity yet fast tools capable of computing thousands of different load cases used in wing design. The wing structure is modelled with FEM shell elements, allowing the direct inclusion of mechanical constraints in the optimization. The wing's main load-bearing structural components are divided into patches that are locally optimized to fully utilize the tailoring capabilities of composite materials. Aerodynamics is modelled using a fast panel method called the doublet lattice method (DLM). Composite materials and their directional stiffness characteristics are included in the optimizer via lamination parameters, allowing for gradient-based optimization. Structural continuity between adjacent wing patches is enforced through blending constraints, and their impact on the final design is thoroughly studied. Stacking sequence retrieval and the impact of blending constraints on the retrieval process are also explored.

Low-fidelity approaches inevitably involve simplifications limiting their applicability. Aerodynamic panel methods like the DLM, while fast, are unsuitable for estimating aircraft aerodynamic performance (e.g., drag). In this dissertation, CFD-based corrections to the DLM are implemented to capture the effect of airfoil camber and wing twist law on aerodynamic loads accurately. Additionally, a surrogate model is introduced to account for aerodynamic drag during optimization. The surrogate model relies on an original reduction technique to approximate wing structural deflection with a limited number of inputs. The resulting surrogate replaces costly high-fidelity CFD aero-structural simulations inside optimization loops, resulting in significantly faster simulations.

The proposed framework is built around the analysis and optimization capabilities of the commercial tool Nastran and has been applied to a real industrial case. Two main optimization cases have been performed. The first case focuses on three aspects: the impact of blending constraints on gradient-based optimization, the effect of blending constraints on subsequent stacking sequence retrieval, and the inclusion and impact of dynamic load cases on the final design. The use of blending constraints leads to a reduction in the design space followed by an approximately 5% increase in structural weight. However, these constraints enable more gradual thickness and stiffness changes between adjacent patches, resulting in a lower error (about 60%) when retrieving a discrete stacking sequence. This lower error ultimately leads to smaller corrections needed to achieve a fully feasible design and up to a 3.7% lighter final discrete design. Dynamic loads have been included in the optimizations via an Equivalent Static Load (ESL) method. Although dynamic loads have not been found to significantly impact the design under consideration, the ESL has demonstrated its capability to successfully include dynamic loads in an optimization.

The second optimization case focuses on multi-objective optimizations and trade-offs between weight and aerodynamic drag minimization, thanks to the inclusion of the surrogate model. The obtained Pareto fronts show that for structural weight minimization, the optimizer favours wing structures with wash-out behaviour and inward-shifted lift distribution. However, to maintain trim, the aircraft needs to fly at a higher angle of attack, increasing aerodynamic drag. Minimizing the drag coefficient results in a stiffer wing with less wash-out behaviour, allowing the aircraft to fly at a lower angle of attack. Validation of the results against full-order model CFD results shows an absolute error ranging between 0.9 and 1.6 d.c., in line with the surrogate model generalization RMSE of 1.29 d.c.

# SAMENVATTING

De efficintie van vliegtuigen en de resulterende milieu-impact ervan worden hoofdzakelijk bepaald door drie belangrijke factoren: het vliegtuiggewicht, de arodynamische efficintie en de voortstuwing. Dat laatste is vaak een aparte discipline, maar gewichtsvermindering en arodynamische efficintie kunnen samen worden geoptimaliseerd door de stijfheidsverdeling van composietmaterialen te bepalen. Dit onderzoeksgebied wordt aeroelastic tailoring genoemd. De potentile toepassing ervan wordt al sinds de jaren 1980 bestudeerd en zijn de laatste tijd in een stroomversnelling terechtgekomen dankzij betere computers en het wijdverbreide gebruik van composietmaterialen in de lucht- en ruimtevaart.

De auteur ontwikkelt een methode voor aroelastische optimalisatie van de vleugel tijdens de voorontwerpfase van een vliegtuig in dit proefschrift. Snelle rekenmethoden zijn nodig om deze methode rekenkundig haalbaar te maken omdat duizenden verschillende belastingsgevallen doorgerekend moeten worden tijdens het vleugelontwerp. De structuur van de vleugel wordt gemodelleerd met eindige elementen schaalmodellen die het mogelijk maken om mechanische randvoorwaarden mee te nemen in de optimalisatie. De belangrijkste dragende structurele delen van de vleugel zijn onderverdeeld in patches die elk geoptimaliseerd zijn en zo veel mogelijk gebruik te maken unieke eigenschappen van de composietmaterialen. De arodynamica wordt gemodelleerd met een panelenmethode, meer bepaald de doublet lattice method (DLM). De composietmaterialen en hun stijfheidskarakteristieken worden in de optimalisatie meegenomen via lamination parameters om een gradient-based optimalisatie te kunnen doen. Structurele compatibiliteit tussen de aangrenzende patches van de vleugel wordt gegarandeerd via blending constraints en hun invloed op het uiteindelijke ontwerp wordt bestudeerd. Ook wordt de invloed van de composieten stacking sequence op het proces bestudeerd.

De low-fidelity benaderingen gaan onvermijdelijk gepaard met aannames die hun accuraatheid beperken. Panelenmethoden, zoals de DLM, zijn weliswaar snel, maar echter niet geschikt om de luchtweerstand van vliegtuigen te bepalen. In dit proefschrift worden arodynamische correcties, die berekend zijn met CFD, in de DLM gemplementeerd om het effect van het vleugelprofiel en de vleugelrotatie op de arodynamische belastingen correct te bepalen. Bovendien wordt een surrogaatmodel gebruikt om tijdens de optimalisatie rekening te houden met de

luchtweerstand. Het surrogaatmodel berust op een reductietechniek om de continue structurele doorbuiging van de vleugel te benaderen met een beperkt aantal parameters. Het resulterende surrogaatmodel wordt gebruikt om de rekenkundig intensieve high-fidelity CFD arostructurele simulaties in het optimalisatiealgoritme te vervangen. Dat resulteert in een aanzienlijk snellere simulatietijd.

De voorgestelde methode is ontwikkeld binnen de analyse- en optimalisatiemogelijkheden van NASTRAN en is toegepast op een realistische industrile casus. Er zijn twee optimalisatiestudies uitgevoerd. De eerste studie focust op drie aspecten: (i) de invloed van blending constraints op de gradient-based optimalisatie, (ii) de invloed van blending constraints op de berekening van de stacking sequence, en (iii) de implementatie en effect van dynamische belastingsgevallen op het uiteindelijke vleugelontwerp. Het directe gevolg van het gebruik van de blending constraints is een vermindering van de ontwerpmogelijkheden, wat resulteert in een toename van het constructiegewicht met ongeveer 5%. Het gebruik van deze voorschriften zorgt echter voor een meer geleidelijke dikte- en stijfheidsveranderingen tussen aangrenzende patches, hetgeen uiteindelijk leidt tot een kleinere fout (ongeveer 60%) bij het bepalen van een discrete stacking sequence. Deze kleinere fout leidt uiteindelijk tot kleinere correcties die nodig zijn om een volledig produceerbaar ontwerp te verkrijgen en uiteindelijk tot een 3.7% lichter realistisch ontwerp. Dynamische belastingen zijn meegenomen in de optimalisaties via een Equivalent Static Load (ESL) methode. Ook al bleken dynamische belastingen geen significante invloed te hebben op het ontwerp, toch is aangetoond via de ESL methode dat dynamische belastingen succesvol meegenomen kunnen worden in een optimalisatie.

De tweede studie is gericht op multi-objective optimalisatie en het afwegen van minimaal gewicht en minimale luchtweerstand. Dit laatste kan bepaald worden dankzij de integratie van het surrogaatmodel voor de weerstand. De verkregen Paretocurves tonen aan dat voor structurele gewichtsminimalisatie, de optimizer de voorkeur geeft aan vleugelstructuren met wash-out gedrag met als gevolg een naar de vleugelwortel toe verschoven liftverdeling. Om het vliegtuig te trimmen moet het echter bij een hogere invalshoek vliegen waardoor de luchtweerstand toeneemt. Het minimaliseren van de weerstandscofficint resulteerde uiteindelijk in een stijvere vleugel met minder wash-out waardoor het vliegtuig bij een lagere invalshoek kan vliegen. Validatie van de resultaten met de CFD resultaten van het volledige model laat zien dat de absolute fout varieert tussen 0.9 en 1.6 drag counts, wat in lijn is met de fout van het surrogaatmodel van 1.29 drag counts.

# ACADEMIC CONTRIBUTION OF THIS DISSERTATION

In this dissertation, an optimisation framework is introduced for designing aeroelastically tailored wings during the preliminary design phase of an aircraft. The framework allows for accurate sizing of the wing structure and incorporates aerodynamic drag estimation, allowing for multidisciplinary analysis and optimisation. The main contributions of this work are as follows:

- Introduction of an aeroelastic optimisation framework for the design of aeroelastically tailored wings has been introduced. The model extends the state-of-the-art by (i) including a comprehensive set of constraints (i.e. manufacturing constraints, composite compatibility constraints, structural strength based on the Tsai-Wu failure criterion, panel buckling, blending constraints and a high-fidelity aerodynamic drag constraint), (ii) including a high-fidelity aerodynamic correction to improve load and flight shape calculation and (iii) including a combination of static and dynamic load cases. The optimisation framework is built using object-oriented programs and combines commercial FEM tools (i.e. Nastran) for gradient-based optimisation and ad-hoc open-source tools for stacking sequence retrieval.
- Presentation of a novel approach to incorporating aerodynamic drag into structural optimisation. This method employs an original reduction technique that combines traditional modal projection with advanced statistical methods to approximate wing structural displacement using a limited number of inputs. This reduction enabled the creation of a fast surrogate model, which is interfaced with the commercial tool Nastran, allowing for the inclusion of drag considerations during structural optimisation.
- Investigation of how blending constraints affect the continuous optimisation of thickness and stiffness distribution across various load case combinations, as well as assessing the influence of these constraints on the performance of the stacking sequence retrieval process.
- Exploration of the impact of incorporating high-fidelity aerodynamic drag into structural optimisation and the resulting Pareto fronts from the mul-

tidisciplinary optimisation with conflicting objectives. Additionally, the surrogate model approach was validated by comparing its results with those from the CFD model.

# CONTENTS

# NOMENCLATURE

## ROMAN SYMBOLS

| | |
|---|---|
| $\mathbf{A}$ | Laminate in-plane stiffness matrix |
| $\mathbf{B}$ | Laminate coupling stiffness matrix |
| $C_D$ | Drag coefficient |
| $\widetilde{C}_D$ | Approximation of the drag coefficient |
| $\mathbf{D}$ | Laminate out-of-plane stiffness matrix |
| $E$ | Young's modulus |
| $E$ | Euclidean distance |
| $\boldsymbol{f}_{eq}$ | Equivalent static load |
| $F_g$ | Flight profile alleviation factor |
| $G$ | Shear stiffness |
| $h$ | Laminate height |
| $H$ | Gust gradient |
| $\mathbf{K}$ | Stiffness matrix |
| $\mathbf{L}$ | Orthonormal basis resulting from a SVD decomposition |
| $\tilde{\mathbf{L}}$ | Reduced orthonormal basis resulting from a SVD decomposition |
| $\boldsymbol{LP}$ | Vector of lamination paramenters |
| $\widetilde{\mathbf{LP}}$ | Vector of target lamination paramenters |
| $\mathbf{M}$ | Mass matrix |
| $M$ | Moment |
| $N$ | Force |
| $\boldsymbol{p}_{mean}$ | Mean values of the generalized coordinates $\boldsymbol{p}$ |
| $\boldsymbol{p}$ | Generalized coordinates when projecting using $\tilde{\mathbf{L}}$ |
| $\mathbf{Q}$ | Reduced stiffness matrix |
| $\boldsymbol{q}$ | Generalized coordinates when projection using $\boldsymbol{\Phi}$ |
| $\mathbf{T}$ | Transformation matrix |
| $t_{ply}$ | Ply thickness |
| $\boldsymbol{u}_{1g}$ | Wing dispacement at 1g SLF |

| | |
|---|---|
| $U_i$ | Material invariant |
| $U_{ds}$ | Design gust velocity in EAS |
| $\mathbf{u}_E$ | Elastic structural displacement |
| $\tilde{\mathbf{u}}_E$ | Approximation of the elastic structural displacement |
| $\boldsymbol{u}_{gust}$ | Wing dispacement during gust |
| $\mathbf{u}_{res}$ | Residual displacement error |
| $U_{ref}$ | Reference gust velocity in EAS |
| $\boldsymbol{u}_{tot}$ | Total wing dispacement |
| $U$ | Gust velocity in EAS at position s |
| $v_i$ | Lamination parameter |
| $s$ | Distance travelled inside the gust |
| $Z_{mo}$ | Maximum operating altitude |

## Greek Symbols

| | |
|---|---|
| $\alpha$ | Angle of attack |
| $\Delta v_{(N \to N-X)}$ | Change in lamination parameter due to X ply drops |
| $\epsilon$ | Membrane strain |
| $\gamma$ | Shear strain |
| $\mathbf{\Gamma}_1$ | Material invariant matrix |
| $\kappa$ | Lamanate curvature |
| $\boldsymbol{\nu}$ | Generalized coordinates after PCA |
| $\nu$ | Poisson's ratio |
| $\mathbf{\Phi}$ | Modal basis |
| $\tilde{\mathbf{\Phi}}$ | Truncated modal basis |
| $\mathbf{\Psi}$ | Trasformation matrix of the PCA |
| $\tilde{\mathbf{\Psi}}$ | Truncated trasformation matrix of the PCA |
| $\sigma$ | Membrane stress |
| $\mathbf{\Sigma}$ | Diagonal matrix containing the singular values resulting from a SVD decomposition |
| $\tau$ | Shear stress |
| $\theta$ | Ply angle |

## Abbreviations

| | |
|---|---|
| ACARE | Advisory Council for Aeronautics Research in Europe |
| AFP | Automated Fiber Placement |
| ANN | Artificial Neural Networks |

| | |
|---|---|
| CAD | Computer-Aided Design |
| CAE | Computer-Aided Engineering |
| CFD | Computational Fluid Dynamics |
| CFRP | Carbon Fiber Reinforced Polymer |
| CLT | Classical Lamination Theory |
| CONLIN | Convex Linearisation Method |
| CRM | Common Research Model |
| CS | Certification Specification |
| CV | Cross-Validation |
| DLM | Doublet Lattice Method |
| DMAP | Direct Matrix Abstraction Program |
| DOE | Design of Experiment |
| EAS | Equivalent Airspeed |
| EASA | European Union Aviation Safety Agency |
| ESL | Equivalent Static Load |
| FEA | Finite Element Analysis |
| FEM | Finite Element Method |
| FI | Failure Index |
| FSI | Fluid-Structure Interaction |
| GA | Genetic Algorithm |
| GHG | Green-House Gas |
| HSA | Hybrid Static Approach |
| ICAO | International Civil Aviation Organisation |
| IPOPT | Interior Point Optimisation |
| LP | Lamination Parameter |
| LR | Linear Regression |
| MDO | Multi-Disciplinary Optimisation |
| MLW | Maximum Landing Weight |
| MoE | Mixtures of Experts |
| MSE | Mean Squared Error |
| MTOW | Maximum Take-Off Weight |
| MZFW | Maximum Zero-Fuel Weight |
| NACA | National Advisory Committee for Aeronautics |
| PCA | Principal Component Analysis |
| PR | Polynomial Regression |
| PR-ENET | Polynomial Regression with Elastic nNet |
| RANS | Reynolds-Averaged Navier-Stokes |
| RBF | Radial-Basis Function |

| | |
|---|---|
| REC | Regression Error Characteristics |
| RMSE | Root Mean Square Error |
| RSS | Residual Sum of Squares |
| SBO | Surrogate-Based Optimization |
| SST | Stacking Sequence Table |
| SVD | Singular Value Decomposition |
| SVM | Support Vector Machine |
| SVR | Support Vector Regression |
| TPS | Thin Plate Spline |
| VLM | Vortex Lattice Method |

# 1

# INTRODUCTION

Aviation, alongside other industries, continues to face the pressing need to reduce greenhouse gas (GHG) emissions in alignment with the temperature targets negotiated under the Paris Agreement of COP21. As of 2019, prior to the COVID pandemic, aviation accounted for approximately 2.5% of global $CO_2$ emissions. However, the actual impact on global warming could be significantly higher due to emissions of nitrogen oxides, soot, and water vapour, with aviation effects potentially being two to four times greater than the pure $CO_2$ effects (ICAO, 2022).

As of February 2023 (ICAO, 2023), the International Civil Aviation Organization (ICAO) forecasts that air passenger demand in 2023 will rapidly recover to pre-pandemic levels on most routes by the first quarter. By the end of the year, a growth of around 3% on 2019 figures is expected. Looking further ahead to 2024, air passenger demand is anticipated to be stronger, estimated to be around 4% higher than in 2019. This translates to a Compound Annual Growth Rate (CAGR) of 0.7% over the 2019-2024 period, and some aircraft manufacturer forecasts a CAGR of 3.6% between 2019 and 2042 (Airbus, 2023) for the passenger traffic alone. Thus, the need for more ecological aviation remains vital if we want to mitigate the impact of this growth on the environment. These needs are reflected in the program from the Advisory Council for Aeronautics Research in Europe *"ACARE Flightpath 2050"*. Among its many objectives (European Commission, 2011), this program aims at reducing $CO_2$ emissions by 75% per passenger kilometre, reducing $NO_x$ emissions by 90%, reducing perceived noise by 65% through the development of new technologies by the year 2050.

Research and development tend to concentrate mainly on three key areas for improving aircraft efficiency(Acosta et al., 2013). These areas are weight reduction, aerodynamic efficiency and engine performance. Aerolestic tailoring is the main topic of this dissertation and takes advantage of the directional stiffness properties of composite materials to control wing elastic deformation under static or dynamic aerodynamic loads in a beneficial way. By doing so, aeroelastic tailoring has the potential to achieve both structural weight reduction and aerodynamic efficiency improvement.

## 1.1 LITERATURE REVIEW

This section reviews the state-of-the-art of the different topics involved in this dissertation and serves as a background for the research objective and modelling decisions. The topics covered in this section are composite material optimisation, composite blending constraints and aeroelastic tailoring.

### 1.1.1 COMPOSITE MATERIAL OPTIMISATION

Composite materials are one of the key structural technology improvements that take part in structural weight reduction (Acosta et al., 2013). This is possible thanks to the composite materials' high strength-to-weight ratio and their intrinsic anisotropy that allows for optimising specific stiffness directions in a load-carrying component. However, while in general they offer improved mechanical performances when compared to their more conventional aluminium counterparts, composite materials are more difficult to design because of the increased number of design variables. For example, with composite materials, both thickness and plies angles need to be correctly chosen to determine the optimal stiffness and mass of the laminate. In addition, adding composite materials to an aircraft also has some drawbacks, such as galvanic corrosion, increased use of expensive and hard-to-machine titanium alloys, additional failure modes that are harder to predict, and increased environmental footprint. Optimisation of a composite structure plays a major role in composite design, and a considerable amount of work has been spent in developing modelling and optimisation methods. The books of Haftka and Gürdal (1992) and Gürdal et al. (1999) are great examples of such modelling and optimisation methods for both general structural optimisation and composite optimisation.

#### 1.1.1.1 Review of optimisation strategies

Optimising a composite structure consists of identifying its thickness and stacking sequence with respect to a given set of loads while satisfying a wide range of constraints such as stress, stability, minimum first natural frequency and manufacturing. This strategy can be effective for simple structures. However, it is not possible to make the same statement when large and complex structures are involved. The reason is that loads are not uniformly distributed over large structures such as an aircraft fuselage or wing centre box. As a consequence, the use of a uniform and constant thickness and stacking sequence design over a large structure will lead to an optimal design only for the most heavily loaded region while over-designing other less loaded parts of the structure, resulting in an overall inefficient design. As a consequence, it is common practice to divide large and complex structures into sub-regions that could be locally optimised with respect to the local load distribution.

Two works from Ghiasi et al. (2009) and Ghiasi et al. (2010) review various optimisation strategies for different classes of composite structures. The first work of Ghiasi et al. (2009) focuses on *constant stiffness* composite, where the optimal stacking sequence is uniform for the entire composite component. The second work of Ghiasi et al. (2010) focuses instead on *variable stiffness* composite structures where material distribution and/or stacking sequence can vary over the structural domain. Within the variable stiffness design category, it's possible to identify two subcategories: a *patch* variable stiffness design and a *local* variable stiffness design. A patch is a region of the structure that is defined a priori by the designer and where the stacking sequence and thickness are kept constant. The local design, instead, offers the possibility to locally describe the fiber path across the structure and results in a smooth and continuous variation of thickness and stiffness. For the sake of simplicity, in this dissertation *variable stiffness design* always refers to a structure with a patch-wise stiffness variation.

#### 1.1.1.2 Parameterisations of composite materials

A central topic in composite optimisation is the parameterisation adopted to model the composite materials. The most explicit parameterisation is the direct use of plies thickness and angle. This parameterisation allows for an easy introduction of manufacturing constraints and direct output of the stacking sequence. However, there are some drawbacks like the potentially boundless design space, the discrete nature of the design parameters that could require the use of mixed-integer programming techniques (Haftka and Gürdal, 1992) and non-convex constraint design space (e.g. buckling) presenting several local minima (Stegmann and Lund, 2005). Heuristic methods like genetic algorithms (GAs) have also been

widely used together with explicit parameterisation like the works from Haftka and Walsh (1992), Le Riche and Haftka (1993) and Adams et al. (2004). However, while heuristic methods may reach the global optimum and are suited to work with discrete quantities, they require more function evaluation than gradient-based methods. Such drawback makes these approaches difficult to apply in case of expensive functions like finite element models (FEM) or computational fluid dynamics (CFD) runs.

Another well-known approach is based on the lamination parameters (LPs) that were first introduced by Tsai and Pagano (1968). Lamination parameters are part of the implicit parameterisation and are a representation of the composite material stiffness matrices **A**, **B** and **D** derived from the classical lamination theory (CLT). Composite parameterisation via lamination parameters results in twelve parameters that, together with the thickness, fully describe any general laminate stiffness matrix regardless of the number of plies. The advantages of this parameterisation are a drastically reduced number of design variables, the design variables being continuous so that gradient-based optimisation can be implemented and a convex design space (Grenestedt and Gudmundson, 1993). On the other hand, lamination parameters do not provide a direct representation of the laminates, so an inverse optimisation problem is often performed to obtain the stacking sequence of the optimised laminates through heuristic algorithms (Irisarri et al., 2014). Moreover, the design space needs to be constrained, and the full feasible space is not known explicitly.

Lamination parameters have been applied extensively to constant and variable stiffness structure optimisation with the intent of improving mechanical performance such as compliance (Hammer et al., 1997; Setoodeh et al., 2005), buckling load (IJsselmuiden et al., 2010; Liu et al., 2004; Setoodeh et al., 2009) and natural frequencies (Abdalla et al., 2007) and also in aeroelastic tailoring (more in Section 1.1.3). For the sake of completeness, there is another implicit parameterisation that has been successfully implemented in various optimisations; this approach is called polar invariants (PIs) parameterisation and has been introduced by Verchery (1982).

#### 1.1.1.3 MANUFACTURING CONSTRAINTS AND BI-STEP APPROACH

As all implicit parameterisation methods model directly the laminate stiffness and mass matrices, a constant challenge for these methods is how to introduce stacking sequence manufacturing constraints or some mechanical constraints in the parameterisation space. Among the many manufacturing constraints that are applied to composites (Bailie et al., 2002; US Department of Defense, 2002), only

a few (e.g. symmetric and balanced stacking sequences) have a direct link to constraints onto the parameters, while the other requires more elaborate constraints that limit the design space in areas where these constraints can be enforced.

One common strategy used to optimise composite structures and enforce manufacturing constraints on the stacking sequence relies on a bi-step approach (Bloomfield et al., 2009b; Dillinger, 2014; Herencia et al., 2007b; IJsselmuiden et al., 2009; Liu et al., 2011), where a gradient-based (continuous) optimisation of homogenised stiffness parameters (e.g. lamination parameters) is performed to obtain the continuous optimum design. Later, combinatorial optimisation is used to retrieve the best stacking sequences matching the continuous design while enforcing manufacturing constraints. This second step (discrete optimisation) is typically performed via evolutionary algorithms (e.g. genetic algorithms). However, due to the difficulties in enforcing some manufacturing constraints in the gradient-based optimisation with homogenised stiffness parameters, these constraints are usually implemented only during stacking sequence retrieval. As a consequence, two different sets of constraints are used in the two subsequent optimisations. This reduces the chance of finding in the discrete domain a design close to the optimal continuous solution. So, while the continuous optimum represents the theoretical optimum that could be achieved, a drop in performance should be expected when retrieving the laminate stacking sequence. Such drop depends on the number of plies in the laminate and the number of additional constraints introduced in the stacking sequence retrieval. One way of reducing such loss in performance is to include in the gradient-based optimisation more and more manufacturing constraints. Some examples with lamination parameters are the 10%-rule constraint derived by Abdalla et al. (2009), the blending constraints derived by Macquart et al. (2016) and the strength constraints based on Tsai-Wu failure criteria derived by IJsselmuiden et al. (2008).

### 1.1.2 Blending constraints

Various blending definitions have been proposed by different authors like Adams et al. (2004) and van Campen et al. (2008) (more details in Section 2.4). The objective of blending constraints is to ensure a smooth and gradual variation of the structural thickness and stiffness distributions to ensure structural continuity and avoid stress concentration during the design and optimisation of a variable stiffness composite structure. The first definition of blending and its first application in composite optimisation has been performed by Kristinsdottir et al. (2001). The process starts with a set of predefined loads and the identification of the most critical region. Every ply in the structure originates from the critical region and can span any number of adjacent regions until it is dropped. Once a ply is dropped, it cannot be added back again. This constant dropping from the most loaded region is called the *"grater-than-or-equal-to"* blending rule. In this

way, blending ensures that a structure is manufacturable by allowing a controlled ply-drop and consistent fiber angle across the structure.

Liu (2001) used a bi-step sequential optimisation using response surfaces to enforce continuity and derived two measures of continuity, the one based on the ratio of common ply angles between adjacent panels, the second based on the number of layers that can be continuous between two adjacent laminates. Soremekun et al. (2002) proposed instead an iterative two-step genetic algorithm approach where the minimum number of plies required in each panel is identified and then used to create a base laminate spanning the entire structure. This process is repeated for all the remaining panels until the final design is reached. Adams et al. (2004) uses a different approach that relies on a single-step GA and the concept of "guiding stack". Similarly to the *"grater-than-or-equal-to"* blending rule, a guiding stack is defined for the thickest laminate from which other panel laminates are obtained by dropping plies. This new formulation reduces the dimensionality of the problem and eliminates the need for continuity constraints. An enhanced version of the guide-based blending proposed by Adams et al. (2004) is the stacking sequence table (SST) proposed by Irisarri et al. (2014). SST contains additional information about the order of ply-drops, thus it provides a more detailed picture of the stacking sequence layout over the panels and results in a convenient tool to introduce a wide variety of composite manufacturing rules (Irisarri et al., 2014; US Department of Defense, 2002).

Except for the work by Liu (2001), in all the above-mentioned works and many other (Jin et al., 2016; Seresta et al., 2009; Soremekun et al., 2002) composite structure optimisation with blending constraints were performed via a heuristic method (e.g. GA) or random search (Improved Hit and Run) that require a significant amount of structural analyses. The first attempt to derive blending constraints in the lamination parameters space to be used in a gradient-based optimisation has been proposed by Macquart et al. (2016).

### 1.1.3 AEROELASTIC TAILORING

Aeroelastic tailoring has been defined by Shirk et al. (1986) as *"the embodiment of directional stiffness into an aircraft structural design to control aeroelastic deformation, static or dynamic, in such a fashion as to affect the aerodynamic and structural performance of that aircraft in a beneficial way,"*. The areas that can be improved by proper aeroelastic tailoring include but are not limited to structural weight, buckling, stress/strain, fatigue, flutter, divergence, aileron effectiveness, lift and drag. While aeroelastic tailoring is not limited to the sole use of composite materials, as shown by Harmin et al. (2011), their superior material properties and intrinsic anisotropy make them the ideal materials. A very extensive review of the aeroelastic tailoring for subsonic transport aircraft can be found in the work from Jutte and Stanford (2014), while early research and findings can be found

in Shirk et al. (1986) and Weisshaar (1987).

The first reported application of aeroelastic tailoring can be found in a patent from Munk (1949). In the patent, a fixed-pitch blade is manufactured, taking into consideration the orientation of wood fibers to have a favourable twist deformation as thrust changes. One of the early examples of the weight-saving capabilities of aeroelastic tailoring with composite materials is the work from Krone (1975). In his work, Krone demonstrated that the structural weight penalty associated with divergence prevention could be greatly reduced when using composite materials (Figure 1.1). This result has been achieved by controlling the composite stiffness and orientation, which results in a wash-out wing behaviour. The concepts and impact of wash-in and wash-out can be found in the work from Shirk et al. (1986) and are summarised in Figure 1.2. Wash-out is a typical behaviour of aft-swept wings where wing bending is coupled with wing nose-down torsion that reduces the sectional angle of attack and, thus, the lift generated by the wing. On the contrary, wash-in is a typical behaviour of a forward-swept wing that couples wing bending with nose-up torsion that increases the sectional angle of attack and, therefore, the lift. If this wash-in behaviour is not counteracted by sufficient structural torsional strength, the wing will fail due to divergence. In addition, Figure 1.2 also shows how structural designers can impact not only the stress distribution but also the lift distribution, handling qualities and aeroelastic instabilities through directional stiffness.

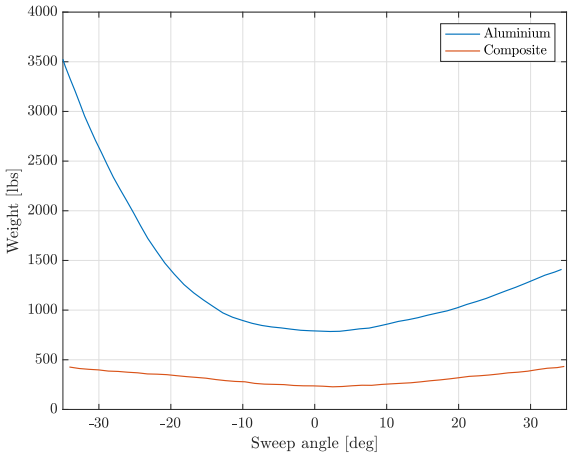


**Figure 1.1:** Comparison between structural weight and wing sweep angle for aluminium and composite wings. Original from Krone (1975).

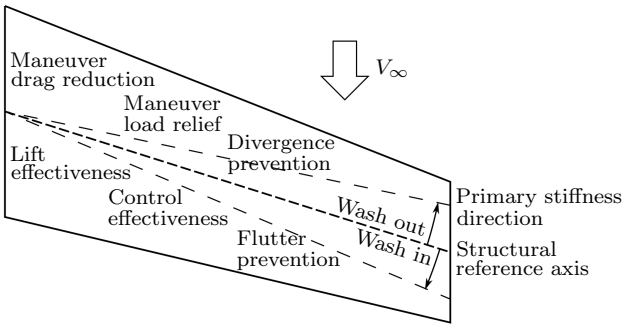


**Figure 1.2:** Effects of aeroelastic tailoring. Original from Shirk et al. (1986).

#### 1.1.3.1 Aeroelastic tailoring with lamination parameters

Several works on aeroelastic tailoring have been carried out, taking advantage of lamination parameters. Fukunaga and Sekine (1994) evaluated the effect of the lamination parameters on the extension-shear coupling and how such coupling affects differently flutter and divergence speeds. In a later work, Kameyama and Fukunaga (2007) optimised a composite plate wing with various sweep angles for minimum weight subjected to flutter and divergence speed constraints. Their work clearly showed the effect of aeroelastic tailoring and also revealed the presence of potential discontinuities in flutter and divergence speeds in the lamination parameters domain. Herencia et al. (2007a) presented a bi-step approach to minimise the mass of a shell-based FEM wing having five spanwise patches from root to tip optimisable with symmetric laminates and 0, 90, 45 or -45 degree ply angles. The first step uses a gradient-based optimiser in the lamination parameters space with strength, buckling, and practical design constraints. Lift and induced drag were also included in the optimisation thanks to the use of PANAIR Carmichael and Erickson, a linear potential flow solver. The second step uses a genetic algorithm to obtain the actual stacking sequence. Dillinger et al. (2013) expanded the approach proposed by Herentia and investigated the effect of balanced and unbalanced laminates on a wing with several spanwise and chordwise patches. In his work, the stacking sequence of a composite wing is optimised for mass or aileron effectiveness, and the impact on the final design is investigated. His research has been extended to incorporate high-fidelity computational fluid dynamics (CFD) corrections to the doublet lattice method (DLM) used during the optimisation. In addition, this later work focuses on the aeroelastic tailoring of a forward-swept composite wing (Dillinger et al., 2019).

#### 1.1.3.2 Aeroelastic tailoring and dynamic loads

Conventional wing structural sizing of large transport aircraft usually considers symmetric static manoeuvres, like $2.5g$ pull-up and $-1g$ push-down manoeuvres, as design loads together with aeroelastic phenomena like divergence, flutter and aileron effectiveness (Torenbeek, 2013). While this is the case for most of the above-mentioned studies, Kenway et al. (2014) showed that a metallic large transport aircraft wing optimised for static manoeuvres loads could fail when subjected to discrete gusts, underlying the need to include dynamic load cases during optimisation. Werter (2017) obtained similar results with a composite large transport aircraft wing and showed how wings optimised with static loads and unbalanced stacking sequence are more prone to failure under dynamic loads than wings designed with a more conventional stacking sequence (e.g. $[0_{60\%}/\pm 45_{30\%}/90_{10\%}]_s$). One of the challenges in gust analysis is that the critical load cases are not known a priori, and for that reason, a large number of simulations need to be run. To speed up computation, Rajpal et al. (2019) utilised a balanced proper order decomposition to reduce the aerodynamic system coupled to a structural solver to obtain a reduced-order aeroelastic model. Results on a clamped model show that the critical gust loads change and it is important to keep track of them during the optimisation process. Finally, Reimer et al. (2015) and Lancelot and De Breuker (2016) show that dynamic loads are also influenced by the flight dynamics of the aircraft.

#### 1.1.3.3 Multidisciplinary design optimization

While a large portion of the research in aeroelastic tailoring is based on low fidelity linearised potential aerodynamics (e.g. strip theory or pannel methods) and focuses mainly on structural optimisation, the Multidisciplinary Design Optimization Laboratory (MDO Lab) research group [1] at the University of Michigan developed an adjoint-based aero-structural optimiser that allows for simultaneous aerodynamic shape optimisation and structural sizing. This has been achieved thanks to a framework that couples high-fidelity Euler/RANS (Reynolds-Averaged Navier-Stockes) aerodynamics and finite element models and shows the benefits in terms of fuel burn and weight reduction that can be obtained when combining aerodynamic and structural optimisation (Bons and Martins, 2020; Brooks et al., 2018; Burdette and Martins, 2018; Kennedy and Martins, 2014; Kenway and Martins, 2014; Liem et al., 2015; Martins et al., 2004, 2005). Despite the remarkable results obtained with high-fidelity RANS/FEM aero-structural optimisation, these simulation remains computationally very expensive and rarely applicable during conceptual or preliminary design phases, even with the current supercomputer. The reason is that during these phases, up to several hun-

[1] http://mdolab.engin.umich.edu/

dreds of manoeuvres and aircraft configurations could be considered, and each resulting load case could have thousands of constraints. While constraints can be reduced through agglomeration functions (e.g. Kreisselmeier and Steinhauser (1979)), the number of load cases has a strong negative impact on the computational time. To speed up simulation time, a parallel computation strategy has been developed (Kennedy and Martins, 2014), and significant effort has been made towards accelerating high-fidelity CFD gradients computations by using faster lower-fidelity aerodynamics as preconditioner (Jovanov, 2019).

#### 1.1.3.4 SURROGATE BASED OPTIMIZATION

A very popular alternative to the direct use of CFD in optimisation processes is to construct a cheap-to-use approximation model of the expensive CFD analysis. These approximations are usually referred to as surrogate models or metamodels and express complicated relationships between the responses (outputs) and the design variables (inputs) with a simple equation. Once computed, these models require minimal computational effort to run, making them ideal for optimisation purposes (Forrester and Keane, 2009). Surrogate-based optimisation (SBO) has been used for speeding up evolutionary algorithms like genetic algorithms (GAs) used in 2D or 3D aerodynamic optimisation (Jeong et al., 2005; Song and Keane, 2007) via the Kriging model. GAs require many objective function evaluations, and therefore, replacing expensive high-fidelity CFD analysis with the Kriging model reduced the computational time drastically. The Kriging model, in particular, is very powerful as it is naturally equipped with an uncertainty estimation. This uncertainty estimation can be integrated into adaptive sampling approaches where an initial surrogate model is built, and new data points are iteratively added to update the model (Liu et al., 2017). These additional points can either improve the general accuracy of the model (exploration) or improve the optimal design under study (exploitation). Multidisciplinary design optimisations can also benefit from the use of a surrogate to approximate coupled multidisciplinary simulations like in aeroacustics (Jouhaud et al., 2007) and aeroelasticity. Nevertheless, SBOs are inherently limited to the dimension of the inputs, so dimensionality reduction techniques are required in applications with hundreds or thousands of design variables.

Different authors used surrogate models to perform static aero-structural gradient-based optimisation. Zhang et al. (2008) compared different surrogate models (quadratic polynomial regression, Kriging and neural network) to maximise the aircraft lift-to-drag ratio and minimise the weight with respect to the wing planform parameters and structural thicknesses and concluded that not considering the aeroelastic effect will result in large errors. Rasmussen et al. (2008) outlines a methodology to optimise the weight and perform design exploration for a joined-wing aircraft (no aerodynamic performance involved). The optimisation has been

divided into two steps. The first step consists of performing aero-structural optimisation for weight minimisation for different geometric aircraft configurations. A weight-optimised solution was found by varying spar, rib, and skin thicknesses of the wing structure. The second step consisted of creating an approximation, via polynomial regression, of the entire design space, using the optimised structures as sample points. The surrogate moderate fit is then used to define optimal regions and design trends and is not used to determine precise optimal configurations. Paiva et al. (2010) also compares different surrogate models (quadratic polynomial regression, Kriging and neural network) of the aerodynamic coefficients ($C_L$, $C_D$ and $C_M$) using a panel method aerodynamic model as a function of several geometrical, structural (thicknesses) and aerodynamic (NACA profile) parameters concluding that polynomial regression proves to be adequate only for low dimensionality problems. Lebofsky et al. (2014) utilises a surrogate model of an aircraft wing drag coefficient that is a function of wing geometry variables such as the jig twist-law and deflection parameters of variable camber trailing edge flaps to minimise drag at off-design cruise conditions in a gradient-based optimisation.

#### 1.1.3.5 Aeroelastic tailoring and fiber steering

For the sake of completeness, several promising results have been achieved in aeroelastic tailoring by using fiber steering. Fiber steering falls under the *local* variable stiffness design proposed in Ghiasi et al. (2010) and allows continuous spatial variation of mechanical properties to achieve exceptional tailoring capability. This approach has recently gained momentum thanks to the development of large-scale advanced fiber and tow placement (AFP) technologies. Examples of this research in this field can be found in the works from Stodieck et al. (2013, 2017), Stanford et al. (2014), Stanford and Jutte (2017) and Brooks et al. (2019)

## 1.2 Research objective

Starting from the work of Dillinger (2014), this dissertation incorporates some of the topics described in the previous section and has the objective to:

*develop a preliminary wing design framework to perform aeroelastic tailoring, considering both structural weight and high-fidelity aerodynamic drag while enforcing composite blending.*

Different fidelity levels could be used to perform aeroelastic tailoring depending on the design phase and the required objectives: from Euler-Bernoulli beam structures with panel methods for unsteady aerodynamics (Lebofsky et al., 2014)

to complex FEM shell geometry fully coupled with high-fidelity RANS computations (Kenway et al., 2014). As this dissertation focuses on the preliminary design of a composite wing, a FEM shell model is used together with a fast aerodynamic panel method called the doublet lattice method (DLM). On the structural side, the selection of shell FEM allows for detailed modelling of the main load-bearing structures and the direct inclusion of mechanical constraints during sizing. On the aerodynamic side, the use of panel methods results in a fast load generation for potentially thousands of different load cases, both static and dynamic.

Composite material optimisation is included in this dissertation via lamination parameters, and particular focus is placed on ensuring structural continuity in the design via blending and studying its effect on wing sizing.

While being fast and resulting in conservative loads, panel methods are irrotational and inviscid, thus unsuitable for estimating aircraft performance (i.e. lift-to-drag ratio or drag coefficient) or capturing the effect of airfoil camber and wing twist law. CFD-based corrections to the panel method are implemented to correctly represent the wing spanwise and chordwise load distribution. Finally, a surrogate model is introduced to take aerodynamic drag into account during the optimisation. To achieve this, an original reduction technique based on both traditional modal projection and advanced statistical techniques has been developed in order to approximate the wing structural deflection with a limited number of inputs, suitable for Machine Learning models. The proposed reduction allowed the creation of a fast surrogate model based on rigid CFD that could replace costly high-fidelity CFD aero-structural runs. The proposed strategy is then implemented in the commercial tool Nastran and applied to a realistic industrial case.

## 1.3 DISSERTATION OUTLINE

The contribution of this dissertation is divided into three main tasks, which are (i) extending the framework from Dillinger (2014) to include composite blending and dynamic loads, (ii) applying the framework to different aeroelastic tailoring optimisations of a regional aircraft composite wing structure and (iii) including of high-fidelity aerodynamic drag during preliminary design.

The rest of the dissertation is outlined as follows:

- Chapter 2 provides a general introduction to composite materials and focuses on the introduction of two topics: the lamination parameters and the blending constraints.
- Chapter 3 shows the approach used to create the surrogate model that approximates the aerodynamic drag. The chapter first explains how the

wing structural deflection is approximated and what techniques are used to reduce the model dimensionality. Secondly, the chapter introduces what numerical models are used to approximate the aerodynamic drag and what selection process is used to derive the surrogate model. Application of what is introduced in this chapter is presented later in Section 6.1.

- The application case used in this dissertation is presented in Chapter 4 together with the two-step optimisation approach used in all case studies. In particular, Section 4.2.6 covers the integration of gust loads into the optimisation while the interface between the optimiser and the surrogate model for aerodynamic gust is covered in Section 4.2.7.

- Chapter 5 applies the composite parameterisation and blending constraints presented in Chapter 2 to the weight minimisation of the composite wing presented in Chapter 4. Several optimisations are performed to show the effect of the blending constraints on the continuous optimisation, the relevance of static and dynamic loads on the final wing design, and the effect of blending constraints on the stacking sequence retrieval.

- In Chapter 6, first the approximation of the structural deflection and the surrogate model selection process presented in Chapter 3 are applied to the wing case introduced in Chapter 4. Secondly, the derived surrogate model is applied to a multi-objective optimisation to perform trade-off studies of conflicting objectives: weight minimisation and aerodynamic drag.

- Chapter 7 is reserved for the conclusions and suggestions on future activities.

# 2

# COMPOSITE MATERIALS AND BLENDING CONSTRAINTS

On the macroscopic scale, the building blocks of composite materials are single plies which are defined as thin orthotropic layers of fiber and matrix. These orthotropic layers are stacked on top of each other to form a laminate, and the orientation of all the plies is called a stacking sequence. As this dissertation focuses on the optimisation of laminate stacking sequence, fiber and matrix are not modelled separately, and their properties are considered constant during the optimisation.

In this chapter, Section 2.1 introduces the classical lamination theory (CLT) that allows translating the stacking sequence into an equivalent stiffness matrix called the ABD-matrix. Section 2.2 briefly covers some of the manufacturing rules and introduces some best practices when designing a laminate stacking sequence. Lamination parameters used in this dissertation to parameterise the composite materials are introduced in Section 2.3. Finally, Section 2.4 presents the blending constraints that are used to ensure structural continuity in the composite structure.

## 2.1 CLASSICAL LAMINATION THEORY



The stiffness properties of composite laminates are usually modelled using the classical lamination theory (Gürdal et al., 1999; Kassapoglou, 2013). In classical lamination theory (CLT), a ply (or lamina) is defined as the smallest element on a macroscopic scale to be used to build a composite laminate. The ply is considered to be a thin orthotropic layer, thus having only in-plane stiffness ($\sigma_3 = \tau_{23} = \tau_{13} = 0$). Therefore, the ply Hooke's law that describes the strain-stress state is as in Equation (2.1).

$$\begin{pmatrix} \sigma_1 \\ \sigma_2 \\ \tau_{12} \end{pmatrix} = \begin{bmatrix} Q_{11} & Q_{12} & 0 \\ Q_{12} & Q_{22} & 0 \\ 0 & 0 & Q_{66} \end{bmatrix} \begin{pmatrix} \epsilon_1 \\ \epsilon_2 \\ \gamma_{12} \end{pmatrix} \tag{2.1}$$

where $\sigma_1$, $\sigma_2$ and $\tau_{12}$ refers to the in-plane longitudinal, transverse and shear stresses respectively, $\epsilon_1$, $\epsilon_2$ and $\epsilon_{12}$ refers to the in-plane longitudinal, transverse and shear strains respectively, $Q_{ij}$ are the components of the reduced stiffness. The subscripts $(\cdot)_1$ and $(\cdot)_2$ refer to the ply coordinate system, where the axis 1 is aligned with the fiber direction (see Figure 2.1). The components $Q_{ij}$ of the reduced stiffness matrix are written as:

$$Q_{11} = \frac{E_{11}}{1 - \nu_{12}\nu_{21}} \tag{2.2}$$

$$Q_{12} = \frac{\nu_{12}E_{22}}{1 - \nu_{12}\nu_{21}} \tag{2.3}$$

$$Q_{22} = \frac{E_{22}}{1 - \nu_{12}\nu_{21}} \tag{2.4}$$

$$Q_{66} = G_{12} \tag{2.5}$$

where $E$ is the Young's modulus, $G$ is the shear modulus, and $\nu$ is the Poisson's ratio.

During the manufacturing of composite laminates, several plies are stacked on top of each other with an arbitrary orientation with respect to the global coordinate system ($x$,$y$). The relative rotation of the ply coordinate system (1,2) to the global coordinate system ($x$,$y$) is described by the ply angle $\theta$ and pictured in Figure 2.1. Therefore, the strain-stress relation expressed in Equation (2.1) has to be rotated in the global coordinate system before being used to describe the laminate. The rotation is achieved with the transformation matrix, $\mathbf{T}$ in Equation (2.6), thus the strains and stresses in the (1,2) coordinate system can be described as in

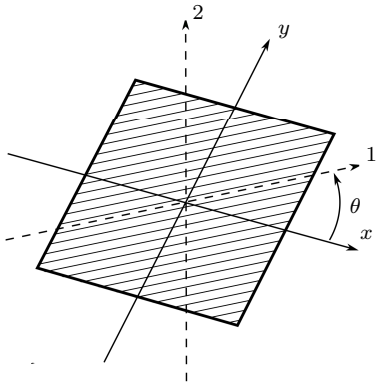


**Figure 2.1:** Definition of ply and laminate coordinate system.

Equation (2.7):

$$\mathbf{T} = \begin{bmatrix} \cos^2\theta & \sin^2\theta & 2\cos\theta\sin\theta \\ \sin^2\theta & \cos^2\theta & -2\cos\theta\sin\theta \\ -\cos\theta\sin\theta & \cos\theta\sin\theta & \cos^2\theta - \sin^2\theta \end{bmatrix} \tag{2.6}$$

$$\begin{pmatrix} \sigma_1 \\ \sigma_2 \\ \tau_{12} \end{pmatrix} = \mathbf{T} \begin{pmatrix} \sigma_x \\ \sigma_y \\ \tau_{xy} \end{pmatrix}, \qquad \begin{pmatrix} \epsilon_1 \\ \epsilon_2 \\ \epsilon_{12} \end{pmatrix} = \mathbf{T} \begin{pmatrix} \epsilon_x \\ \epsilon_y \\ \epsilon_{xy} \end{pmatrix} \tag{2.7}$$

The relations in Equation (2.7) hold only for the tensorial shear strain $\epsilon_{12}$ and not for the engineering shear strain $\gamma_{12}$ used in Equation (2.1). Thus, the relation between engineering and tensorial shear strain has to be taken into account:

$$\mathbf{R} = \begin{bmatrix} 1 & 0 & 0 \\ 0 & 1 & 0 \\ 0 & 0 & 2 \end{bmatrix} \tag{2.8}$$

$$\begin{pmatrix} \epsilon_1 \\ \epsilon_2 \\ \gamma_{12} \end{pmatrix} = \mathbf{R} \begin{pmatrix} \epsilon_1 \\ \epsilon_2 \\ \epsilon_{12} \end{pmatrix}, \qquad \begin{pmatrix} \epsilon_x \\ \epsilon_y \\ \gamma_{xy} \end{pmatrix} = \mathbf{R} \begin{pmatrix} \epsilon_x \\ \epsilon_y \\ \epsilon_{xy} \end{pmatrix} \tag{2.9}$$

By combining Equations (2.1), (2.7) and (2.9), it is possible to obtain the stress-strain relation of a ply in the global coordinate system ($x$,$y$):

$$\begin{pmatrix} \sigma_x \\ \sigma_y \\ \tau_{xy} \end{pmatrix} = \overline{\mathbf{Q}} \begin{pmatrix} \epsilon_x \\ \epsilon_y \\ \gamma_{xy} \end{pmatrix} \tag{2.10}$$

where $\overline{\mathbf{Q}}$ is the reduced stiffness matrix of the rotated ply:

$$\overline{\mathbf{Q}} = \mathbf{T^{-1}QRTR^{-1}} \tag{2.11}$$

A laminate is a stack of arbitrarily oriented plies, and the order in which the plies are stacked and their orientation is called the stacking sequence. The CLT assumes that each ply is perfectly bonded with its neighbouring layer by means of an infinitely thin bond line and that the laminate thickness is small compared to its width and length. The Kirchhoff-Love theory of plates is used to describe the kinematics of the laminate. The hypotheses are:

1. Straight lines normal to the mid-surface remain straight after deformation
2. Straight lines normal to the mid-surface remain normal to the mid-surface after deformation
3. The thickness of the plate does not change during a deformation

Thus, the strain of the $k$-th ply can be described as:

$$\begin{pmatrix} \epsilon_x \\ \epsilon_y \\ \gamma_{xy} \end{pmatrix}_k = \begin{pmatrix} \epsilon_x^0 \\ \epsilon_y^0 \\ \gamma_{xy}^0 \end{pmatrix} + z \begin{pmatrix} \kappa_x \\ \kappa_y \\ \kappa_{xy} \end{pmatrix} \tag{2.12}$$

where $\epsilon_x^0$, $\epsilon_y^0$ and $\gamma_{xy}^0$ are the mid-plane normal and shear strains, $\kappa_x$, $\kappa_y$ and $\kappa_{xy}$ are the laminate curvatures and $z_{k-1} < z < z_k$ is the coordinate in the thickness direction of the $k$-th ply as shown in Figure (2.2). By combining Equations (2.10) and (2.12), it is possible to obtain the strain-stress relation for a specific ply in the laminate:

$$\begin{pmatrix} \sigma_x \\ \sigma_y \\ \tau_{xy} \end{pmatrix}_k = \overline{\mathbf{Q}}_k \begin{pmatrix} \epsilon_x^0 \\ \epsilon_y^0 \\ \gamma_{xy}^0 \end{pmatrix} + z\overline{\mathbf{Q}}_k \begin{pmatrix} \kappa_x \\ \kappa_y \\ \kappa_{xy} \end{pmatrix} \tag{2.13}$$

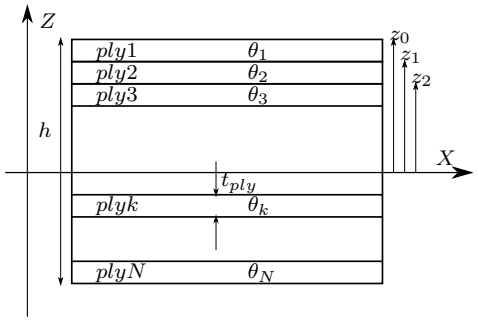


**Figure 2.2:** Schematic cross section of a laminate with $N$ plies with same ply thickness $t_{ply}$ and different orientation $\theta_i$.

The laminate total force and moment are obtained by integrating the ply stresses over the laminate thickness $h$. However, since each ply has a discrete thickness

and each and the ply stresses are not continuous throughout the laminate, it is convenient to integrate the stresses in every single ply and perform a subsequent summation:

$$\begin{pmatrix} N_x \\ N_y \\ N_{xy} \end{pmatrix} = \sum_{k=1}^{N} \int_{z_{k-1}}^{z_k} \begin{pmatrix} \sigma_x \\ \sigma_y \\ \tau_{xy} \end{pmatrix}_k dz \tag{2.14}$$

$$\begin{pmatrix} M_x \\ M_y \\ M_{xy} \end{pmatrix} = \sum_{k=1}^{N} \int_{z_{k-1}}^{z_k} z \begin{pmatrix} \sigma_x \\ \sigma_y \\ \tau_{xy} \end{pmatrix}_k dz \tag{2.15}$$

where $N_x$, $N_y$ and $N_{xy}$ are the forces and $M_x$, $M_y$ and $M_{xy}$ are the moments of the entire laminate. Combining Equations (2.13), (2.14) and (2.15) and performing the integration and summation leads to:

$$\begin{pmatrix} N_x \\ N_y \\ N_{xy} \end{pmatrix} = \mathbf{A} \begin{pmatrix} \epsilon_x^0 \\ \epsilon_y^0 \\ \gamma_{xy}^0 \end{pmatrix} + \mathbf{B} \begin{pmatrix} \kappa_x \\ \kappa_y \\ \kappa_{xy} \end{pmatrix} \tag{2.16}$$

$$\begin{pmatrix} M_x \\ M_y \\ M_{xy} \end{pmatrix} = \mathbf{B} \begin{pmatrix} \epsilon_x^0 \\ \epsilon_y^0 \\ \gamma_{xy}^0 \end{pmatrix} + \mathbf{D} \begin{pmatrix} \kappa_x \\ \kappa_y \\ \kappa_{xy} \end{pmatrix} \tag{2.17}$$

where:

$$\begin{aligned} \mathbf{A} &= \sum_{k=1}^{N} \overline{\mathbf{Q}}_k (z_k - z_{k-1}) \\ \mathbf{B} &= \frac{1}{2} \sum_{k=1}^{N} \overline{\mathbf{Q}}_k (z_k^2 - z_{k-1}^2) \\ \mathbf{D} &= \frac{1}{3} \sum_{k=1}^{N} \overline{\mathbf{Q}}_k (z_k^3 - z_{k-1}^3) \end{aligned} \tag{2.18}$$

are called laminate membrane stiffness matrix, laminate membrane-bending coupling matrix and laminate bending stiffness matrix, respectively. Rewriting Equations (2.16) and (2.17) in matrix notation results in the ABD-matrix that describes the laminate stiffness properties:

$$\begin{pmatrix} N_x \\ N_y \\ N_{xy} \\ M_x \\ M_y \\ M_{xy} \end{pmatrix} = \left[\begin{array}{ccc|ccc} A_{11} & A_{12} & A_{16} & B_{11} & B_{12} & B_{16} \\ & A_{22} & A_{26} & & B_{22} & B_{26} \\ sym. & & A_{66} & sym. & & B_{66} \\ \hline B_{11} & B_{12} & B_{16} & D_{11} & D_{12} & D_{16} \\ & B_{22} & B_{26} & & D_{22} & D_{26} \\ sym. & & B_{66} & sym. & & D_{66} \end{array}\right] \begin{pmatrix} \epsilon_x^0 \\ \epsilon_y^0 \\ \gamma_{xy}^0 \\ \kappa_x \\ \kappa_y \\ \kappa_{xy} \end{pmatrix} \tag{2.19}$$

The ABD-matrix highlights the complex coupling and mechanical behaviour of composite laminate. While **A** matrix describes the laminate in-plane behaviour and **D** matrix describes the laminate out-of-plane behaviour, the **B** matrix couples together the in-plane and out-of-plane behaviour. This means that for the non-zero $B_{ij}$ term, an in-plane tension or compression load can result in out-of-plane laminate deformations. This laminate behaviour is often undesired in practical application, and one effective way to a null **B** matrix is to work only with symmetric laminates. Therefore, in this dissertation, only symmetric stacking sequences are used.

Another interesting coupling exists between in-plane tension and shear due to the $A_{16}$ and $A_{26}$ terms. When these two terms are not zero, an in-plane tension will result in extensional and shear strains. This coupling can be prevented by using only balanced stacking sequences. A balance stacking sequence is characterised by having for each ply at angle $\theta$ another ply at $-\theta$. However, this coupling is very important for aeroelastic tailoring since it can be used to modify the wing's global bending-twist behaviour. Similarly, the **D** matrix can present a bending-twist coupling associated with the $D_{16}$ and $D_{26}$ terms. These coupling terms are important as they mostly degrade stability margins for buckling.

## 2.2 MANUFACTURING GUIDELINES

Manufacturing guidelines have been developed using analysis, components testing, and hands-on experience to avoid undesired laminate features that could significantly impact the strength and durability of composite components. Some undesired features include high interlaminar stresses, complex coupling mechanisms, large resin pockets or weak damage tolerance. Moreover, possible ply orientations are usually reduced to a set of few discrete angles such as [0°, ±15°, ±30°, ±45°, ±60°, ±75°, 90°]. As a result, these guidelines can heavily affect the composite structural design and should be taken into account early in the design phase. The interested reader is invited to have a look at Bailie et al. (2002) or US Department of Defense (2002) for a more in-depth discussion on the different guidelines.

Manufacturing guidelines are usually divided into three categories (Irisarri et al., 2014). These categories are presented with a few guidelines for the sake of clarity. The first set of guidelines refers only to the single composite panel and are:

1. Symmetry: The stacking sequence must be symmetric with respect to the mid-plane to avoid any membrane bending coupling effect.

2. Balance: The stacking sequence must have the same number of plies with an orientation equal to $+\theta^\circ$ and $-\theta^\circ$ to avoid any tension-shear coupling.

3. Contiguity: Limits are placed on the number of consecutive plies aligned in the same direction to limit delamination and matrix cracking.
4. Disorientation: No more than 45° ply orientation difference between successive layers to avoid free-edge interlaminar stresses;
5. 10% rule: Plies with 0°, ±45°, and 90° orientation should account each for at least 10% of the total number of plies. Thus, it ensures a minimum in-plane stiffness in all directions to account for unforeseen secondary loading.
6. Damage tolerance: No primary load-carrying plies should be placed on the outer or inner surface of the laminate to reduce the chance of damage from scratches and corrosion.



The second set refers to the ply-drop in the composite panel and aims at reducing resin pockets, stress concentrations, and delaminations due to excessive ply-drops from one stacking sequence to another within the same panel. The third set is the global guidelines and is applied to the component level. Among these global guidelines lies the concept of blending. Blending constraint aims at ensuring structural integrity and manufacturability of the component and is covered in more detail in Section 2.4.

## 2.3 Lamination parameters

The classical lamination theory can be used to determine the stiffness properties of a composite laminate based on the ply thickness and angles. However, this parameterisation is not suitable for the optimisation of large composite structures for two reasons. First, the number of design variables varies linearly with the number of plies. Industrial cases of large composite structures can be composed of tens or hundreds of laminates that have between 10 and 100 plies each, resulting in a design space too big to handle. Second, due to manufacturing constraints, only certain values of thickness and ply angles are allowed, resulting in a discrete optimisation problem that cannot make use of powerful gradient-based optimisation techniques. To circumvent these problems, a well-established strategy is to use a parameterisation of the ABD-matrix by means of lamination parameters (LP). Other such parameterisations (e.g., polar invariants) exist that allow for fixed-size optimisation parameters. In this dissertation, only lamination parameters have been considered.

### 2.3.1 Mathematical representation

The lamination parameters approach has been first introduced by Tsai and Pagano (1968) and Tsai and Hahn (1980). The first use of lamination parameters

for optimisation purposes has been done by Miki (1982) under a graphical approach, and since then, they have been used successfully by many researchers (see Section 1.1.1 for references). This approach allows the modelling of a generic ABD-matrix of a laminate in a continuous way by separating the material-dependent parameters, the so-called Tsai-Pagano invariants, from the stacking sequence parameters called lamination parameters. Lamination parameters ($v_i$) are defined as the integral, over the thickness, of the layers angles:

$$\begin{aligned}
(v_1^{\mathbf{A}}, v_2^{\mathbf{A}}, v_3^{\mathbf{A}}, v_4^{\mathbf{A}}) &= \frac{1}{h}\int_{-h/2}^{h/2}(\cos 2\theta, \sin 2\theta, \cos 4\theta, \sin 4\theta)\mathrm{dz} \\
(v_1^{\mathbf{B}}, v_2^{\mathbf{B}}, v_3^{\mathbf{B}}, v_4^{\mathbf{B}}) &= \frac{4}{h^2}\int_{-h/2}^{h/2} z(\cos 2\theta, \sin 2\theta, \cos 4\theta, \sin 4\theta)\mathrm{dz} \\
(v_1^{\mathbf{D}}, v_2^{\mathbf{D}}, v_3^{\mathbf{D}}, v_4^{\mathbf{D}}) &= \frac{12}{h^3}\int_{-h/2}^{h/2} z^2(\cos 2\theta, \sin 2\theta, \cos 4\theta, \sin 4\theta)\mathrm{dz}
\end{aligned} \tag{2.20}$$

With lamination parameters, any stacking sequence can be reproduced with twelve continuous variables, together with laminate thickness and material invariant matrices $\Gamma_i$. The relation between lamination parameters, thickness and material invariant is described by:

$$\begin{aligned}
\mathbf{A} &= h(\mathbf{\Gamma}_0 + \mathbf{\Gamma}_1 v_1^{\mathbf{A}} + \mathbf{\Gamma}_2 v_2^{\mathbf{A}} + \mathbf{\Gamma}_3 v_3^{\mathbf{A}} + \mathbf{\Gamma}_4 v_4^{\mathbf{A}}) \\
\mathbf{B} &= \frac{h^2}{4}(\mathbf{\Gamma}_0 + \mathbf{\Gamma}_1 v_1^{\mathbf{B}} + \mathbf{\Gamma}_2 v_2^{\mathbf{B}} + \mathbf{\Gamma}_3 v_3^{\mathbf{B}} + \mathbf{\Gamma}_4 v_4^{\mathbf{B}}) \\
\mathbf{D} &= \frac{h^3}{12}(\mathbf{\Gamma}_0 + \mathbf{\Gamma}_1 v_1^{\mathbf{D}} + \mathbf{\Gamma}_2 v_2^{\mathbf{D}} + \mathbf{\Gamma}_3 v_3^{\mathbf{D}} + \mathbf{\Gamma}_4 v_4^{\mathbf{D}})
\end{aligned} \tag{2.21}$$

$$\mathbf{\Gamma}_0 = \begin{bmatrix} U_1 & U_4 & 0 \\ U_4 & U_1 & 0 \\ 0 & 0 & U_5 \end{bmatrix}, \mathbf{\Gamma}_1 = \begin{bmatrix} U_2 & 0 & 0 \\ 0 & -U_2 & 0 \\ 0 & 0 & 0 \end{bmatrix}, \mathbf{\Gamma}_2 = \begin{bmatrix} 0 & 0 & U_2/2 \\ 0 & 0 & U_2/2 \\ U_2/2 & U_2/2 & 0 \end{bmatrix},$$

$$\mathbf{\Gamma}_3 = \begin{bmatrix} U_3 & -U_3 & 0 \\ -U_3 & U_3 & 0 \\ 0 & 0 & -U_3 \end{bmatrix}, \mathbf{\Gamma}_4 = \begin{bmatrix} 0 & 0 & U_3 \\ 0 & 0 & -U_3 \\ U_3 & -U_3 & 0 \end{bmatrix} \tag{2.22}$$

where the invariant matrices ($\Gamma_i$, Equation (2.22)) contains the Tsai-Pagano material invariants $U_i$. Such invariants contain the unidirectional ply stiffness information. Therefore, they depend only on the material properties and not on the stacking sequence and can be derived from the elements reduced stiffness

matrix:

$$\begin{pmatrix} U_1 \\ U_2 \\ U_3 \\ U_4 \\ U_5 \end{pmatrix} = \begin{bmatrix} 3/8 & 3/8 & 1/4 & 1/2 \\ 1/2 & -1/2 & 0 & 0 \\ 1/8 & 1/8 & -1/4 & -1/2 \\ 1/8 & 1/8 & 3/4 & -1/2 \\ 1/8 & 1/8 & -1/4 & 1/2 \end{bmatrix} \begin{pmatrix} Q_{11} \\ Q_{22} \\ Q_{12} \\ Q_{66} \end{pmatrix} \tag{2.23}$$

By combining Equations (2.22) and (2.21), it is possible to obtain the relations between components of the ABD-matrix and the Tsai-Pagano material invariants. The relations for the membrane and bending matrices are:

$$\begin{pmatrix} A_{11} \\ A_{22} \\ A_{12} \\ A_{66} \\ A_{16} \\ A_{26} \end{pmatrix} = h \begin{bmatrix} 1 & v_1^{\mathbf{A}} & v_3^{\mathbf{A}} & 0 & 0 \\ 1 & -v_1^{\mathbf{A}} & v_3^{\mathbf{A}} & 0 & 0 \\ 0 & 0 & -v_3^{\mathbf{A}} & 1 & 0 \\ 0 & 0 & -v_3^{\mathbf{A}} & 0 & 1 \\ 0 & v_2^{\mathbf{A}}/2 & v_4^{\mathbf{A}} & 0 & 0 \\ 0 & v_2^{\mathbf{A}}/2 & -v_4^{\mathbf{A}} & 0 & 0 \end{bmatrix} \begin{pmatrix} U_1 \\ U_2 \\ U_3 \\ U_4 \\ U_5 \end{pmatrix} \tag{2.24}$$

$$\begin{pmatrix} D_{11} \\ D_{22} \\ D_{12} \\ D_{66} \\ D_{16} \\ D_{26} \end{pmatrix} = \frac{h^3}{12} \begin{bmatrix} 1 & v_1^{\mathbf{D}} & v_3^{\mathbf{D}} & 0 & 0 \\ 1 & -v_1^{\mathbf{D}} & v_3^{\mathbf{D}} & 0 & 0 \\ 0 & 0 & -v_3^{\mathbf{D}} & 1 & 0 \\ 0 & 0 & -v_3^{\mathbf{D}} & 0 & 1 \\ 0 & v_2^{\mathbf{D}}/2 & v_4^{\mathbf{D}} & 0 & 0 \\ 0 & v_2^{\mathbf{D}}/2 & -v_4^{\mathbf{D}} & 0 & 0 \end{bmatrix} \begin{pmatrix} U_1 \\ U_2 \\ U_3 \\ U_4 \\ U_5 \end{pmatrix} \tag{2.25}$$

For symmetric stacking sequences, where the **B** matrix is always zero, only eight parameters are required to model both the **A** and the **D** matrices. However, this number could be further reduced for some specific laminates. For example, it can be shown that laminates with only classical orientation ($[0°, \pm 45°, 90°]$) would result in both $v_4^{\mathbf{A}}$ and $v_4^{\mathbf{D}}$ being zero reducing the required number of lamination parameters to six. Another example is the case of balanced laminates, where both $v_2^{\mathbf{A}}$ and $v_4^{\mathbf{A}}$ are zero, reducing the required number of lamination parameters to six.

### 2.3.2 Feasible design space

Lamination parameters are tightly linked to a laminate stacking sequence via Equation (2.20) and, therefore cannot have arbitrary values. The region which defines physically meaningful lamination parameters is called the feasible lamination space. Such a domain is known to be convex (Grenestedt and Gudmundson, 1993) and is available in closed form only for a limited number of combinations of the lamination parameters.

An example of closed-form feasible constraints is the one derived by Hammer et al. (1997). This set of constraints describes the analytical relationship between all four in-plane and between all four out-of-plane lamination parameters separately; no coupling between in-plane and out-of-plane lamination parameters is considered. For a laminate with four lamination parameters ($v_1$, $v_2$, $v_3$ and $v_4$) the feasible space for the **A** and **D** matrices is defined by Equation (2.26).

$$\begin{cases} 2v_1^2(1-v_3)+2v_2^2(1+v_3)+v_3^2+v_4^2-4v_1v_2v_4 \leq 1 \\ v_1^2+v_2^2 \leq 1 \\ -1 \leq v_i \leq 1,\ (i=1,...,4) \end{cases} \tag{2.26}$$

Recent efforts in deriving constraints that consider both in-plane and out-of-plane lamination parameters have been made by Raju et al. (2014) and Wu et al. (2013) by using Cauchy-Schwarz inequalities. Another approach has been proposed by Bloomfield et al. (2009a) and utilises a convex hull of the lamination parameter space obtained by a set of predefined ply angles. A different approach has been used by Bettebghor et al. (2019) where machine learning has been used to reconstruct a lamination parameters feasibility constraint starting from a database of stacking sequences.

In the present work, the in-plane and out-of-plane constraints derived by Raju et al. (2014) are used in conjunction with those presented in by Hammer et al. (1997) (Equation (2.26)). The constraints by Raju et al. (2014) are presented in AppendixA

### 2.3.3 MEMBRANE STIFFNESS VISUALIZATION

While lamination parameters offer many advantages, reconstructing the associated fiber direction is not straightforward. As introduced by Dillinger et al. (2013), to have a general understanding of the main in-plane stiffness distribution of a given **A** matrix, and therefore an idea of the main fiber direction, it is possible to calculate the normalised elastic modulus of elasticity ($\hat{E}_{11}(\theta)$) associated to the component $A_{11}$ along an axis rotated with an angle $\theta$ with respect to the axis of the laminate as:

$$\hat{E}_{11}(\theta) = \frac{1}{\hat{A}_{11}^{-1}(\theta)} \tag{2.27}$$

where **T** is the transformation matrix presented in Equation (2.6) and

$$\hat{\mathbf{A}}^{-1}(\theta) = \mathbf{T}^T \hat{\mathbf{A}}^{-1} \mathbf{T} \tag{2.28}$$

$$\hat{\mathbf{A}} = \frac{1}{h}\mathbf{A} \tag{2.29}$$

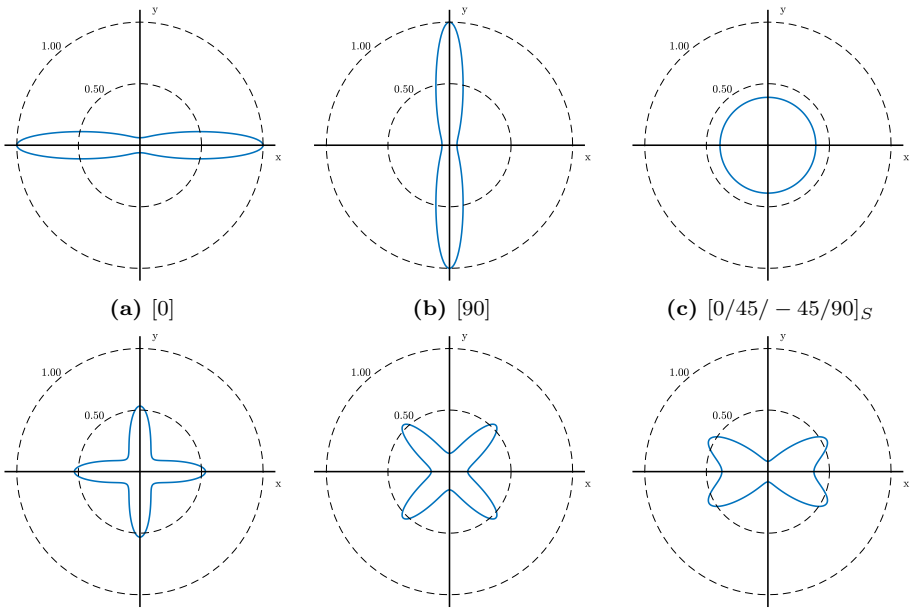


**(a)** [0] **(b)** [90] **(c)** $[0/45/-45/90]_S$

**(d)** $[0/90]_S$ **(e)** $[45/-45]_S$ **(f)** $[30/-30]_S$

**Figure 2.3:** $\hat{E}_{11}(\theta)$ stiffness distribution for some characteristic laminates.

A few characteristic examples of laminates and their corresponding membrane stiffness distributions are shown in Figure 2.3, where the $x$ axis represents the axis of the laminate and the $S$ at the end of a stacking sequence means that the stacking sequence is symmetric with respect to its mid-plane. The stiffness distributions presented here have all been normalised with respect to the maximum stiffness associated with the single unidirectional ply. When all fibers are oriented in the same direction, as in Figures 2.3a and 2.3b, the stiffness distribution is aligned with one direction, and this direction is indeed the fiber orientation. For quasi-isotropic laminates (Figure 2.3d), that is composed of plies in $[0/45/-45/90]$ directions in an equal ratio, the stiffness distribution is constant in all directions and have a magnitude of 0.40 with respect to the unidirectional ply. For laminates made with just two fiber directions, as in Figures 2.3c, 2.3f and 2.3e, the stiffness distributions are aligned with the two directions that compose the stacking sequences. Stiffness distribution plots are used throughout this dissertation to provide an indication of the main fiber directions.

## 2.4 BLENDING CONSTRAINTS



This section is based on the paper, *Derivation and application of blending constraints in lamination parameter space for composite optimisation* by T. Macquart, **M.T. Bordogna**, P. Lancelot and R. De Breuker, which appeared in Composite Structures volume 135, (2016), pp:224-235. Note: symbols may have been changed to maintain consistency throughout this thesis.

This section focuses on one of the main challenges in designing variable stiffness design, namely the blending. First introduced by Kristinsdottir et al. (2001), blending is essential to ensure structural continuity and avoid stress concentration during the design of variable stiffness composite structures, where thicknesses and ply orientations are locally optimised and may vary significantly between adjacent patches. Blending constraints have the objective of guaranteeing that some plies in the laminate stacking sequence span continuously between adjacent patches to improve their structural integrity.

Different definitions for blending have been proposed by different authors (Figure 2.4). Inner and outer blending definitions have been introduced by Adams et al. (2004). In these definitions, only the innermost and the outermost plies can be dropped. Two alternative definitions, the generalised and relaxed generalised blending, have been formulated by van Campen et al. (2008). Generalised blending requires all plies of the thinnest section to be continuous in the whole structure; relaxed generalised blending demands that no discontinuous plies should be in direct physical contact with each other. For the sake of clarity, throughout this dissertation, blending is always associated with the generalised blending definition of van Campen et al. (2008).

Macquart et al. (2016) introduced a set of blending constraints in the lamination parameters space that allows taking into account blending during gradient-based continuous optimisation. For the sake of completeness, these constraints are presented here, while the interested reader is invited to check the work from Macquart et al. (2016).

### 2.4.1 SINGLE IN-PLANE LAMINATION PARAMETER BLENDING CONSTRAINT

The general definition of lamination parameters introduced with Equation (2.20) can be rewritten as Equation (2.30) if the laminate is made with plies composed

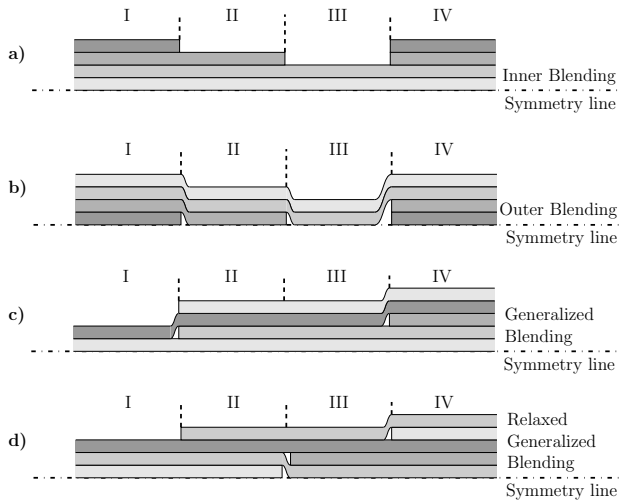


**Figure 2.4:** Four different definitions of blending: a) inner, b) outer, c) generalised and d) relaxed generalised blending. Original figures from van Campen et al. (2008).

of the same material and with the same ply thickness.

$$
\begin{aligned}
(v_1^{\mathbf{A}}, v_2^{\mathbf{A}}, v_3^{\mathbf{A}}, v_4^{\mathbf{A}}) &= \frac{1}{N}\sum_{i=1}^{N}(\cos(2\theta_i), \sin(2\theta_i), \cos(4\theta_i), \sin(4\theta_i)) \\
(v_1^{\mathbf{D}}, v_2^{\mathbf{D}}, v_3^{\mathbf{D}}, v_4^{\mathbf{D}}) &= \frac{4}{N^3}\sum_{i=1}^{N}(z_i^3 - z_{i-1}^3)\,(\cos(2\theta_i), \sin(2\theta_i), \cos(4\theta_i), \sin(4\theta_i))
\end{aligned}
\tag{2.30}
$$

where $z_i = -N/2 + i$.

The key concept in the derivation of the blending constraints with respect to lamination parameter is to quantify the change in lamination parameters between adjacent patches due to ply-drops (Figure 2.5).

Consider the first in-plane lamination parameters for a laminate with N-plies $v_{1,(N)}^{\mathbf{A}}$ and drop X-plies from the laminate to obtain $v_{1,(N-X)}^{\mathbf{A}}$. The complete stacking sequence is denoted by the set $\mathbf{S}$, the dropped plies are a subset of $\mathbf{S}$ called $\mathbf{D}$ and the plies in common between the two patches are a subset of $\mathbf{S}$ called $\mathbf{K}$, where $\mathbf{K} = \mathbf{S} - \mathbf{D}$. The change in $v_1^{\mathbf{A}}$ due to any number $X$ of ply-drops can

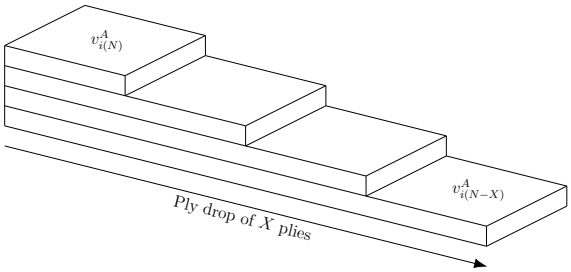


**Figure 2.5:** Multi-section laminate and ply-drops illustration.

be quantified according to Equation (2.33).

$$v^{\mathbf{A}}_{1,(N)} = \frac{1}{N}\sum_{\substack{i=1\\ i\in\mathbf{S}}}^{N}\cos(2\theta_i) \tag{2.31}$$

$$v^{\mathbf{A}}_{1,(N-X)} = \frac{1}{N-X}\sum_{\substack{i=1\\ i\in\mathbf{K}}}^{N}\cos(2\theta_i) \tag{2.32}$$

$$\Delta v^{\mathbf{A}}_{1,(N\to N-X)} = v^{\mathbf{A}}_{1,(N)} - v^{\mathbf{A}}_{1,(N-X)} = \underbrace{\frac{1}{N}\sum_{\substack{i=1\\ i\in\mathbf{D}}}^{N}\cos(2\theta_i)}_{\substack{\text{Term containing the}\\ \text{dropped plies}}} + \underbrace{\left(\frac{1}{N}-\frac{1}{N-X}\right)\sum_{\substack{i=1\\ i\in\mathbf{K}}}^{N}\cos(2\theta_i)}_{\substack{\text{Term containing the plies}\\ \text{present in both patches}}} \tag{2.33}$$

The maximum and minimal change of lamination parameters occur, respectively, for some "extreme" laminates where $[\theta_{i\in\mathbf{K}}, \theta_{i\in\mathbf{D}}] = [0°, 90°]$ and $[\theta_{i\in\mathbf{K}}, \theta_{i\in\mathbf{D}}] = [90°, 0°]$ for which the value of $\Delta v^{\mathbf{A}}_{1,(N\to N-X)}$ is:

$$\max_{(\theta_{i\in\mathbf{K}},\theta_{i\in\mathbf{D}})} ||\Delta v^{\mathbf{A}}_{1,(N\to N-X)}|| = 2\frac{X}{N} \tag{2.34}$$

Performing the same calculations for the remaining in-plane lamination parameters (i,e. $v^{\mathbf{A}}_{2,3,4}$) it is found that $2(X/N)$ is always the maximum change magnitude:

$$||\Delta v^{\mathbf{A}}_{k,(N\to N-X)}|| \leq 2\frac{X}{N}, \qquad \text{for } k = 1,2,3,4 \tag{2.35}$$

Equation (2.35) restrains the change of a single in-plane lamination parameter, occurring from a symmetrical laminate with N-plies due to X-ply-drop.

### 2.4.2 AGGLOMERATED IN-PLANE LAMINATION PARAMETERS BLENDING CONSTRAINT



Simultaneous change of more than one in-plane lamination parameter is presented here by introducing an Euclidean distance between multiple varying lamination parameters. The Euclidean distance in Equation (2.36) is associated with the radius of the feasible lamination parameter change reachable by a laminate with N plies subjected to an X ply-drops. The situation is illustrated in Figure 2.5.

$$E^{ip}_{12,(N\to N-X)} = \sqrt{\left(\Delta v^{\mathbf{A}}_{1,(N\to N-X)}\right)^2 + \left(\Delta v^{\mathbf{A}}_{2,(N\to N-X)}\right)^2} \tag{2.36}$$

Similarly to individual in-plane lamination parameter, it can be shown that the maximal Euclidean distance occurs for "extreme" laminates. In this context, "extreme" laminates refer to laminates where all $\theta_{i\in\mathbf{K}}$ kept in the adjacent patches and all $\theta_{i\in\mathbf{D}}$ dropped have the same orientation (e.g. $[\theta_{i\in\mathbf{K}}, \theta_{i\in\mathbf{D}}] = [90°, 0°]$). As result, $\Delta v^{\mathbf{A}}_{1,(N\to N-X)}$ and $\Delta v^{\mathbf{A}}_{2,(N\to N-X)}$ can be rewritten as:

$$\begin{aligned}\left[\left(\Delta v^{\mathbf{A}}_{1,(N\to N-X)}\right)_{\text{ext}}\right]^2 &= \left[\frac{1}{N}\sum_{\substack{i=1\\ i\in\mathbf{D}}}^{N}\cos(2\theta_i) + \left(\frac{1}{N}-\frac{1}{N-X}\right)\sum_{\substack{i=1\\ i\in\mathbf{K}}}^{N}\cos(2\theta_i)\right]^2 \\ &= \left[\frac{X}{N}\cos(2\theta_{i_\mathbf{D}}) - \frac{X}{N}\cos(2\theta_{i_\mathbf{K}})\right]^2 \\ &= \left[\cos(2\theta_{i_\mathbf{D}}) - \cos(2\theta_{i_\mathbf{K}})\right]^2 (X/N)^2 \\ &= \left(C_1^2 + C_3^2 - 2C_1C_3\right)(X/N)^2\end{aligned} \tag{2.37}$$

$$\begin{aligned}\left[\left(\Delta v^{\mathbf{A}}_{2,(N\to N-X)}\right)_{\text{ext}}\right]^2 &= \left[\frac{1}{N}\sum_{\substack{i=1\\ i\in\mathbf{D}}}^{N}\sin(2\theta_i) + \left(\frac{1}{N}-\frac{1}{N-X}\right)\sum_{\substack{i=1\\ i\in\mathbf{K}}}^{N}\sin(2\theta_i)\right]^2 \\ &= \left(S_1^2 + S_3^2 - 2S_1S_3\right)(X/N)^2\end{aligned} \tag{2.38}$$

where $[C_1, C_3] = [\cos(2\theta_{i_\mathbf{D}}), \cos(2\theta_{i_\mathbf{K}})]$ and $[S_1, S_3] = [\sin(2\theta_{i_\mathbf{D}}), \sin(2\theta_{i_\mathbf{K}})]$. Using Equations (2.37) and (2.38) it is possible to rewrite the Euclidean distance (2.36)

as:

$$E^{ip}_{12,(N\to N-X)} = (X/N)^2 \left[ \underbrace{\left(C_1^2 + C_3^2 - 2C_1C_3\right)}_{\text{from } (\Delta V^A_{1,(N\to N-X)})^2} + \underbrace{\left(S_1^2 + S_3^2 - 2S_1S_3\right)}_{\text{from } (\Delta V^A_{2,(N\to N-X)})^2} \right] \\ = f_{12}(\theta_{i_{\mathbf{D}}}, \theta_{i_{\mathbf{K}}})(X/N)^2 \tag{2.39}$$

where $f_k(\theta_{i_{\mathbf{D}}}, \theta_{i_{\mathbf{K}}})$ denote the sum of cosine and sine functions for the "extreme" laminates, and $k$ refers to the lamination parameters considered (e.g. in this case 12). The maximum Euclidean distance is obtained by maximizing $f_{12}(\theta_{i_{\mathbf{D}}}, \theta_{i_{\mathbf{K}}})$, resulting in:

$$\max_{\theta_{i_{\mathbf{D}}}, \theta_{i_{\mathbf{K}}}} \left[ \left( E^{ip}_{12,(N\to N-X)} \right)^2 \right] = 4(X/N)^2 \tag{2.40}$$

According to Equation (2.40), the maximum change in lamination parameters $v_1^{\mathbf{A}}$ and $v_2^{\mathbf{A}}$ beyond which no blendable solution can be found is again a function of the ply-drop ration $(X/N)$. A corresponding bi-dimensional blending constraint can, therefore, be written as Equation (2.41):

$$\left( \Delta v^{\mathbf{A}}_{1,(N\to N-X)} \right)^2 + \left( \Delta v^{\mathbf{A}}_{2,(N\to N-X)} \right)^2 - 4(X/N)^2 \leq 0 \tag{2.41}$$

by applying Equation (2.41) to a laminate on 20 plies and a ply-drop of 4 plies (Figure 2.6), it can be seen that the retrieved constraint well constraints all 16 plies blended solutions. Considering that the constraints have been retrieved by using "extreme" laminates and that such laminates are never used because they do not satisfy most of the basic manufacturing rules introduced in Section 2.2, a shrinking factor $\alpha$ can be added further reduce the design space:

$$\left( \Delta v^{\mathbf{A}}_{1,(N\to N-X)} \right)^2 + \left( \Delta v^{\mathbf{A}}_{2,(N\to N-X)} \right)^2 - 4\alpha(X/N)^2 \leq 0 \tag{2.42}$$

Generalising, the Euclidean distance expressing a change in all four in-plane lamination parameters is expressed as

$$\left( E^{ip}_{1234,(N\to N-X)} \right)^2 = \sum_{k=1}^{4} \left( \Delta v^{\mathbf{A}}_{k,(N\to N-X)} \right)^2 \tag{2.43}$$

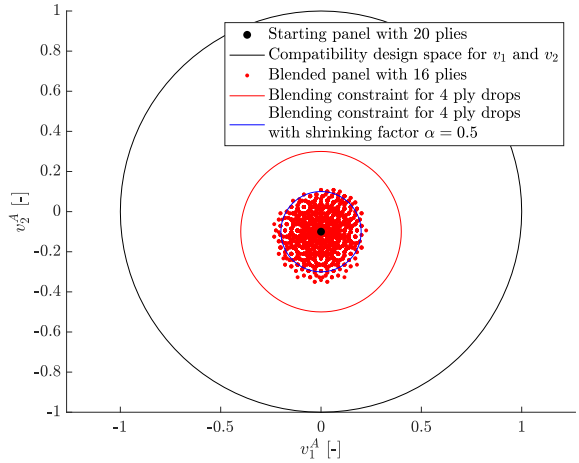


**Figure 2.6:** Illustrative example of the reduced feasible blended lamination parameter space of a stacking sequence of 20 plies due to 4 ply-drops.

and its value for "extreme" laminates is:

$$\begin{aligned}\left[\left(E^{ip}_{1234,(N\to N-X)}\right)_{\text{ext}}\right]^2 &= \left[\left(C_1^2+C_3^2-2C_1C_3\right)+\left(S_1^2+S_3^2-2S_1S_3\right)+\right.\\ &\left.\left(C_2^2+C_4^2-2C_2C_4\right)+\left(S_2^2+S_4^2-2S_2S_4\right)\right](X/N)^2\\ &= f_{1234}(\theta_{i_\mathbf{D}},\theta_{i_\mathbf{K}})(X/N)^2\end{aligned} \tag{2.44}$$

in which the coefficients are:

$$[C_1,C_2,C_3,C_4] = [\cos(2\theta_{i_\mathbf{D}}),\cos(4\theta_{i_\mathbf{D}}),\cos(2\theta_{i_\mathbf{K}}),\cos(4\theta_{i_\mathbf{K}})] \tag{2.45}$$

$$[S_1,S_2,S_3,S_4] = [\sin(2\theta_{i_\mathbf{D}}),\sin(4\theta_{i_\mathbf{D}}),\sin(2\theta_{i_\mathbf{K}}),\sin(4\theta_{i_\mathbf{K}})] \tag{2.46}$$

From Equation (2.44), the generalised constraint for different in-plane lamination parameters with shrinking $\alpha$ factor can be written as:

$$\left(E^{ip}_{k,(N\to N-X)}\right)^2 \leq \left(\max_{\theta_{i_\mathbf{D}},\theta_{i_\mathbf{K}}} f_k(\theta_{i_\mathbf{D}},\theta_{i_\mathbf{K}})\right)\alpha(X/N)^2, \qquad \text{for } k=1,2,3,4 \tag{2.47}$$

A representation of $f_k(\theta_{i_\mathbf{D}},\theta_{i_\mathbf{K}})$ for the first three in-plane lamination parameters (i.e. 1-3) is presented in Figure 2.7 while a list of maximal values for $f_k(\theta_{i_\mathbf{D}},\theta_{i_\mathbf{K}})$ is presented in Table 2.1 for different combination of lamination parameters. Finally, the blending constraint (2.47) is presented in Figure 2.8 for the reduced dimension case where $k=1,2,3$.

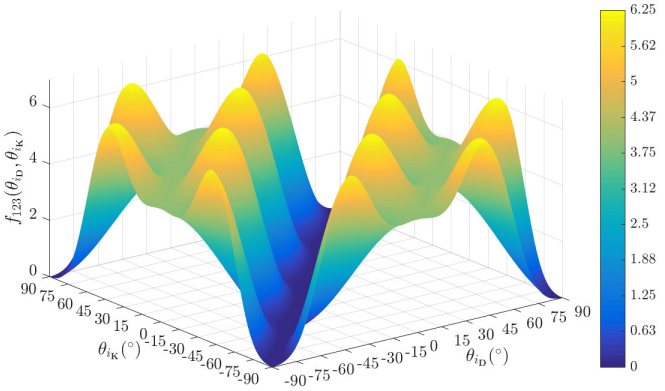


**Figure 2.7:** Coefficient function $f_k(\theta_{i_\mathbf{D}}, \theta_{i_\mathbf{K}})$ for the combination of in-plane lamination parameters 123. Original from Macquart et al. (2016).

| Values of $k$ | Combination of lamination parameters | $\max_{\theta_{i_\mathbf{D}}, \theta_{i_\mathbf{K}}} f_k(\theta_{i_\mathbf{D}}, \theta_{i_\mathbf{K}})$ |
|---|---|---|
| 1, 2, 3, 4, 12, 34 | $v_1, v_2, v_3, v_4, v_1 + v_2, v_3 + v_4$ | 4 |
| 13, 23 | $v_1 + v_3, v_2 + v_3$ | 5.1443 |
| 14, 24, 123, 124, 134, 234, 1234 | $v_1 + v_4, v_2 + v_4, v_1 + v_2 + v_3, v_1 + v_2 + v_4, v_1 + v_3 + v_4, v_2 + v_3 + v_4, v_1 + v_2 + v_3 + v_4$ | 6.25 |

**Table 2.1:** Maximal values of $f_k(\theta_{i_\mathbf{D}}, \theta_{i_\mathbf{K}})$ for all combinations of in-plane lamination parameters

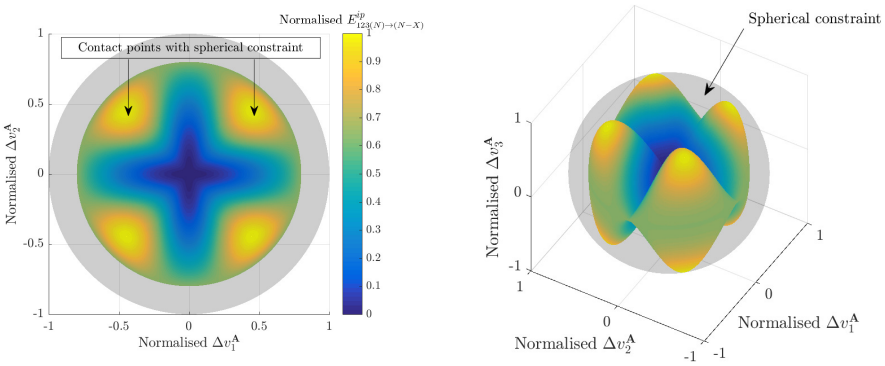


**Figure 2.8:** Normalised Euclidean distance for "extreme" laminates contained into a sphere of radius 1. Originals from Macquart et al. (2016).

### 2.4.3 SINGLE AND AGGLOMERATED OUT-OF-PLANE LAMINATION PARAMETER BLENDING CONSTRAINT

The same approach used in the previous two subsections can be used for the derivation of the single and agglomerated out-of-plane lamination parameters blending

constraints. However, the location of the dropped plies influences the **D** matrix while it doesn't influence the **A** matrix. Therefore, in order to simplify the derivation of the blending constraints for the **D** matrix, only symmetric laminates with an even number of plies are considered, and plies are dropped two by two. This means that a 2X ply-drop is obtained by removing X plies from the top half of the stacking sequence and X plies from the bottom half of the stacking sequence, resulting in a 2X ply-drop that is symmetric around the laminate mid-plane. The out-of-plane blending constraints for a ply-drop of 2X is equal to:

$$\left(E^{oop}_{k,(N\rightarrow N-2X)}\right)^2 \leq \left(\max_{\theta_{i_{\mathbf{D}}},\theta_{i_{\mathbf{K}}}} f_k(\theta_{i_{\mathbf{D}}},\theta_{i_{\mathbf{K}}})\right)\alpha\left[2\left(3\left(\frac{X}{N}\right)-6\left(\frac{X}{N}\right)^2+4\left(\frac{X}{N}\right)^3\right)\right]^2$$
$$\text{for } k=1,2,3,4 \tag{2.48}$$

Also, in this case, the retrieved blending constraint (Equation (2.48)) results in a change of lamination parameter that is a function of the ratio $X/N$. It should be noted that all the derived constraints are very conservative since they do not take into account any manufacturing rules apart from symmetric stacking sequence rules. Therefore, a shrinking factor $\alpha$ is added to reduce the design space.

### 2.4.4 AGGLOMERATED IN-PLANE AND OUT-OF-PLANE LAMINATION PARAMETERS BLENDING CONSTRAINT

The Euclidean distance is used again to agglomerate all in-plane and all out-of-plane lamination parameters into a single blending constraint, resulting in:

$$\left(E^{ip,oop}_{k,(N\rightarrow N-2X)}\right)^2 \leq \Bigg[\underbrace{\left(\max_{\theta_{i_{\mathbf{D}}},\theta_{i_{\mathbf{K}}}} f_k(\theta_{i_{\mathbf{D}}},\theta_{i_{\mathbf{K}}})\right)\alpha_{ip}(2X/N)^2}_{\text{in-plane}}$$
$$+\underbrace{\left(\max_{\theta_{i_{\mathbf{D}}},\theta_{i_{\mathbf{K}}}} f_k(\theta_{i_{\mathbf{D}}},\theta_{i_{\mathbf{K}}})\right)\alpha_{oop}\left[2\left(3\left(\frac{X}{N}\right)-6\left(\frac{X}{N}\right)^2+4\left(\frac{X}{N}\right)^3\right)\right]^2}_{\text{out-of-plane}}\Bigg]$$
$$\text{for } k=1,2,3,4 \tag{2.49}$$

where $\alpha_{ip}$ and $\alpha_{oop}$ the two shrinking factors and the in-plane ply-drop now considers 2X ply-drops to be consistent with the out-of-plane contribution assumptions.

# 3

# HIGH-FIDELITY DRAG PREDICTION FOR FLEXIBLE WINGS: COMBINING MODEL REDUCTION AND SURROGATE MODELLING TECHNIQUES

The aerodynamic methods used in the preliminary design phase are usually divided into two categories. The first methods are the high-fidelity CFD simulations used primarily to estimate aircraft performance, such as aircraft drag, stability margins, maximum lift at low speeds, and corrections for lower-fidelity methods. These methods deliver accurate results but are very computationally expensive, limiting their use in optimisation. The second methods are low-fidelity and fast-to-run potential methods such as strip theory or panel methods like the doublet lattice method (DLM) or the vortex lattice method (VLM). These second methods are mainly used to determine the aerodynamic loads acting on the aircraft and, therefore, are used to size the structure. However, these low-fidelity methods are irrotational and inviscid, thus unsuitable for estimating aircraft drag as limited to induced drag only, while high-fidelity CFD computes the total drag and also decomposes it in its components (e.g. induced drag, viscous drag, form drag and wake drag).

A popular alternative to the direct use of CFD in optimisation processes is to construct a cheap-to-compute approximation model of the computationally expensive

CFD computations by statistical or empirical approaches. These approximation models are usually referred to as surrogate models or metamodels. Surrogate models express complicated relationships between the response (output) and the design variables (input) with relatively simple equations derived from machine learning, statistics and optimisation. Once constructed, these models require minimal computational effort to run and often allow retrieving gradient, making them ideal for optimisation. Some examples of surrogate models used in aero-structural optimisation can be found in Lebofsky et al. (2014); Paiva et al. (2010); Zhang et al. (2008).



The approach used in this dissertation is built around the commercial FE tool Nastran. Nastran's SOL144 (MSC Software, 2014a) and SOL200 (MSC Software, 2014b) solutions are capable of computing static aeroelastic loads and their sensitivities with respect to design variables using the doublet lattice method from Giesing et al. (1972), and are commonly used in the industry to perform aeroelastic optimisation with structural constraints. However, total drag cannot be properly captured because the panel methods are limited to computing induced drag only. To overcome this restriction, a surrogate model is built from rigid RANS computations to provide the total wing drag coefficient. The surrogate model ($\widetilde{C}_D$) can be written as in Equation (3.1), where $f()$ is the function of the surrogate model that has as input the aicraft angle of attack $\alpha$ and the wing elastic structural displacement $\mathbf{u}_E$.

$$C_D \approx \widetilde{C}_D = f(\alpha, \mathbf{u}_E) \tag{3.1}$$

This chapter presents the framework used to develop a high-fidelity CFD surrogate model for the drag coefficient of a flexible wing. In particular, Section 3.1 focuses on modal reduction and dimensionality reduction processes while Section 3.2 focuses on the selection and validation of the surrogate model. The application of these processes is presented in Section 6.1.

## 3.1 STRUCTURAL DISPLACEMENT DIMENSIONALITY REDUCTION

The direct use of the wing elastic structural displacement ($\mathbf{u}_E$) as input to the surrogate model is not viable, as this would mean building a model with the same dimensionality as the number of components inside ($\mathbf{u}_E$). To avoid this, the wing elastic displacement is approximated using a projection-based reduced-order model. The simplest approach is to project the displacement onto a modal-basis built using the structural modes of the structure under study as in Equation (3.2), where the basis can be truncated to use only the first $n_\phi$ modes as is shown in

Equation (3.3).

$$\mathbf{u}_E = \sum_{i=1}^{\infty} \boldsymbol{\phi}_i q_i = \boldsymbol{\Phi}\mathbf{q} \tag{3.2}$$

$$\tilde{\mathbf{u}}_E = \sum_{i=1}^{n_\phi} \boldsymbol{\phi}_i q_i = \tilde{\boldsymbol{\Phi}}\tilde{\mathbf{q}} \tag{3.3}$$



where $\boldsymbol{\Phi}$ is the full modal basis, $\tilde{\boldsymbol{\Phi}}$ is the truncated modal basis that contains only the first $n_\phi$ structural modes (i.e. $\tilde{\boldsymbol{\Phi}} = [\boldsymbol{\phi}_1\ \boldsymbol{\phi}_2\ ...\ \boldsymbol{\phi}_{n_\phi}]$), and $\mathbf{q}$ and $\tilde{\mathbf{q}}$ the full and truncated generalised coordinates resulting from the projection.

It should be noted that both the structural displacement and the modal basis used in Equation (3.3) depend on the structural stiffness matrix $\mathbf{K}$ and mass matrix $\mathbf{M}$ of the structure under consideration. Therefore, any change in the structure during optimisation will impact both structural modes and wing displacement. Thus, in order to guarantee a correct approximation of the displacements throughout the optimisation process, the surrogate model should either use a variable projection basis ($\tilde{\boldsymbol{\Phi}} = f(\mathbf{M}, \mathbf{K})$) or adopt a constant basis made to ensure small residual displacement ($\mathbf{u}_{res} = \mathbf{u}_E - \tilde{\mathbf{u}}_E$) across the design space. The latter approach is used in this dissertation.

The following two sections cover two separate model reduction steps. Section 3.1.1 focuses on reducing the number of vectors in the constant projection basis, while Section 3.1.2 combines different generalized coordinates to reduce the surrogate dimensionality further. The starting point for both steps is the creation of databases of structural modes and aeroelastic displacements obtained via a design of experiment (DOE). The DOE is structured as follows:

1. $N$ distinct structures are generated with different stiffness and mass distributions

2. From each of the structure, the first $n_\phi$ modal shapes vectors ($\boldsymbol{\phi}_i$, for $i = 1, \ldots, n_\phi$) and the aeroelastic displacements at trim conditions ($\mathbf{u}_E^i$) are computed. Each structure is trimmed independently. All the mode shape vectors from the different structures are grouped together to form the modal basis ($\boldsymbol{\Phi}^{ndof \times N n_\phi} = [\boldsymbol{\phi}_1, \ldots, \boldsymbol{\phi}_{N n_\phi}]$) and all the aeroelastic displacements are grouped together to form a matrix of aeroelastic displacements ($\mathbf{u}_E^{ndof \times N} = [\mathbf{u}_E^1, \ldots, \mathbf{u}_E^N]$).

3. The modal basis and the matrix of aeroelastic displacements are split into a training set and a test set. The training set is used to build the approximation model using the K-fold cross-validation (CV) method, while the test set is used specifically to assess the capability of the resulting model

to extrapolate from unseen data. The rule-of-thumb ratio of 80/20 (Hastie et al., 2017) is used to generate the training and the test sets.

The DOE process is represented in Figure 3.1.

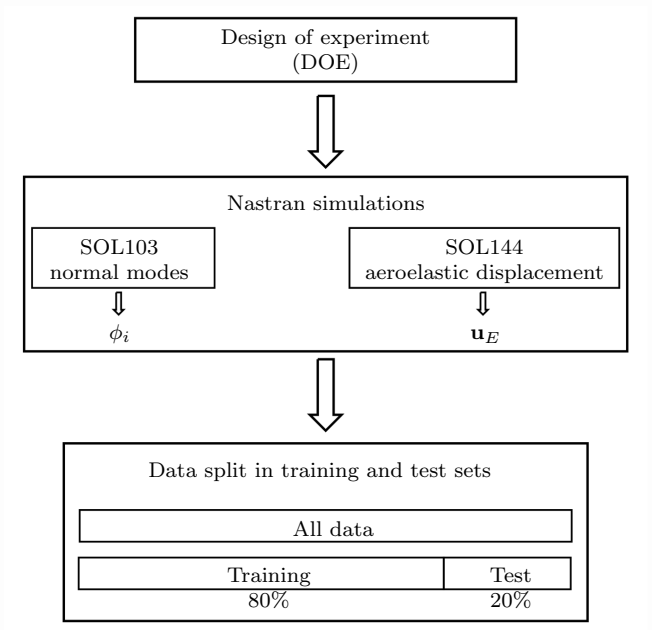


**Figure 3.1:** DOE process with retrieval of modal basis and aeroelastic displacement and final separation in the training and test set

### 3.1.1 PROJECTION BASIS DIMENSIONALITY REDUCTION USING SINGULAR VALUE DECOMPOSITION

The number of modes required to build an appropriate modal basis depends on the complexity of the structure, the scope of the model, and the requirements for the model's accuracy. In general, this basis can vary from about ten to tens of modes for a single structure, and its size is decided via a convergence study over the quantities of interest (e.g. displacement error). It is, therefore, difficult to understand a priori the required number of modes that shall be used.

To compute the constant projection basis $\tilde{\mathbf{\Phi}}$ and to reduce its dimensionality, a singular value decomposition (SVD) is applied to the training set of modal basis generated by the DOE to reduce the basis dimensionality. Matrix decomposition allows the decomposing of a matrix into a product of matrices to implement

efficient matrix algorithms or identify hidden patterns, such as the smallest orthogonal subset or the presence of redundant information. The identification of hidden patterns is especially important with a large quantity of data because such patterns could be used to reduce data dimensionality. The singular value decomposition is no exception and is widely used in signal/image processing, numerical analysis and big data.

The SVD decomposes a general rectangular matrix as in Equation (3.4) (Golub and Reinsch, 1970).



$$\tilde{\mathbf{\Phi}} = \mathbf{L}\mathbf{\Sigma}\mathbf{R}^T \tag{3.4}$$

where $\mathbf{\Sigma}$ is the diagonal matrix containing the singular values of $\tilde{\mathbf{\Phi}}$ and $\mathbf{L}$ and $\mathbf{R}^T$ are two orthonormal matrices in column space and row space, respectively. All the vectors in the matrices are linearly independent so that $\mathbf{L}$ and $\mathbf{R}^T$ are the smallest set of orthonormal vectors required to describe the column and row spaces. Additionally, the column and row vectors are ordered with respect to the magnitude of the singular values. This allows the creation of reduced orthonormal matrices by simply removing vectors associated with the lowest singular values. Thus, the reduced size projection basis can be computed as in Equation (3.5).

$$\tilde{\mathbf{\Phi}} \approx \tilde{\mathbf{L}} = [\boldsymbol{l}_1, \ldots, \boldsymbol{l}_{n_L}] \tag{3.5}$$

where only the first $n_L$ column vectors of $\mathbf{L}$ are retained in the reduced orthogonal basis $\tilde{\mathbf{L}}$.

As result, the structural displacements can be approximated as in Equation (3.6), where $\boldsymbol{p}$ is the column vector that contains the new generalized coordinates ($p_i$) obtained from projecting the wing elastic displacement over the orthogonal basis $\tilde{\mathbf{L}}$. By introducing Equation (3.6) in Equation (3.1), the function of the surrogate model can then be written as in Equation (3.7).

$$\tilde{\mathbf{u}}_E = \tilde{\mathbf{L}}\boldsymbol{p}, \text{ with } \tilde{\mathbf{L}} \text{ constant} \tag{3.6}$$

$$\widetilde{C}_D = f(\alpha, \mathbf{p}) \tag{3.7}$$

### 3.1.2 Generalized coordinates reduction using principal component analysis

So far, attention has been placed only on the dimensionality reduction of the projection basis, as this directly impacts the number of inputs required by the surrogate model. However, the non-correlation of the inputs should also be considered as this has three benefits: it improves the explainability of the surrogate model, it reduces the variance in regression coefficients and thus improves the

model performance with unseen data, and finally, it allows to reduce the dimensionality of the model further as redundant information can be removed (Golub and Reinsch, 1970) from the inputs. In addition, machine learning models might encounter numerical issues when fed with correlated inputs. In this section, a principal component analysis (PCA) is performed to eliminate the potential correlation between the generalized coordinates ($\boldsymbol{p}$) computed from Equation (3.6) and possibly further reduce the surrogate model dimensionality.



The principal component analysis (PCA) is an orthogonal transformation that converts a set of correlated variables into a new set of uncorrelated variables. PCA can be achieved by eigenvalue decomposition of a data covariance matrix (in this case $\frac{1}{2}\mathbf{P}\mathbf{P}^T$, where $\mathbf{P} = [\boldsymbol{p}_1, \ldots, \boldsymbol{p}_{n_L}]$) or singular value decomposition of a data matrix. Both approaches are applied after the data have been mean-centred as in Equation (3.8).

$$(\mathbf{P} - \mathbf{P}_{mean}) = \boldsymbol{\Psi}\mathbf{N} \tag{3.8}$$

where $\mathbf{N}$ contains as columns vector ($\boldsymbol{\nu}_i$) the new uncorrelated set of variable ($\nu_i$), or principal components. $\mathbf{P}_{mean}$ contains the mean values of $\mathbf{P}$ and allows to center the data and $\boldsymbol{\Psi}$ contains as columns the eigenvectors of the covariance matrix $\mathbf{P}^T\mathbf{P}$. The transformation matrix $\boldsymbol{\Psi}$ maps a data vector $\boldsymbol{p}_i$ from an original space to a new space of uncorrelated variables $\boldsymbol{\nu}_i$. Additionally, since the new variables are indexed by data variance, it is possible to truncate the transformation by simply retaining only the first $n_\Psi$ principal components and obtain a reduced-order representation of $\mathbf{P}$, $\tilde{\mathbf{P}}$.

$$\left(\tilde{\mathbf{P}} - \mathbf{P}_{mean}\right) = \tilde{\boldsymbol{\Psi}}\tilde{\mathbf{N}} \tag{3.9}$$

where $\tilde{\boldsymbol{\Psi}}$ contains only the first $n_\Psi$ columns of $\boldsymbol{\Psi}$ and only the first $n_\Psi$ principal componets of $\mathbf{N}$ are used to approximate $\tilde{\mathbf{P}}$. By construction, the truncated reconstruction of $\mathbf{P}$ is the one that minimizes the total squared error $\left|\left|\mathbf{P} - \tilde{\mathbf{P}}\right|\right|^2$. As a result, a set of $n_L$ potentially correlated generalized coordinates $p_i$ can now be approximated with $n_\Psi$ uncorrelated principal components $\nu_i$ with minimum truncation error, where $n_\Psi < n_L$.

$$\boldsymbol{p} \approx \tilde{\boldsymbol{p}} = \tilde{\boldsymbol{\Psi}}\boldsymbol{\nu} + \boldsymbol{p}_{mean} \tag{3.10}$$

Therefore, by using Equations (3.6) and (3.10), the aeroelastic displacement can be then approximated as in Equation (3.11) such that the function of the surrogate model can be expressed as in Equation (3.12).

$$\tilde{\mathbf{u}}_E = \tilde{\mathbf{L}}(\tilde{\boldsymbol{\Psi}}\boldsymbol{\nu} + \mathbf{p}_{mean}), \text{ with } \tilde{\mathbf{L}}, \tilde{\boldsymbol{\Psi}} \text{ and } \mathbf{p}_{mean} \text{ constant} \tag{3.11}$$

$$\widetilde{C}_D = f(\alpha, \boldsymbol{\nu}) \tag{3.12}$$

### 3.1.3 SUMMARY AND TRUNCATION STRATEGY

The workflow presented in Sections 3.1.1 and 3.1.2 is summarized in Figure 3.2. At different points in the workflow, truncations are made to reduce the model dimensionality and the decision behind each truncation is based on the residual displacement quantification ($\mathbf{u}_{res}$) as shown in Figure 3.2. The number of vectors used in the projection basis, as well as the residual displacement error at each truncation, are presented in Section 6.1.



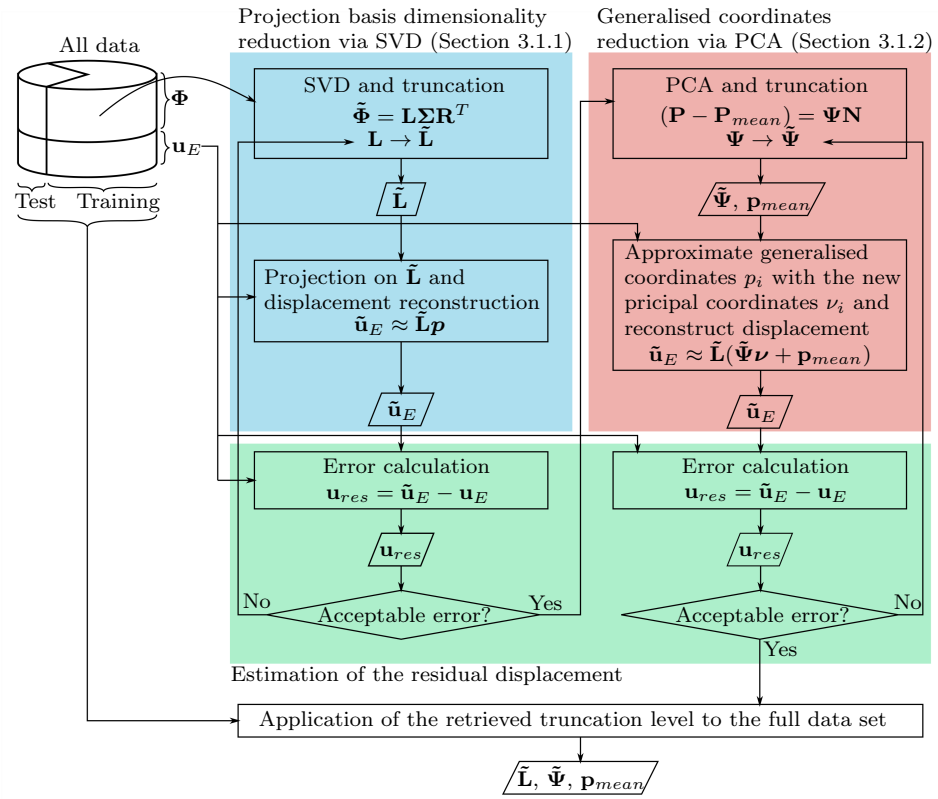


**Figure 3.2:** Workflow for projection basis dimensionality reduction via SVD, the subsequent generalised coordinates reduction via PCA with their respective estimation of residual displacement.

## 3.2 SURROGATE MODELLING TECHNIQUES

This section covers the list of techniques considered in this dissertation during the surrogate model creation. It presents also the processes used to create, evaluate,

tune, and finally select the most suitable model.

### 3.2.1 TECHNIQUES CONSIDERED FOR SURROGATE

For this work, only a few surrogate modelling techniques are investigated to obtain a robust surrogate for the wing drag coefficient. The models considered are:



1. Linear regression (LR);
2. Polynomial regression (PR);
3. Polynomial regression with elastic net regularization (PR-ENET);
4. Support vector machine with radial basis function kernel (SVM-RBF).

#### 3.2.1.1 LINEAR AND POLYNOMIAL REGRESSION MODELS

A linear regression model assumes a linear relationship between the input variables $\mathbf{x}^T = [x_1, \ldots, x_p]$ and the response $y$. The linear regression model can be written as:

$$\tilde{y} \approx \beta_0 + \sum_{i=1}^{p} x_i \beta_i \tag{3.13}$$

where $\tilde{y}$ is the function approximation, $\beta_i$ are the unknown coefficients and $x_i$ are the variables. Polynomial regression models are also represented by Equation (3.13), but in this case, $x_i$ are intermediate variables that represent the interactions between different variables of the system called $z_i$ (e.g. $x_3 = z_1^i \cdot z_2^j$). Regardless of the origins of the inputs $x_i$, the model is always linear in the parameters, and the $p+1$ unknowns $\beta_i$ are computed via the least-squares method by minimizing the residual sum of squares (RSS) in Equation (3.14).

$$RSS(\beta) = \sum_{i=1}^{N} (y_i - \tilde{y})^2 = \sum_{i=1}^{N} \left( y_i - \left( \beta_0 + \sum_{i=1}^{p} x_i \beta_i \right) \right)^2 \tag{3.14}$$

In this dissertation, the designation linear regression (LR) indicates the use of a model based on Equation (3.13) without intermediate variables. The designation polynomial regression (PR) will instead be used when $x_i$ are the intermediate variables used to model interaction and/or basis expansion of the variables $z_i$ (e.g. $x_3 = z_1^i \cdot z_2^j$)

For linear regression, no hyperparameters are involved in the model unless regularization techniques are used, while in polynomial regression, the hyperparameters

$k$, which indicate the polynomial degree, need to be tuned during the model's training.

#### 3.2.1.2 Linear and polynomial regression method with shrinkage

Shrinkage methods allow to retain a subset of the predictors and discarding the rest by introducing a penalty on the size of the regression coefficients. Thus resulting in models that are easier to interpret and potentially have a lower prediction error.



Three well-known shrinkage methods are the Ridge, the Lasso and the Elastic Net regressions (Hastie et al., 2017). In the case of Ridge regression, unknown coefficients $\beta_i$ are found through a simple linear system. In the case of Lasso or elastic-net regression, $\beta_i$ are found through more complex optimisation techniques. The residual sum of squares (RSS) of each regression is presented here, respectively:

$$RSS(\beta) = \sum_{i=1}^{N} \left( y_i - \left( \beta_0 + \sum_{i=1}^{p} x_i \beta_i \right) \right)^2 + \lambda \sum_{i=1}^{p} \beta_i^2 \tag{3.15}$$

$$RSS(\beta) = \sum_{i=1}^{N} \left( y_i - \left( \beta_0 + \sum_{i=1}^{p} x_i \beta_i \right) \right)^2 + \lambda \sum_{i=1}^{p} |\beta_i| \tag{3.16}$$

$$RSS(\beta) = \sum_{i=1}^{N} \left( y_i - \left( \beta_0 + \sum_{i=1}^{p} x_i \beta_i \right) \right)^2 + \lambda \sum_{i=1}^{p} \left( \alpha \beta_i^2 + (1-\alpha)|\beta_i| \right) \tag{3.17}$$

For all three methods, the hyperparameter $\lambda$ indicates the magnitude of the penalty and needs to be tuned during model training. The Ridge penalty ($\lambda \sum_1^p \beta_i^2$) limits the values of all unknown coefficients $\beta_i$, putting an upper limit to their values. The Lasso penalty ($\lambda \sum_1^p |\beta_i|$) is instead used to set some unknown coefficients $\beta_i$ to zero (see Figure 3.3) reducing the dimension of the model. This dissertation also considers the elastic-net penalty (PR-ENET) from Zou and Hastie (2005). The Elastic Net uses a linear compromise between Ridge and Lasso $\lambda \sum_1^p \left( \alpha \beta_i^2 + (1-\alpha)|\beta_i| \right)$, where the hyperparameter $\lambda$ indicates the magnitude of the penalty and $\alpha$ indicates the ratio between the Ridge and Lasso penalties.

#### 3.2.1.3 Support vector regression

Support vector regression (SVR) is a supervised learning model derived from the support vector machine (SVM) method for classification by Vapnik (1995). While the classification problem returns a discrete-valued output from a finite

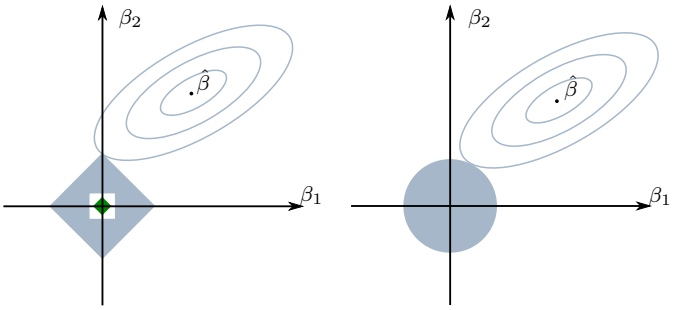


**Figure 3.3:** Representation of the Lasso and Ridge constraints on the RSS contours. Originals from Hastie et al. (2017)

set, the regression problem returns a continuous-valued output. SVR retains from SVM the capability of defining an acceptable error of the model thanks to the introduction of an $\epsilon$-insensitive region in the regression equation that ignores the errors of size less than $\epsilon$ (see Figure 3.4 and Equation (3.18)).

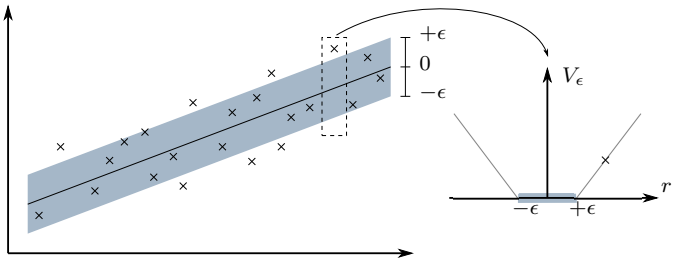


**Figure 3.4:** Representation of the $\epsilon$-insensitive region for a linear SVM. Original from Smola and Schölkopf (2004)

$$V_\epsilon(r) = \begin{cases} 0 & \text{if } |r| < \epsilon \\ |r| - \epsilon & \text{otherwise} \end{cases} \tag{3.18}$$

The linear regression model is written as in Equation (3.13), and the unknown $\beta_i$ are computed by minimising Equation (3.19).

$$H(\beta) = C \sum_{i=1}^{N} V_\epsilon \left( y_i - \left( \beta_0 + \sum_{i=1}^{p} x_i \beta_i \right) \right) + \frac{1}{2} \sum_{i=1}^{p} \beta_i^2 \tag{3.19}$$

where $V_\epsilon$ is the $\epsilon$-insensitive region presented in Equation (3.18). The introduction of the $\epsilon$-insensitive region enables the minimization problem to find a buffer zone that approximates the continuous-valued function and balances both model complexity and prediction error. This trade-off, between model complexity and deviations larger than $\epsilon$, is controlled by the constant $C$. Both $\epsilon$ and $C$ are hyperparameters of the linear SVR.

SVR can be made nonlinear by using kernels to map the data into a higher-dimensional space and perform linear SVR in the kernel space (Smola and Schölkopf, 2004). In this dissertation, a radial basis function (RBF), see Equation (3.20), the kernel is used where $\sigma$ is the additional hyperparameter.

$$k(x_i, x_j) = \exp\left(-\frac{||x_i - x_j||^2}{2\sigma^2}\right) \tag{3.20}$$



### 3.2.2 SURROGATE MODEL SELECTION PROCESS

Most of the models considered in this dissertation have hyperparameters that change the complexity of the model. Selecting the best-performing surrogate model means identifying which model and which hyperparameters minimize the average error when the model is used with independent test data.

The selection of the best surrogate model is divided into two steps:

1. Model selection refers to the process of estimating the performance of different models, adjusting any hyperparameters and choosing the best-performing model.

2. Model assessment refers to the prediction of how well the selected model performs with new data (generalization error)

In the ideal data-rich situation, the two problems are solved by randomly dividing the data into three subsets: a training set, a validation set and a test set. No general rule exists on how to partition the data into the three subsets, however, it is good practice to use the 50/25/25 split (Hastie et al., 2017). The training and the validation sets are used respectively to fit and estimate the performance of each model during model selection, while the test set is used to estimate the generalization error of the best-performing model during the model assessment.

Both the model selection and the model assessment steps rely on the mean squared error (MSE) to compute the performance of the model on their respective data sets. The MSE quantify the average error between the responses predicted by a model and the correct response for a given set of observations.

$$\text{MSE} = \frac{1}{n}\sum_{i=0}^{n}(y_i - \tilde{y}_i)^2 \tag{3.21}$$

The reason behind the division of the data into subsets is that low training MSE does not guarantee a low test MSE (Hastie et al., 2017). The risk is that, in order to minimize the training MSE, model complexity could be excessively increased,

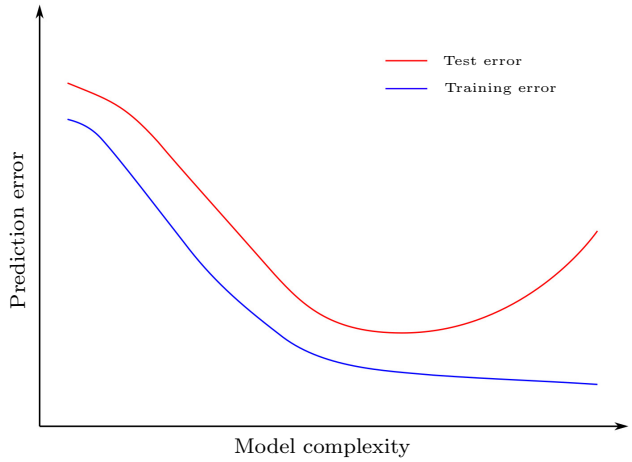


**Figure 3.5:** Representation of the behaviour of the test error and training error as a function of the model complexity. Original from Hastie et al. (2017)

resulting in an overfitted model that performs poorly against new data. This case is represented in Figure 3.5.

In case of scarcity of data, when it is impossible to divide the data into training, validation, and test sets, the K-fold cross-validation (CV) method is used. This method requires only the training and test sets as the training data are randomly split into $K$ equally sized folds. The first fold is then treated as a temporary validation set while the remaining $K-1$ folds are used to fit the model as the training set (see Figure 3.6). This procedure is repeated $K$ times, and each time the MSE is computed against the temporary validation set and stored. The full MSE from the K-fold CV is computed by averaging the stored MSE values as in Equation (3.22). Usual choices of $K$ are 5 or 10 (Hastie et al., 2017).

$$\mathrm{CV} = \frac{1}{k}\sum_{i=1}^{k}\mathrm{MSE}_i \tag{3.22}$$

During the model selection, the K-fold CV is performed for each model and the different values of the associated hyperparameters. The selected model is the model that, together with its hyperparameters, results in the lowest CV error. The selected model is then trained using both training and validation sets and tested against the test set to estimate the generalization error of the model.

In this dissertation, the selection of the most suitable surrogate model considers the cross-validation error but also the regression error characteristics (REC) (Bi and Bennett, 2003) area and the ease of implementation inside the commercial

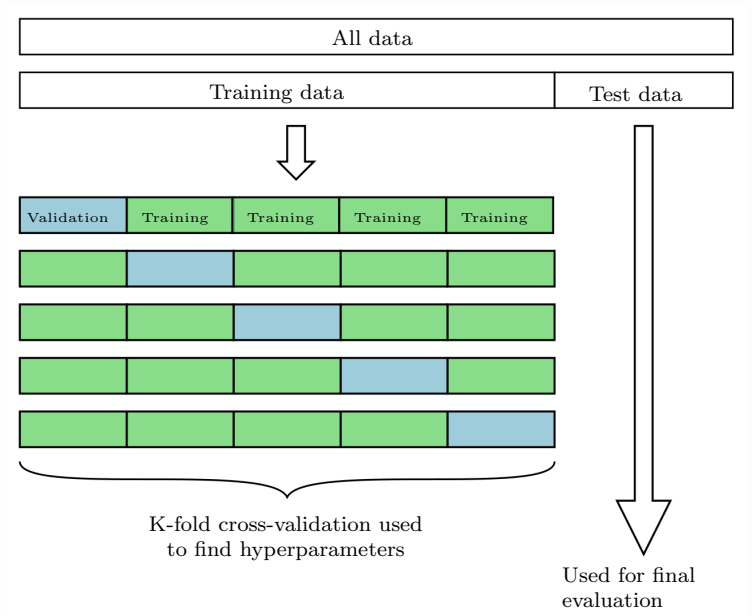


**Figure 3.6:** Schematic display of a K-fold cross-validation.

optimizers (i.e. Nastran). Application of the selection process is presented in Section 6.1.

# 4

# OPTIMISATION STRATEGY AND REGIONAL AIRCRAFT WING MODEL

This chapter is partially based on the industrial application paper, *Static and dynamic aeroelastic tailoring with composite blending and manoeuvre load alleviation* by **M.T. Bordogna**, P. Lancelot, D. Bettebghor and R. De Breuker, which appeared in Structural and Multidisciplinary Optimization, 2020, issue 61, pages 2193-2216. Note: symbols may have been changed to maintain consistency throughout this thesis.

This chapter introduces the regional aircraft wing model used in this dissertation as an application test case as well as the optimisation strategy. The wing model and the optimisation strategy are used in Chapters 5 and 6 to study, respectively, the effect of aeroelastic tailoring and blending constraints on the wing structural weight and the trade-off between wing structural weight and aerodynamic drag.

As introduced in Chapter 2, lamination parameters require a two-step optimisation approach where a continuous gradient-based optimisation is followed by an inverse optimisation problem that retrieves a discrete stacking sequence. The two steps are introduced in Sections 4.2 and 4.3, respectively. Section 4.2 also covers the integration of gust loads into the optimisation and the integration of the surrogate model of the aerodynamic drag inside the optimiser.

## 4.1 REGIONAL AIRCRAFT WING MODEL

This section introduces the model used in this dissertation as an application case. The model is an ONERA internal composite wing model of a regional aircraft.

### 4.1.1 FINITE ELEMENT MODEL

The finite element model is composed of shell and beam elements. The wing skins, shear ribs and spars have been modelled using shell elements, while beam elements represent stringers. The shell elements of the upper and lower wing skins are grouped to form sections in the spanwise and chordwise directions. The wing spars are also grouped in sections in the spanwise direction (Figure 4.1). All the elements in each section share the same thickness and material properties. The wing's internal structure is composed of 32 shear ribs and 13 stringers. Wing dimensions and characteristics are presented in Table 4.1.



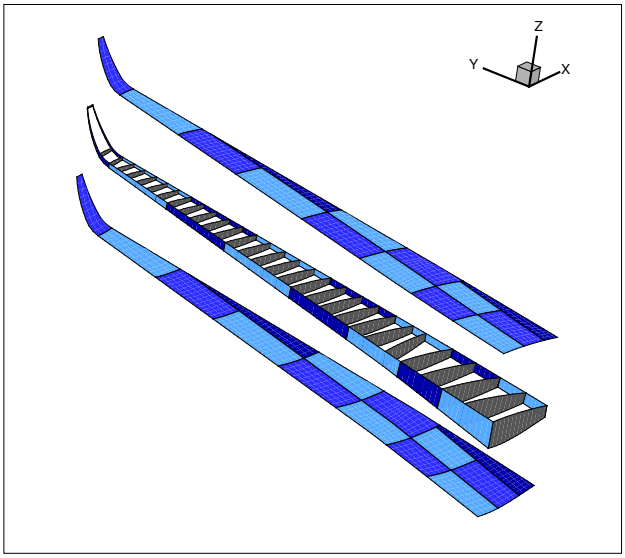


**Figure 4.1:** ONERA regional wing model with the main structural components. Each component shows the locations of the different locally optimised sections.

Two different fuel mass distributions have been considered in this dissertation, the maximum take-off weight (MTOW) and maximum landing weight (MLW), see Figure 4.2. A third mass distribution is the maximum zero fuel weight (MZFW), which is not considered in load calculation. The fuel is modelled as concentrated masses connected to the wing box FEM via multi-point connections. The amount of fuel along the spanwise direction has been estimated by consider-

**Table 4.1:** Wing dimensions and characteristics.

| Wing feature | Values |
|---|---|
| Half wingspan | 16.7 m |
| Wing area | 111 $m^2$ |
| Wing dihedral | 3.5° |
| Leading edge sweep angle | 18° |
| MTOW | 60 000 kg |
| MLW | 55 000 kg |
| MZFW | 50 000 kg |
| Design cruise Mach | 0.75 |
| Design cruise altitude | 35 000 ft |



ing the volume of each rib-bay, defined as the space between two consecutive ribs and the two spars, and the jet fuel density.

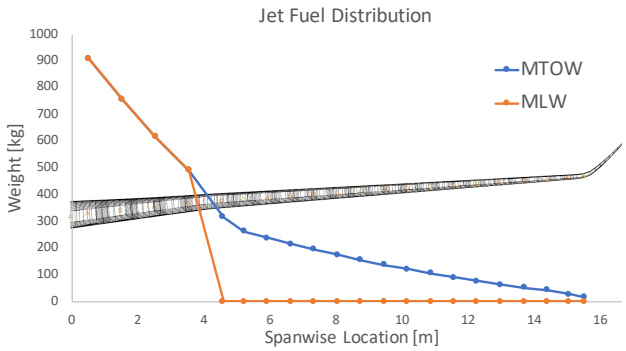


**Figure 4.2:** Two jet fuel distributions in the spanwise direction: MTOW and MLW.

### 4.1.2 Aerodynamic model

Two aerodynamic models have been used in this dissertation. The first model is a low-fidelity panel method for fast aeroelastic loads simulations, while the second model is a high-fidelity computational fluid dynamics model used to generate corrections for the low-fidelity method and perform the analysis required for the aerodynamic drag surrogate model.

#### 4.1.2.1 Doublet lattice model

The aeroelastic loads are calculated via the Nastran (MSC Software, 2014a) SOL144 static aeroelastic solution that utilises the doublet lattice method. Figure 4.3 shows the DLM panels mesh associated with the wing model.

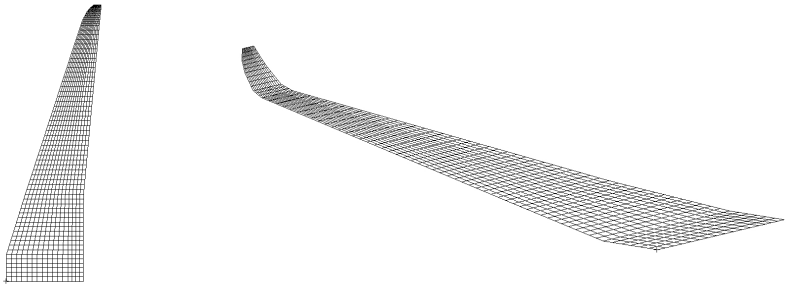

**(a)** Top view. **(b)** Iso view.

**Figure 4.3:** DLM mesh of the ONERA regional wing model.



As the aerodynamic loads coming from the DLM are used to perform the aircraft trim and to calculate the displacement required by the drag surrogate model, it is essential to correctly represent the spanwise and chordwise load distribution along the wing. This condition is achieved by using the concept of separation between the rigid and elastic load components, where the rigid part utilises rigid CFD results, and the elastic increment is computed via DLM. This method, often referred to as the Hybrid Static Approach (HSA) (Di Vincenzo, 2012), allows for consideration in the aeroelastic load computation for airfoil camber and wing twist law. This method not only ensures a more realistic lift distribution for structural sizing but also provides correct wing deflection input to the surrogate model, improving the fidelity of the drag evaluation.

#### 4.1.2.2 COMPUTATIONAL FLUID DYNAMIC MODEL

An aerodynamic mesh with 1 million cells is used to perform rigid CFD RANS analysis with the Spalart-Allmaras turbulence model. All simulations have been computed at Mach 0.75 and at 35 000 ft altitude which represents the cruise condition for this regional aircraft. The ONERA CFD solver elsA (Cambier et al., 2011) is used to perform all rigid aerodynamic computations. Figure 4.4 shows the fluid-structure interface mesh of the ONERA regional wing model.

The CFD model is used for two applications. The first is to compute drag coefficients $C_D$ for the surrogate model generation and assessment. The second is to correct the DLM model by providing rigid CFD data.

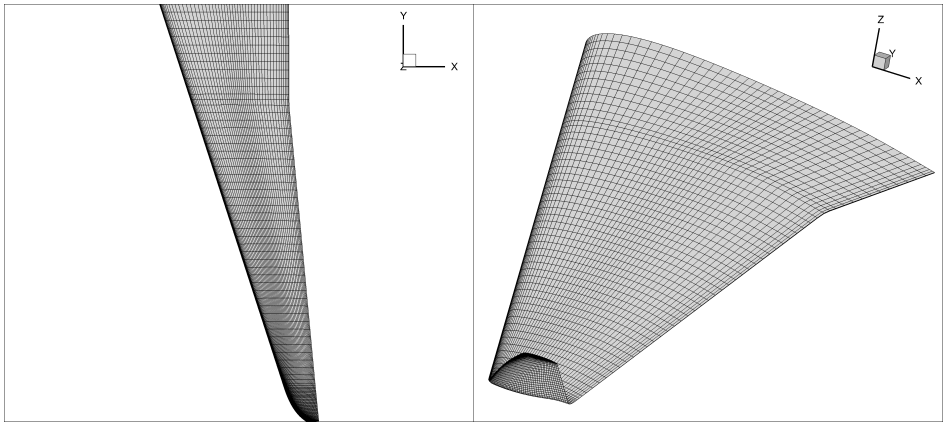


**(a)** Top view. **(b)** Iso view.

**Figure 4.4:** CFD mesh of the ONERA regional wing model.



## 4.2 Gradient-based optimization

The first step of the optimisation process is composed of a continuous optimisation where the optimal lamination parameters and section thicknesses are obtained through a gradient-based process performed via Nastran SOL200 (MSC Software, 2014b).

### 4.2.1 Design variables

As introduced in Section 4.1.1, the wing structural elements are grouped into sections sharing the same thickness and material properties. In total, there are 44 sections, 14 for each skin and 8 for each spar (Figure 4.1). All laminates are parameterised with lamination parameters and are assumed to be symmetric. Thus, each section has as 9 design variables, one thickness $t_i$ and eight lamination parameters $v_i^{\mathbf{A}}$ or $v_i^{\mathbf{D}}$ for a total of 396 design variables.

Shear ribs and stiffeners do not take part in the optimisation and are made of quasi-isotropic composite. Carbon fiber reinforced polymer (CFRP) is used in the structure, and its material properties are summarised in Table 4.2.

**Table 4.2:** Carbon fiber single-ply material properties.

| Property | Value |
|---|---|
| $E_{11}$ | 177 $GPa$ |
| $E_{22}$ | 10.8 $GPa$ |
| $G_{12}$ | 7.6 $GPa$ |
| $\nu_{12}$ | 0.27 |
| $\rho$ | 1500 $kg/m^3$ |
| $t_{ply}$ | 0.2 $mm$ |

### 4.2.2 COMPATIBILITY CONSTRAINTS



Compatibility constraints introduced in Section 2.3.2 ensure that lamination parameters are within the feasible design space and that the obtained **A** and **D** stiffness matrices are realistic.

In this dissertation, the compatibility constraints proposed by Hammer et al. (1997) (Equation (2.26)) and Raju et al. (2014) (see AppendixA) are used during the optimisation process.

### 4.2.3 MECHANICAL CONSTRAINTS

Two mechanical constraints are considered during the optimisation: strength and local buckling.

Strength constraints have been derived from the work of IJsselmuiden et al. (2008). This approach defines an analytical expression for a conservative failure envelope based on the Tsai-Wu failure criterion in strain space. This conservative failure envelope determines a region that guarantees no failure would occur within a laminate, irrespective of the ply orientation angles (Figure 4.5). The strength constraint is applied to all the elements of the structure.

Local buckling is applied to all regions of the wing skins delimited by two consecutive ribs and stiffeners, called buckling bays (see Figure 4.6). The closed formula in Equation (4.1) for buckling under biaxial loading of a simply supported plate is used.

$$\lambda_B = \pi^2 \frac{D_{11}(m/a)^4 + 2(D_{12} + 2D_{33})(m/a)^2(n/b)^2 + D_{22}(n/b)^4}{(m/a)^2 N_X + (n/b)^2 N_Y} \tag{4.1}$$

where buckling occurs for $0 < \lambda_B < 1$, $N_X$ and $N_Y$ are the stresses in the longitudinal and transverse directions, $D_{11}$, $D_{12}$, $D_{22}$ and $D_{33}$ are bending stiffness terms of the laminate, $a$ and $b$ are the corresponding region dimensions and $m$ and $n$ are the corresponding number of half-waves. This formula does not consider the effects of shear fluxes $N_{XY}$ and non-orthotropic composite bending stiffness

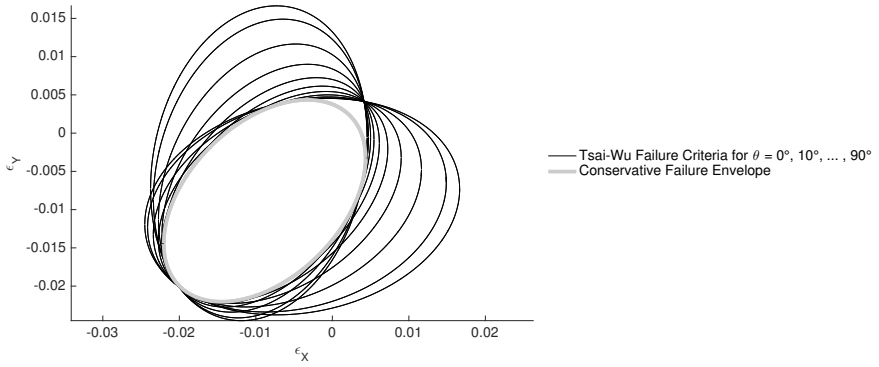


**Figure 4.5:** Strenght constrained derived by IJsselmuiden et al. (2008).

effects (i.e. $D_{13}$ and $D_{23}$ non-zero) into account. This approximation is known to be non-conservative and should be considered carefully (Bettebghor and Bartoli, 2012).

Both the strain values used in the strength constraints and the stress used for buckling computation are multiplied by 1.5 so that the structure is sized by ultimate loads.

### 4.2.4 Blending constraints

The blending constraints outlined in Section 2.4 apply to all sections of each main structural component but not cross-component. The four main structural components are the two wing skins and the two spars. This means, for example, that blending is applied to all sections of the upper wing skin only but not to the upper and lower wing skin simultaneously. The reason behind this choice is that usually, these four components are manufactured separately and then fastened mechanically together. Therefore, there is no need to guarantee ply continuity among them. A shrinking factor equal to 0.5 is applied to all blending constraints to help retrieve a blended solution.

### 4.2.5 Load cases

The regional wing model is optimised with respect to different load cases summarized in Table 4.3. In total, there are 18 load cases: 8 symmetric static manoeuvres and 10 gust load cases.

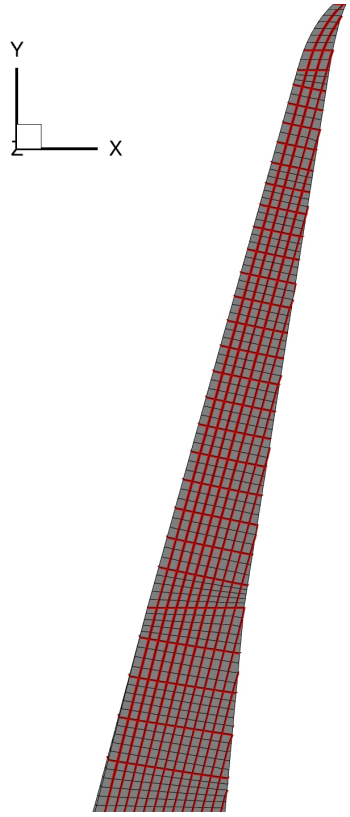


**Figure 4.6:** Difference between FE shell elements in black and buckling bays in red on the upper wing skin.

**Table 4.3:** List of the load cases used in the optimisation.

| N | Load factor ($g$) | Mach | Altitude ($ft$) | Mass configuration | Name |
|---|---|---|---|---|---|
| 1 | 2.5 | 0.48 | 0 | MTOW | Pull-up |
| 2 | -1 | 0.48 | 0 | MTOW | Push-down |
| 3 | 2.5 | 0.75 | 35000 | MTOW | Pull-up |
| 4 | -1 | 0.75 | 35000 | MTOW | Push-down |
| 5 | 2.5 | 0.48 | 0 | MLW | Pull-up |
| 6 | -1 | 0.48 | 0 | MLW | Push-down |
| 7 | 2.5 | 0.75 | 35000 | MLW | Pull-up |
| 8 | -1 | 0.75 | 35000 | MLW | Push-down |
| 9-18 | - | - | - | - | Gust 1-10 |

The 10 gust loads, as explained in more detail in Section 4.2.6, are the 10 worst gust loading conditions resulting from a gust selection process. The different gust profiles, taken from the certification CS-25 (EASA, 2018), are shown in Figure 4.7.

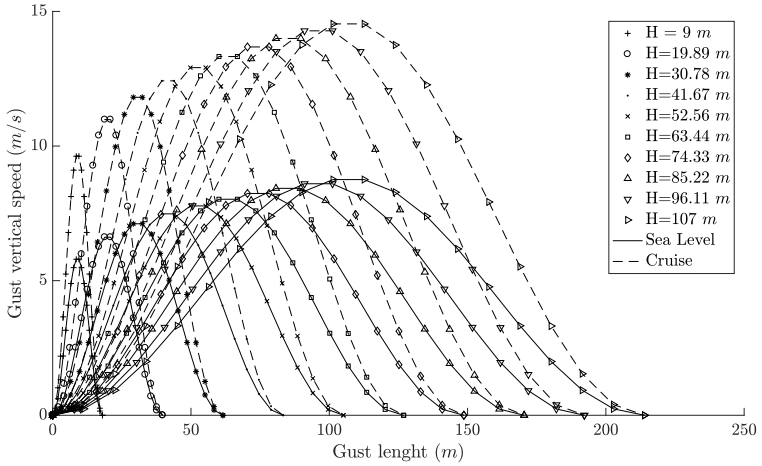


**Figure 4.7:** Gust profiles used at sea-level and cruise from CS-25 (EASA, 2018).



### 4.2.6 Inclusion of dynamic load cases

Dynamic aeroelastic analyses of discrete gusts are performed to ensure the wing satisfies the CS-25 certification requirements (EASA, 2018) for gust and turbulence loads. The CS-25 requires the aircraft to be subjected to discrete symmetrical vertical and lateral gusts at level flight.

#### 4.2.6.1 Gust analysis

In this dissertation, only positive and negative discrete symmetrical vertical gusts are taken into account. The "1-cosine" gust shape is defined according to EASA (2018) as in Equation (4.2).

$$U = \frac{U_{ds}}{2}\left[1 - \cos\left(\frac{\pi s}{H}\right)\right] \tag{4.2}$$

$$U_{ds} = U_{ref} F_g \left(\frac{H}{107}\right)^{1/6} \tag{4.3}$$

$$F_g = 0.5\left(1 - \frac{Z_{mo}}{76200} + \sqrt{\frac{MZFW}{MTOW}}\tan\left(\frac{\pi MLW}{4MTOW}\right)\right) \tag{4.4}$$

where $U$ is the gust velocity in equivalent airspeed (EAS) at position $s$, $s$ is the distance travelled inside the gust, $U_{ds}$ is the design gust velocity in EAS as defined

in Equation (4.3), $H$ is the gust gradient in meters, $U_{ref}$ is the reference gust velocity in EAS, $F_g$ the flight profile alleviation factor as defined in Equation (4.4) and $Z_{mo}$ is the maximum operating altitude in meters. The ONERA regional wing has an MTOW of 60 000 kg, an MLW of 55 000 kg, an MZFW of 50 000 kg and a maximum operating altitude $Z_{mo}$ of 12 192 m (40 000 ft). For gust computations, ten different gust gradients $H$ have been used from 9 m and 107 m (see Figure 4.7).

All gust encounters are simulated as a perturbation of the $1g$ steady-level flight. The Nastran dynamic aeroelastic solver (SOL146) is utilised to perform the gust analysis and to compute the responses (e.g. displacement, strain, etc.). To build up the full response, the incremental results from the gust analysis are superimposed on the $1g$ steady-level flight results.



#### 4.2.6.2 EQUIVALENT STATIC LOADS

In this dissertation, a gradient-based optimiser is used due to a large number of design variables. The main issue when computing for aeroelastic loads is their direct dependency on the design itself. For gust cases in particular, loads and sensitivities need to be recomputed not only for each design cycle but also for all gust cases and for all time instants. Such operations are computationally expensive; therefore, it is often difficult to include transient analysis directly in an optimisation process (Kang et al., 2006). Nonetheless, this process has been implemented in dedicated tools like the TU Delft Proteus aeroelastic code (Rajpal et al., 2019) and the Airbus Lagrange tool (Petersson, 2009). The Equivalent Static Load (ESL) method formalised by Kang et al. (2001) is used in this paper to bypass these issues.

The ESL aims at computing one or more equivalent static loads ($\mathbf{f}_{eq}$) capable of generating the same displacement fields of the transient load at different critical time steps. These $\mathbf{f}_{eq}$, now assumed as constant with respect to the structural design, are then applied to the FEM as static loads while the design is being optimised. Once the optimised design is obtained, a new set of transient analyses is performed to update $\mathbf{f}_{eq}$, and the loop is repeated until convergence of the optimisation. Therefore, the ESL method relies on a weak coupling between the transient simulations and the optimiser and requires several optimisation iterations before converging to a solution. The lack of sensitivities between the design variables and the transient responses constitutes one of the main drawbacks of this method. Therefore, design changes between two consecutive ESL loops need to be small enough to ease constraints satisfaction and convergence. In case of convergence issues, under-relaxation strategies could also be implemented. Still, this method can be implemented around already existing gradient-based optimisation tools and aeroelastic analysis code. The ESL has been used in various contexts, such as non-linear structures, multi-body dynamics, crash, and topology optimisation for the automotive industry. Most of these applications have

been summarised in Park (2006).

#### 4.2.6.3 Implementation of the equivalent static load

The flowchart of the ESL method used in this work is presented in Figure 4.8. The ESL method starts with the design variables ($\mathbf{x}$) of the optimisation problem being updated. This ensures that the latest wing design is used during the equivalent static load creation. The structural stiffness matrix $\mathbf{K}(\mathbf{x})$ is also computed and stored for later usage.

Nastran SOL146 is used to solve the governing equations of motion for the dynamic aeroelastic problem. Four separate gust load analyses are performed at different flight points (i.e. sea level and cruise) and for different mass configurations (i.e. MTOW and MLW). Once the time domain response is obtained for each analysis and for each gust gradient shown in Figure 4.7, different critical time instants are identified, and their associated displacement fields $\mathbf{u}_{gust}$ are extracted. Two criteria are used to identify the critical time steps: the maximum wing root bending moment and wingtip maximum deflections. Ten critical gust instants for each gust analysis are extracted across the gust gradients for a total of 40 stored displacement fields for all four gust analyses. As the wing is modelled as free-flying, the flexible structural displacements are obtained by removing the rigid body translations and rotations from the displacement vector of each grid point.

To include the $1g$ flight condition in the ESL method, four separated static aeroelastic analyses are performed using Nastran SOL144, one for each combination of flight point and mass configuration. The corresponding aeroelastic displacement field $\mathbf{u}_{1g}$ is computed and extracted.

The total displacement is obtained by superimposing the $1g$ and gust displacement fields associated with the same flight and mass configuration. The gust displacement field is added or subtracted to the cruise $1g$ displacement to obtain the effect of a positive or negative gust. This operation brings the total number of critical gust displacements from 40 to 80.

$$\mathbf{u}_{tot} = \mathbf{u}_{1g} \pm \mathbf{u}_{gust} \tag{4.5}$$

Once $\mathbf{u}_{tot}$ are retrieved, a set of equivalent static loads $\mathbf{f}_{eq}$ can be computed using Equation (4.6).

$$\mathbf{f}_{eq} = \mathbf{K}(\mathbf{x})\mathbf{u}_{tot} \tag{4.6}$$

$\mathbf{f}_{eq}$ allows a static analysis to achieve the displacement field that occurs during the dynamic response.

To further reduce the number of static analyses associated with the different equivalent static loads, a second selection of the most critical $\mathbf{f}_{eq}$ is performed

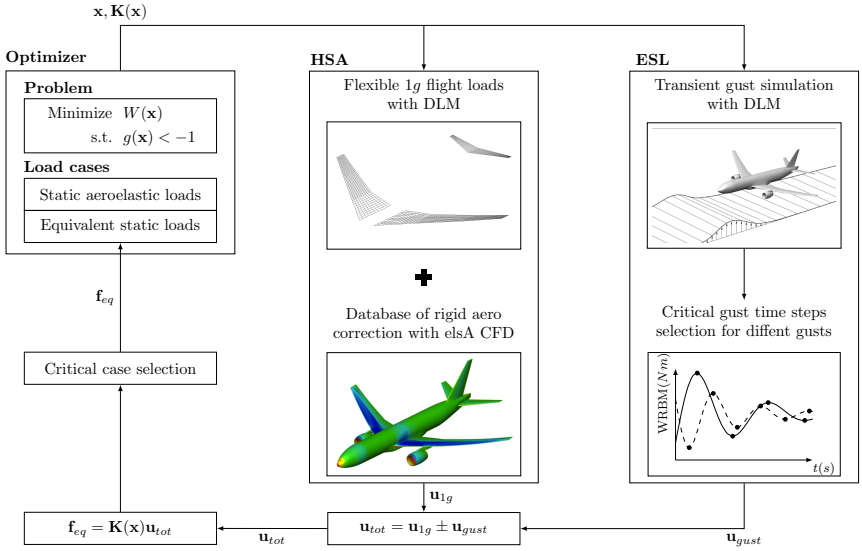


**Figure 4.8:** Overview of the equivalent static load process.

before their introduction in the optimiser. The selection is made by a static analysis performed via Nastran SOL101. The strength (Section 4.2.3) fields of all the 80 equivalent static loads are compared, and only the ten most critical loads are retained and added to the complete list of load cases (Table 4.3) sent to the optimiser module of Nastran SOL200.

### 4.2.7 INTEGRATION OF THE SURROGATE MODEL INSIDE THE OPTIMISER

Nastran allows two kinds of user-defined response functions, or second-level response functions, called DRESP2 and DRESP3. DRESP2 entities allow basic responses to be combined via algebraic equations defined by the user inside Nastran. On the other hand, DRESP3 allows an external program to be called during the optimisation and, therefore, is more suitable when the response cannot be obtained directly but through an iterative solution or a system of equations.

In this dissertation, the surrogate model and part of the structural displacement model reduction presented in Chapter 3 have been implemented inside an external FORTRAN program that is called during the optimisation by a DRESP3 function. The implementation is shown in Figure 4.9.

As shown in shown in Figure 4.9, all quantities obtained during the creation of

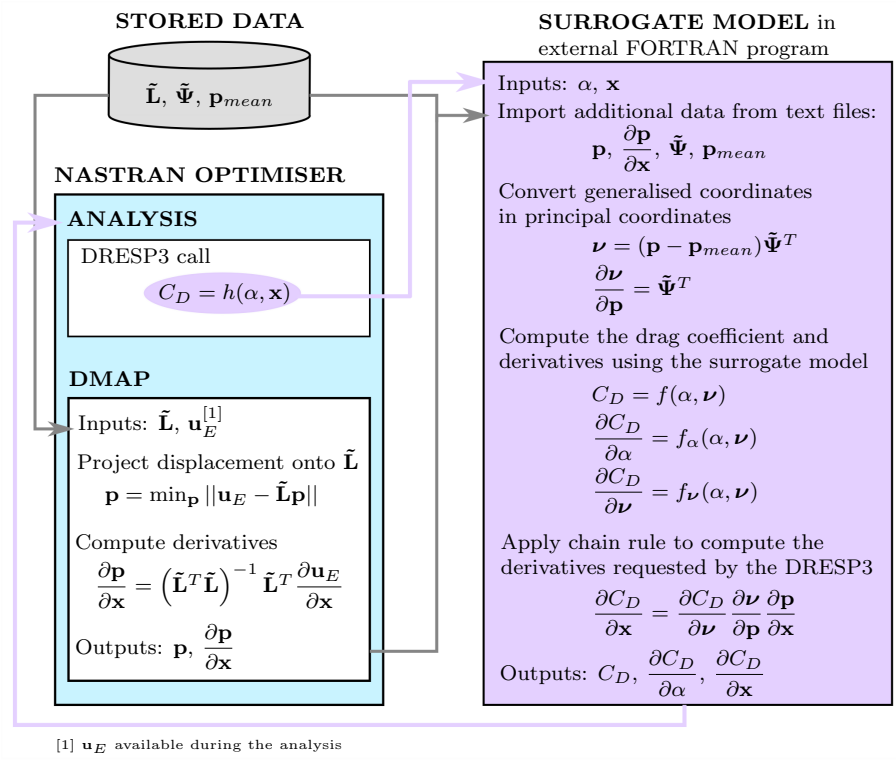


**Figure 4.9:** Workflow to include the surrogate model inside Nastran optimisation.

the wing displacement model reduction (i.e. $\tilde{\mathbf{L}}$, $\tilde{\mathbf{\Psi}}$, $\tilde{\mathbf{p}}_{mean}$), see Chapter 3, are stored in ASCII files and are accessible by both the optimiser and the external FORTRAN program.

The Nastran call to the external function is in the form of $C_D = h(\alpha, \mathbf{x})$, where $\alpha$ is the aircraft angle of attack and $\mathbf{x}$ are all the 396 design variables (i.e. thicknesses and lamination parameters) of the optimisation problem. All these quantities are available to the optimiser, and Nastran expects as output from the DRESP3 function the function value, $C_D$, plus all the derivatives of the function with respect to the inputs to carry on the optimisation (i.e. $\partial C_D/\partial\alpha$ and $\partial C_D/\partial\mathbf{x}$).

During the optimisation runs, a modified Nastran Direct Matrix Abstraction Program (DMAP) subroutine is used to perform the projection of the structural displacement, computed by the static aeroelastic solver, over the projection basis $\tilde{\mathbf{L}}$ and compute the generalised coordinates $\mathbf{p}$. In addition, the DMAP subroutine calculates the derivatives of the generalised coordinates $\mathbf{p}$ over the design variables ($\partial\mathbf{p}/\partial\mathbf{x}$). These two quantities ($\mathbf{p}$ and $\partial\mathbf{p}/\partial\mathbf{x}$) are computed in the background during Nastran execution and stored in an eternal text file.

Once the FORTRAN program is called by Nastran DRESP3 and receives the inputs $\alpha$ and $\mathbf{x}$, the external program accesses via ASCII file the stored constant quantities $\tilde{\mathbf{\Psi}}$, $\tilde{\mathbf{p}}_{mean}$ plus $\mathbf{p}$, $\partial\mathbf{p}/\partial\mathbf{x}$ computed by the DMAP subroutine. First, the generalised coordinates $\mathbf{p}$ are translated into principal components $\boldsymbol{\nu}$. Then, the surrogate model function (Equation (3.12) is used to compute the drag coefficient $C_D$ as well as its derivatives ($\partial C_D/\partial\alpha$ and $\partial C_D/\partial\boldsymbol{\nu}$). However, since the DRESP3 requires $\partial C_D/\partial\mathbf{x}$, the chain rule is applied to $\partial C_D/\partial\boldsymbol{\nu}$ using $\partial\mathbf{p}/\partial\mathbf{x}$ provided by DMAP and $\partial\boldsymbol{\nu}/\partial\mathbf{p}$ being the transposed PCA truncated matrix $\tilde{\mathbf{\Psi}}^T$ resulting in Equation (4.7).

$$\frac{\partial C_D}{\partial \mathbf{x}} = \frac{\partial C_D}{\partial \boldsymbol{\nu}} \frac{\partial \boldsymbol{\nu}}{\partial \mathbf{p}} \frac{\partial \mathbf{p}}{\partial \mathbf{x}} \tag{4.7}$$



It should be noted that even if the FORTRAN code has access to the design variables $\mathbf{x}$, it does not use them. Their inclusion in the DRESP3 is necessary so that Nastran can have the derivatives of the drag with respect to the design variables.

### 4.2.8 CENTRAL OPTIMIZATION PROBLEM

The blending constraints introduced in Section 2.4 limit the change of lamination parameters between all wing sections as a function of their difference in thickness. Applying those constraints while simultaneously optimising thickness and lamination parameters leads to a non-convex optimisation problem (Macquart et al., 2016). Therefore, a 4-stage strategy is employed during the gradient-based phase of the optimisation strategy, see Figure 4.10. This 4-stage strategy is used in all the applications presented in Chapters 5 and 6, so it is used not only with the composite blending constraints but also in conjunction with the equivalent static load and the surrogate model for aerodynamic performance. Figure 4.11 presents the overview of the full optimisation workflow used in this dissertation.

The 4-stage strategy is as follows. When the blending constraints are included in the optimisation, see Figure 4.10a, stage 1 of this strategy is a weight minimisation of the wing with respect to thicknesses and lamination parameters without blending constraints (Equation 4.8). This stage provides a feasible starting point before the introduction of the blending constraints. The unblended design ($\mathbf{x}_U$) is used as a starting point for stage 2, where the objective is still to minimise wing mass, but in this case, the blending constraints are included (Equation 4.9). In stage 3, a repair function rounds up the thicknesses of blended design ($\mathbf{x}_B$) to an even number of plies based on the ply thickness ($t_{ply}$). After the repaired design ($\mathbf{x}_R$), lamination parameters are optimised one last time in stage 4 while thicknesses are kept fixed with the intent of maximising the reserve factors of all the mechanical constraints (i.e. local buckling and strength from Section 4.2.3).

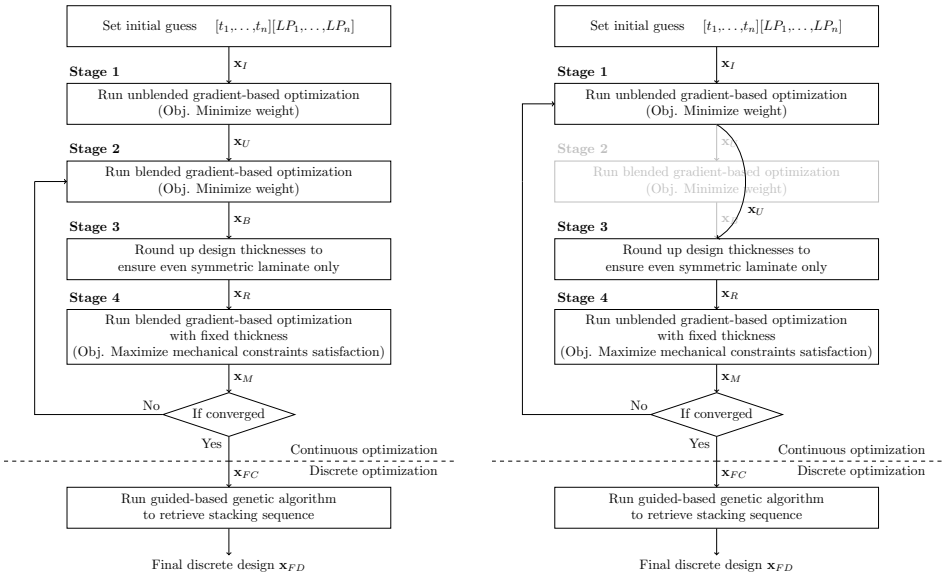


**(a)** With continuous blending constraints. Blending constraints are included in stages 2 and 4.

**(b)** Without continuous blending constraints. Stage 2 is not performed, and blending constraints are not included in stage 4.

**Figure 4.10:** Proposed bi-step optimisation and 4-stage strategy for continuous optimisation.

In this step, often referred to as margin maximization (Bettebghor and Bartoli, 2012; Haftka and Watson, 2005; Liu, 2001), the feasibility of the structure is maximised utilising a slack variable $s$ (Equation 4.10). Rounding of thicknesses and maximising of reserve factors modify the structure's stiffness, leading to internal load redistribution. Therefore, stages 2 to 4 are repeated until convergence to a final continuous design ($\mathbf{x}_{FC}$). Once an optimum design is reached, the stacking sequence retrieval via GA is used to retrieve a blended final discrete design ($\mathbf{x}_{FD}$), see Section 4.3.

In case blending constraints are not included in the optimisation, see Figure 4.10b, stage 2 is not performed, and stage 4 does not consider blending constraints during the optimisation. Stages 1, 3 and 4 are repeated until convergence.

$$\begin{aligned} \text{Minimize} \quad & W(t, v) \\ \text{subject to} \quad & \text{compatibility constraints} < -1 \\ & \text{strenght constraints} < -1 \\ & \text{local buckling constraints} < -1 \end{aligned} \tag{4.8}$$

$$\begin{aligned} \text{Minimize} \quad & W(t, v) \\ \text{subject to} \quad & \text{compatibility constraints} < -1 \\ & \text{blending constraints} < -1 \\ & \text{strenght constraints} < -1 \\ & \text{local buckling constraints} < -1 \end{aligned} \tag{4.9}$$

$$\begin{aligned} \text{Maximize} \quad & s \\ \text{subject to} \quad & \text{compatibility constraints} < -1 \\ & \text{blending constraints} < -1 \\ & \text{strenght constraints} + s < -1 \\ & \text{local buckling constraints} + s < -1 \end{aligned} \tag{4.10}$$

The gradient-based optimiser used is an interior point optimisation algorithm called IPOPT (Wächter and Biegler, 2006). Other optimisation algorithms could also be used. The approximation of the problem is obtained with the convex linearisation method (CONLIN), and all constraints are required to be smaller than $-1$ for ease of comparison during the optimisation runs.

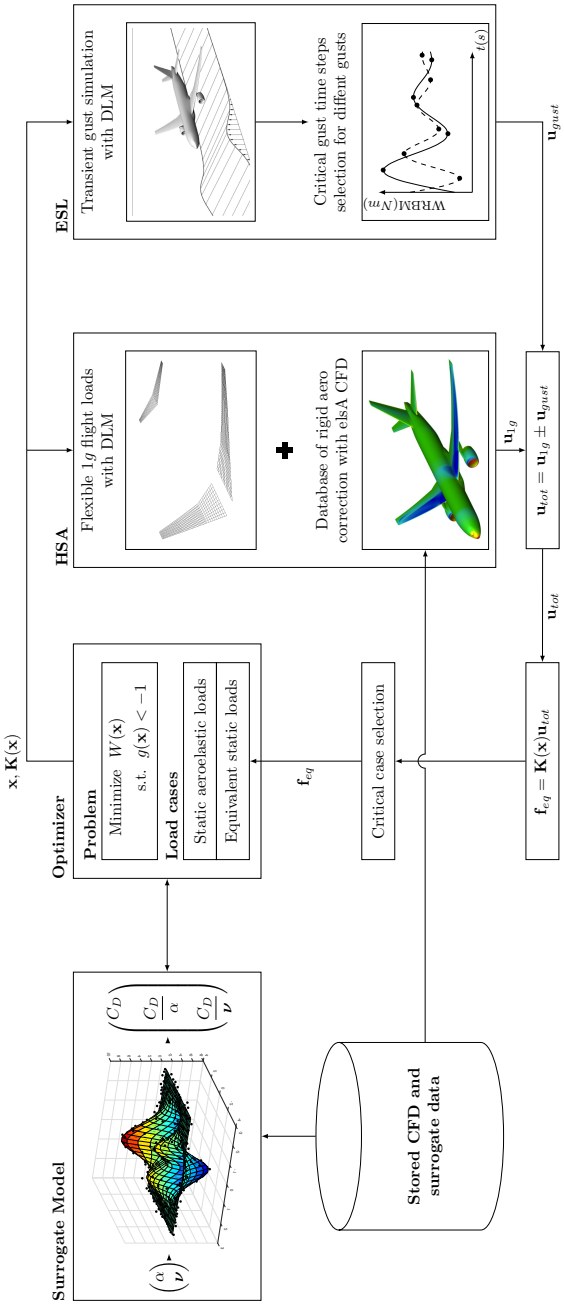


**Figure 4.11:** Overview of the gradient-based optimization workflow with equivalent static load and surrogate model.

## 4.3 STACKING SEQUENCE RETRIEVAL

The OptiBLESS open-source stacking sequence optimisation toolbox (Macquart, 2016) is used to retrieve manufacturable laminates [1]. OptiBLESS uses a guide-based genetic algorithm (GA) to retrieve blended stacking sequences matching the optimised lamination parameters achieved by the gradient-based optimiser (i.e. Nastran). According to the guide-based methodology (Adams et al., 2004), the thickest laminate is defined as the guide-laminate. Other laminates from the same structure are obtained by dropping plies from the guide-laminate, therefore ensuring the final design is blended. As a result, the plies of the thinnest laminate are ensured to span the entire structure.



After the continuous optimisation, each wing section is optimised in terms of laminate thickness and lamination parameters. The continuous design outcome is used as a target solution for the discrete stacking sequence retrieval. The thickest laminate within each main structural component (i.e. skins and spars) is identified and set as the guide. Next, the ply angles describing the guide laminate stacking sequence and ply drops are used as design variables in OptiBLESS. The genotype used in OptiBLESS to describe composite structures is given as in Equation 4.11, where $[\theta_1\ \theta_2\ ...\ \theta_n]$ reppresents the stacking sequence of the guide and $[\Xi_1\ \Xi_2\ ...\ \Xi_D]$ is the drop off table. The drop off table states what plies shall be removed from the guide to generate the remaining laminates of the structural component.

$$\text{Genotype} = \left[ \underbrace{[\theta_1\ \theta_2\ ...\ \theta_n]}_{\text{Ply angles}} \underbrace{[\Xi_1\ \Xi_2\ ...\ \Xi_D]}_{\text{Drop off}} \right] \tag{4.11}$$

The objective function used during the discrete optimisation represents the lamination parameter matching quality between the continuous and discrete retrieved design (Equation 4.12). In other words, OptiBLESS is set to retrieve blended stacking sequences matching the lamination parameters obtained at the end of the continuous optimisation. This objective function is expressed as the root mean square error (RMSE) between the continuous and discrete lamination parameters as shown in Equations (4.12) and (4.13).

$$\text{Fitness}(\boldsymbol{\theta}, \boldsymbol{\Xi}) = \frac{1}{N_{lam}} \sum_{s=1}^{N_{lam}} \text{RMSE}_s(\boldsymbol{\theta}, \boldsymbol{\Xi}) \tag{4.12}$$

$$\text{RMSE}_s(\boldsymbol{\theta}, \boldsymbol{\Xi}) = \sqrt{\frac{1}{8} \sum_{i=1}^{8} w_i \left( \overline{\mathbf{LP}}_{i,p} - \mathbf{LP}_{i,p}(\boldsymbol{\theta}, \boldsymbol{\Xi}) \right)^2} \tag{4.13}$$

[1] https://github.com/TMacquart/OptiBLESS

where $N_{lam}$ is the total number of laminate sections in a structural component (i.e. upper wing skin), $\overline{\mathbf{LP}}_{i,p}$ is the vector of target parameters for section $p$, $w_i$ is a weighting factor and $\mathbf{LP}_{i,p}$ is the vector of lamination parameters obtained by the GA. The weighting has been decided empirically with higher weights given to sections with a high number of failed elements after stacking sequence retrieval. Stacking sequences are converted into lamination parameters in order to evaluate the fitness using the following notation:

$$\mathbf{LP} = [v_1^{\mathbf{A}}\ v_2^{\mathbf{A}}\ v_3^{\mathbf{A}}\ v_4^{\mathbf{A}}\ v_1^{\mathbf{D}}\ v_2^{\mathbf{D}}\ v_3^{\mathbf{D}}\ v_4^{\mathbf{D}}] \tag{4.14}$$

According to the fitness function given in Equation (4.12), the best-retrieved stacking sequence would be a stacking sequence best matching the optimised lamination parameters obtained by Nastran.

# 5

# AEROELASTIC TAILORING WITH STATIC AND DYNAMIC LOAD-CASES AND BLENDING CONSTRAINTS

This chapter is partially based on the industrial application paper, *Static and dynamic aeroelastic tailoring with composite blending and manoeuvre load alleviation* by **M.T. Bordogna**, P. Lancelot, D. Bettebghor and R. De Breuker, which appeared in Structural and Multidisciplinary Optimization, 2020, issue 61, pages 2193-2216. Note: symbols may have been changed to maintain consistency throughout this thesis.

This chapter applies the optimisation strategy presented in Chapter 4 to the ONERA regional wing model introduced in Section 4.1. This application focuses on the weight minimisation of the composite wing and utilises the composite parameterisation and blending constraints introduced in Chapter 2.

A list of all the optimisation cases performed is presented in Section 5.1. Section 5.2 shows the effect of the blending constraints on the continuous optimisation introduced in Section 4.2. The relevance of static and dynamic loads on the final wing design are presented and discussed in Section 5.3. This section also focuses on the ESL and checks the reliability of the equivalent static load approach. Finally, Section 5.4 shows the results from the stacking sequence retrieval performed via the genetic algorithm introduced in Section 4.3.

## 5.1 OPTIMISATION CASES

To investigate the effects of the static/dynamic loads and blending constraints on the final design of the wing, four different optimisation cases are analysed:

- Case A corresponds to the weight minimisation under static loads with mechanical (i.e. strength and buckling) and compatibility constraints. This serves as a reference case for later comparisons.
- Case B is a weight minimisation with the same constraints used in case A but considers both static and dynamic loads. Comparison between cases A and B shows the impact of gust loads on the wing design.
- Case C is a weight minimisation with the addition of blending among constraints used during the optimisation. Only static loads are used in this case, so comparing cases A and C shows the effect of blending constraints on the wing design.
- Case D is a weight minimisation with both static and dynamic loads that also includes blending among the constraints. Comparing A and D shows the combined effect of including blending and dynamic loads.

A summary of the cases can be found in Table 5.1 together with their associated normalised optimal weight. In Table 5.1, two different normalized weight results are given: $\overline{W}$ and $\overline{W}_{NRU}$. $\overline{W}$ represent the weight results obtained with the processes introduced in Figure 4.10 where thicknesses are rounded up in stage 3 to the nearest upper multiple of $t_{ply}$. On the other hand, $\overline{W}_{NRU}$ is obtained with the same processes used for $\overline{W}$, but without the rounding up in stage 3. All results obtained without rounding up are here referred to with the subscript $(\cdot)_{NRU}$. All weights presented in this chapter are normalised with respect to the $NRU$ weight from case A.

**Table 5.1:** Weight for different optimisation problems.

| Case | Static | Dynamic | Blending | $\overline{W}_{NRU}$[%] | $\overline{W}$[%] |
|---|---|---|---|---|---|
| A | Yes | No | No | 100.00 | 102.16 |
| B | Yes | Yes | No | 100.05 | 102.16 |
| C | Yes | No | Yes | 105.01 | 107.50 |
| D | Yes | Yes | Yes | 105.14 | 108.04 |

The reason behind showing both weights is that the rounding-up step does not produce consistent results. For example, two designs with the same weights before rounding but with different thickness distributions may result in different rounded-up weights depending on how close the different thickness distributions are to an even multiple of $t_{ply}$. Therefore, $NRU$ weights are used in all weight comparisons

as $\overline{W}_{NRU}$ is the lowest but theoretical weight achievable by the optimisation process. In contrast, final design comparison and stacking sequence retrieval are made using the continuous rounded-up results as this is closer to a realistic aerospace application.

For the sake of clarity, only the meaningful outputs produced during the optimisation are presented in this chapter. All computed outputs are included in Appendix B.

## 5.2 Effect of blending constraints on continuous optimum

The effect of using blending constraints during the continuous optimisation is visible in Table 5.1. The introduction of the constraints results in an increase in mass of 5.01% from case A to C and of 5.14% from case B to D; this weight gap remains similar also after rounding up. This weight increase is expected since the blending constraints reduce the design space, as shown in Figure 2.6.



Figures 5.1, 5.2 and 5.3 show the thickness and stiffness distributions for the upper wing skin, lower wing skin and spars, respectively. Each figure presents the distributions for case A, case C, and the difference between the two cases. The stiffness distributions are presented with the membrane stiffness polar plots introduced in Section 2.3.3.

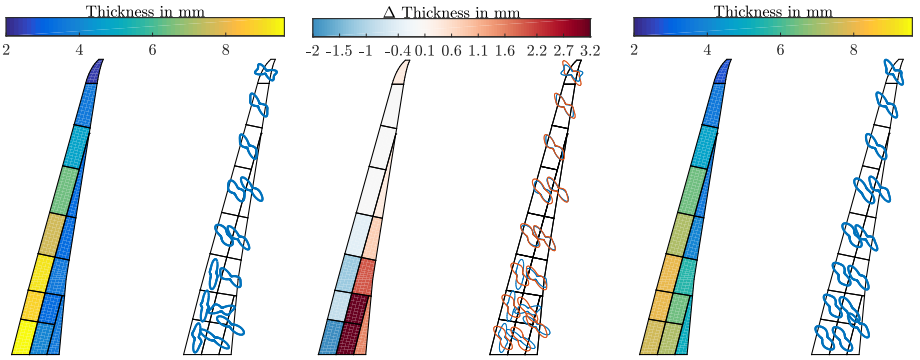


**(a)** Case A **(b)** Case A → Case C **(c)** Case C

**Figure 5.1:** Upper wing thickness and stiffness distributions for case A, case C and the difference between the two cases

Case A results in a wing with decreasing thickness from root to tip, with most of the skin's and spar's thickness concentrated at the leading edge. This solution results in a wing elastic axis that is close to the leading edge and thus creates

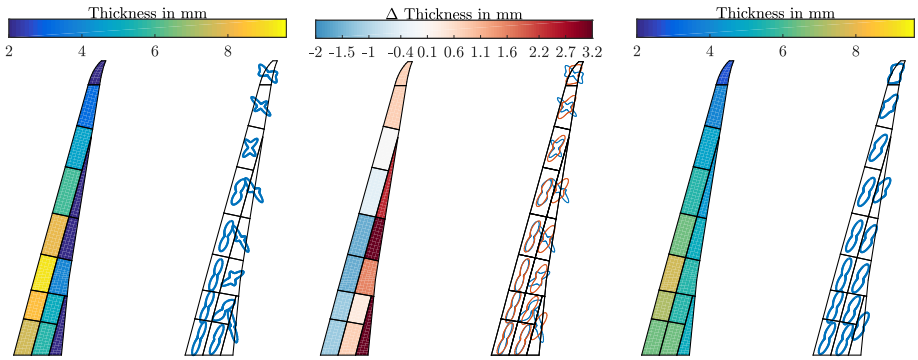


**(a)** Case A **(b)** Case A → Case C **(c)** Case C

**Figure 5.2:** Lower wing thickness and stiffness distributions for case A, case C and the difference between the two cases



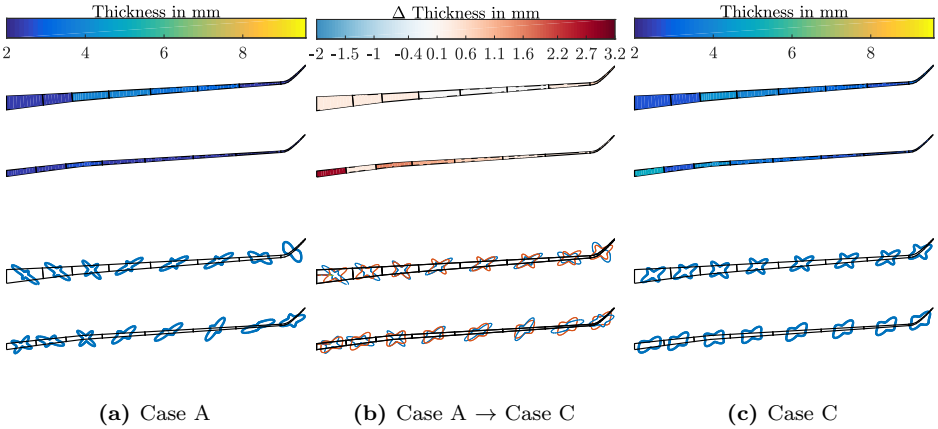


**(a)** Case A **(b)** Case A → Case C **(c)** Case C

**Figure 5.3:** Front and rear spar thickness and stiffness distributions for case A, case C and the difference between the two cases

a wing wash-out effect under bending that shifts the lift distribution towards the wing root, resulting in a lower root wing bending moment and hence light wing design. Including the blending constraints in case C preserves this thickness distribution towards the leading edge, creating a wash-out effect. However, the thickness change between adjacent panels is more gradual than in case A and is followed by a smoother change in stiffness distribution from wing root to tip. This is due to the connection between thickness drop and allowable change in lamination parameters introduced by the blending constraints.

Figures 5.4 present the distribution of the most critical mechanical constraints over wing skins and spars. The resolution of strength and buckling constraints

differ in the FE model as the strength constraint is applied on each FE shell element while buckling is applied on regions delimited by two consecutive ribs and stiffeners (called buckling bays) and only on the skins, this is explained in Section 4.2.3. Therefore, the most critical strength constraint among all the elements in a buckling bay is compared to the most critical buckling constraint for that particular bay. The resulting constraint and its associated load case are extracted and used in Figures 5.4 and 5.5 respectively. In Figure 5.5, the different aircraft configurations (i.e. MTOW and MLW) and flight conditions (i.e. sea-level and cruise altitude) associated with each manoeuvre have been grouped so that only the three manoeuvres are plotted (i.e. pull-up, push-over and gust)

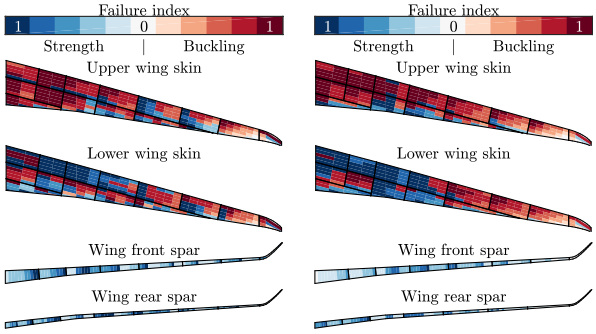


**(a)** Case A **(b)** Case C

**Figure 5.4:** Most critical failure index based on mechanical constraints at continuous optimum for cases A and C.

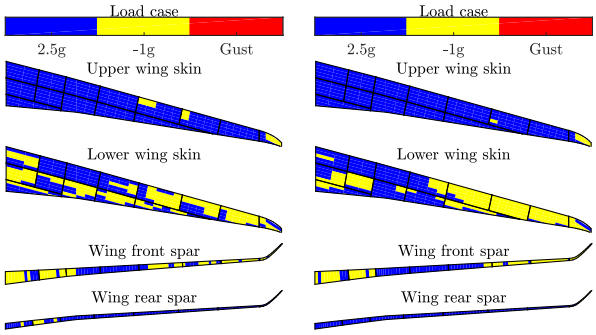


**(a)** Case A **(b)** Case C

**Figure 5.5:** Load-cases associated with the most active mechanical constraints at continuous optimum for cases A and C.

Figures 5.4 and 5.5 show that for both cases A and C, the upper wing skin has higher failure indices (FIs) in buckling, and the load case associated with such FIs is the $2.5g$ pull-up manoeuvre. For the lower skin, the higher FIs are a mix

between strength and buckling, where the former results from the $2.5g$ pull-up manoeuvre while the latter is from the $-1g$ push-over manoeuvre. Spars are only sized by strength, as no buckling has been considered during the optimisation for this component. Gust loads do not appear in Figure 5.5 as both cases A and C are only sized for static loads. The introduction of the blending constraints and their impact on the thickness and stiffness distributions does affect the most critical mechanical constraints and their associated load case. The tendency is that with blending, the wing is more clearly divided between strength-driven and buckling-driven regions.

The observations made in this chapter on the comparison between case A and case C can be made when comparing case B and case D. For the sake of brevity, this second comparison is not presented here. However, the results from cases B and D and their difference can be found in Appendix B.

5

## 5.3 EFFECT OF INCLUDING DYNAMIC LOADS ON CONTINUOUS OPTIMUM

Table 5.1 shows that for the composite regional wing model under study, the introduction of gust loads results in a marginal $NRU$ weight increment between 0.05% and 0.12%. This small weight increment is then either absorbed or augmented by the rounding up but remains substantially minimal, between 0% and 0.5%. The impact of including dynamic loads on the thickness and stiffness distributions of the upper wing skin, lower wing skin and spars are shown in Figures 5.6, 5.7 and 5.8 respectively. Each figure presents the distributions for case C, case D and the difference between the two cases. The stiffness distributions are presented with the membrane stiffness polar plots introduced in Section 2.3.3.

Including dynamic loads results in a mild change in the thickness and stiffness distributions if compared with the introduction of the blending constraints. The change in thickness removes material from the leading edge and increases it at the trailing edge. This change in thickness is followed by a change in stiffness direction at the same panels. Even if, for this application, the impact of dynamic loads is contained, the net result is that the optimiser modified both wing stiffness and thickness to withstand the additional dynamic load cases, showing the capabilities of aeroelastic tailoring and the importance of considering dynamic loads in preliminary design. The contained impact of the gusts on the final design of the regional wing model under study can also be seen in Figure 5.10. This figure shows how only a few areas are characterised by high mechanical constraints FI from the additional dynamic loads.

Figure 5.11 shows the highest strength and buckling constraint values obtained during the encounter of the ten gusts considered during the optimisation for all

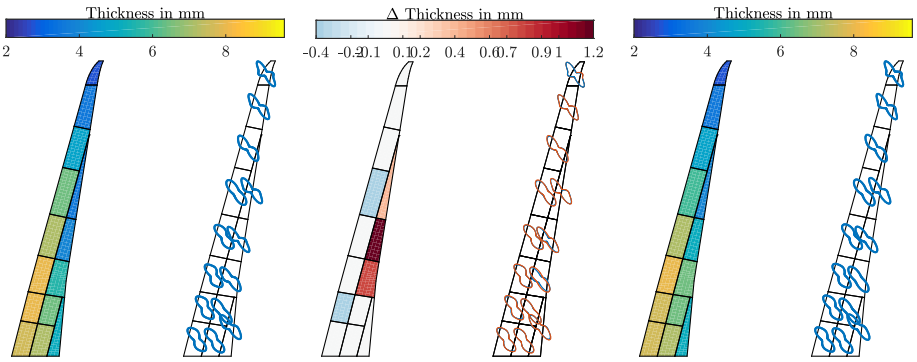


**(a)** Case C **(b)** Case C → Case D **(c)** Case D

**Figure 5.6:** Upper wing thickness and stiffness distributions for case C, case D and the difference between the two cases

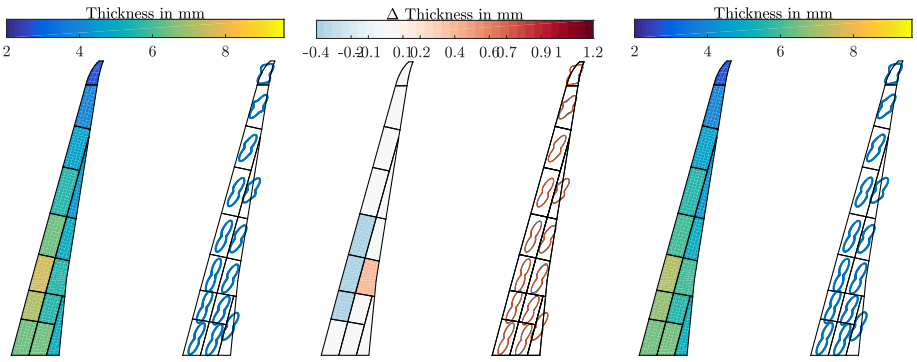


**(a)** Case C **(b)** Case C → Case D **(c)** Case D

**Figure 5.7:** Lower wing thickness and stiffness distributions for case C, case D and the difference between the two cases

flight conditions and mass configurations. Even if the impact of gust loads is marginal, as in the application case used in this dissertation, it is still possible to notice that case C, optimised with only static loads, fails when subjected to gust loads that were not included during the optimisation. This result again shows the importance of including dynamic loads early in the design phase.

Despite the limited impact of dynamic loads on the regional wing model sizing, it is generally recognised that both static and dynamic loads shall be taken into consideration since the early design phase (Kenway et al., 2014) to provide the optimiser with all the relevant load cases. This is even more critical for composite wing structures (Werter, 2017) that, due to the many design variables, can be tailored for the loads taken into consideration but results less robust than metal

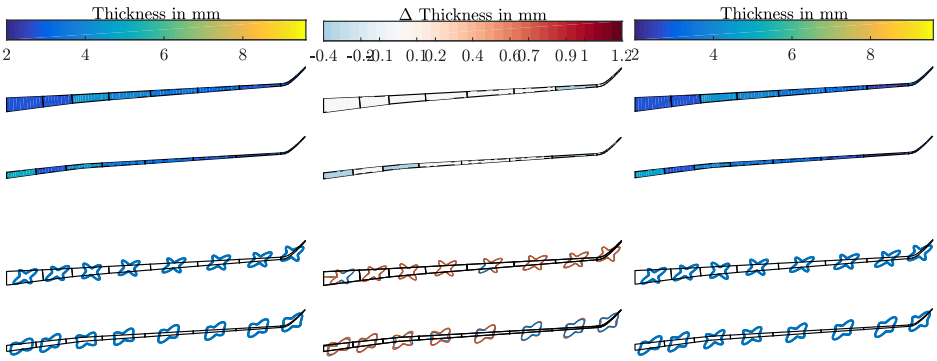


**(a)** Case C **(b)** Case C → Case D **(c)** Case D

**Figure 5.8:** Front and rear spar thickness and stiffness distributions for case C, case D and the difference between the two cases



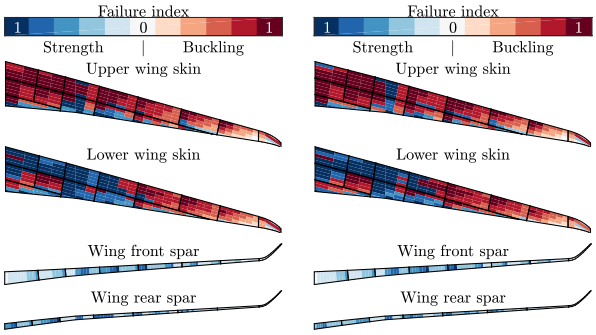


**(a)** Case C **(b)** Case D

**Figure 5.9:** Most critical failure index based on mechanical constraints at continuous optimum for cases C and D.

wing when subjected to a new set of loads not included during the wing structure optimisation. Therefore, given the importance of including dynamic loads, the reliability of the ESL to produce a feasible structure needs to be assessed. The ESL method relies on a weak coupling between the gust simulations and the optimizer. During the structural optimization process, gust loads are considered frozen and updated at fixed intervals. This means that the optimized design meets the frozen gust loads at each iteration, but there is no guarantee that the design will still be valid once the gust loads are recomputed. Hence, after the optimization process is complete, a final analysis is conducted. The optimized structure is tested through a dynamic aeroelastic analysis, in which the strength and buckling values are checked for possible failure.

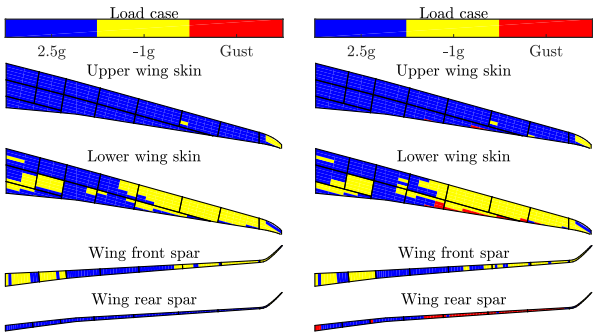


**(a)** Case D **(b)** Case D

**Figure 5.10:** Load-cases associated with the most active mechanical constraints at continuous optimum for cases C and D.

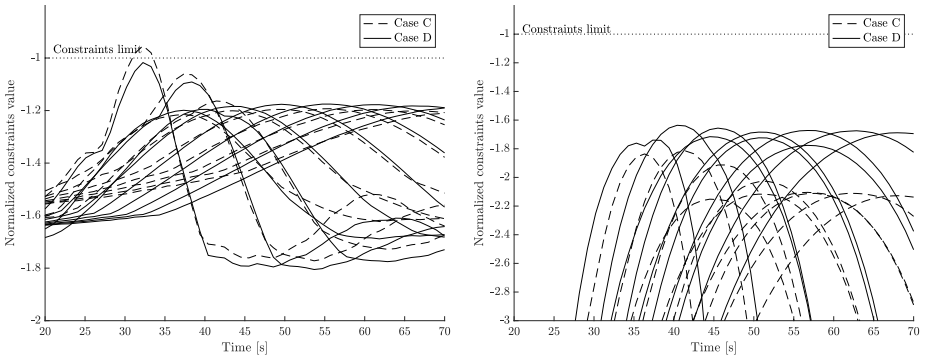


**(a)** Strength constraint **(b)** Buckling constraints

**Figure 5.11:** Time history of critical strength and buckling constraints during the ten different encountered gust for case C and case D

The results of this test are shown in Figure 5.12 where the time histories of the most critical strength and buckling constraints from gust load are compared for case D. The figure shows the constraints time histories from the last optimisation iteration and the gust check step. The results show that strength constraints do not change significantly between the last optimisation iteration and the gust check step, less than 0.7%. On the other hand, the change in buckling constraints is more pronounced and can reach up to 5%. This is due to the fact that while strength constraints depend only on external loads and membrane lamination parameters, buckling depends on external loads and both membrane (e.g. responsible for the internal fluxes) and bending lamination parameters as in Equation (4.1). Thus, buckling constraints are generally more affected by changes in design variables during the ESL loop. Therefore, if a gust load-cases is critical for wing sizing due

to buckling constraints, a different strategy should be implemented to ensure a small change in buckling constraint values between subsequent ESL steps. Such a strategy could imply the use of under-relaxation factors to control the evolution of the structure during the optimisation.

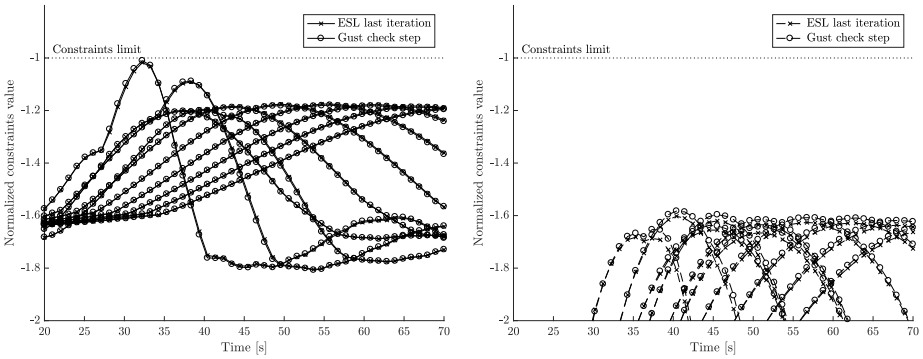


**(a)** Strength constraint **(b)** Buckling constraints

**Figure 5.12:** Time history of critical strength and buckling constraints during the ten different encountered gust for case D. Comparison between the ELS last load set and the gust check step.

In this section, only cases C and D have been compared. However, similar observations and conclusions can also be made when comparing cases A and B. For the sake of brevity, this second comparison is not presented here. The results from cases A and B and their difference can be found in Appendix B.

## 5.4 Effect of blending on stacking sequence retrieval

Once the continuous optimisation described in Section 4.2 converges to an optimal wing design, the stiffness matrix and thickness of each section of the wing are defined. However, in order to manufacture the wing, it is essential to retrieve the stacking sequence associated with the obtained optimal stiffness and thickness distribution. This is achieved with the stacking sequence retrieval process described in Section 4.3.

In this section, the optimal designs from all four cases are considered. The GA introduced in Section 4.3 is used to retrieve the stacking sequences that best match the continuous optimum designs by minimising the root means squared error between the optimum design and the discrete stacking sequence generated by the GA. Unlike more sophisticated GA (Irisarri et al., 2011; Vicente, 2019), the GA used in this dissertation does not have access to information such as mechanical constraints values or their derivative with respect to design variables,

so any of the results presented here could be further improved. During the GA run, manufacturing constraints have been imposed in order to retrieve only symmetric laminates with ply orientation limited to multiples of 15°.

The GA stacking sequence retrieval has been performed ten times for each design, and the averaged RMSE obtained after stacking sequence retrieval are shown in Figure 5.13 while the normalised weight difference is presented in Table 5.1. As seen in Section 5.2, the introduction of the blending constraints results in a weight increment of about 5%. However, this weight increment is also followed by a significant reduction of the RMSE between the target and the retrieved lamination parameters during the stacking sequence retrieval. This reduction of about 60% shows that the blending constraints help the continuous optimisation in converging to a continuous design that is much closer to the discrete solution and, therefore closer to a manufacturable solution.

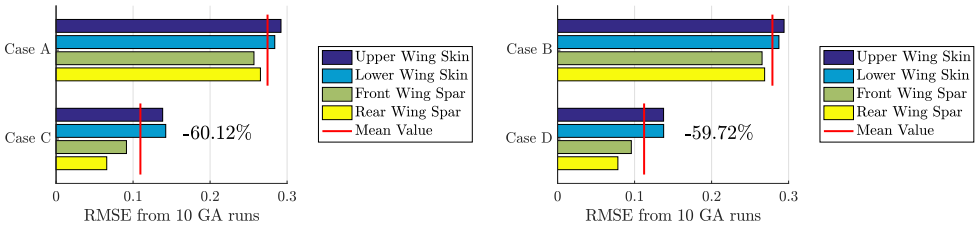


**(a)** Comparison cases A (w/o blending) and C (w/ blending).

**(b)** Comparison cases B (w/o blending) and D (w/ blending).

**Figure 5.13:** Stacking sequence retrieval RMSE for all cases.

If all constraints are met during the continuous optimization process, retrieving a discrete structure that does not exactly match the continuous stiffness and thickness distributions will likely result in a wing that fails to meet all mechanical constraints and global wing behaviour. The effect of this mismatch in the retrieval of discrete stacking sequence is visible in Figures 5.14 and 5.15 and Table 5.2.

**Table 5.2:** Improvements in constraints violation after stacking sequence retrieval due to the use of blending constraints.

| | **Failed Elements** | | **Mean Failure Index** | | **Max Failure Index** | |
|---|---|---|---|---|---|---|
| | Strength | Buckling | Strength | Buckling | Strength | Buckling |
| **Case A** | 312 | 99 | 1.22 | 1.43 | 2.42 | 2.56 |
| **Case C** | 144 | 50 | 1.10 | 1.21 | 1.38 | 1.80 |
| **Delta A-C** | -54% | -49% | -10% | -15% | -43% | -30% |
| **Case B** | 305 | 95 | 1.25 | 1.42 | 2.33 | 2.57 |
| **Case D** | 164 | 53 | 1.12 | 1.20 | 1.42 | 2.07 |
| **Delta B-D** | -46% | -44% | -10% | -15% | -39% | -19% |

Figures 5.14 and 5.15 present the values of the constraints for each element and

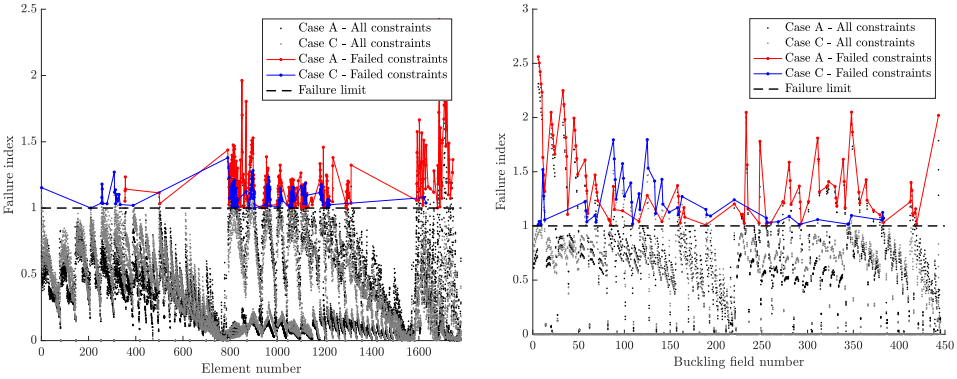


**(a)** Strenght constraints.

**(b)** Local buckling constrainrs

**Figure 5.14:** Strenght and buckling constraints values for the retrieved discrete structures of case A (w/o blending) and case C (w/ blending)



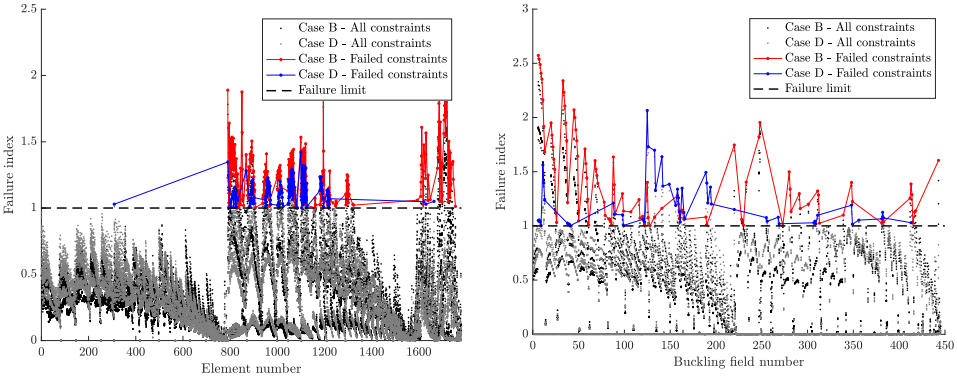


**(a)** Strenght constraints.

**(b)** Local buckling constrainrs

**Figure 5.15:** Strenght and buckling constraints values for the retrieved discrete structures of case B (w/o blending) and case D (w/ blending)

buckling zone of the wing for all the four cases considered in this chapter after the stacking sequence retrieval step. The total number of failed elements, together with the mean and max failure indices for both strength and local buckling constraints, are summarised in Table 5.2. For the number of failed elements, the reported number consists of the failed elements in all load-cases. This means that if the same element fails in two different load-cases, it is counted twice. The smaller RMSE between the target and retrieved lamination parameters resulting from the use of the blending constraints significantly reduces the number of failed

elements and the failure indices. In particular, failed elements are reduced by about $44\% - 54\%$, the mean failure indices are reduced by about $10\% - 15\%$, and the maximum failure indices are reduced by about $19\% - 43\%$. Finally, the retrieved stacking sequences of the upper and lower wing skins for case D are shown respectively in Figures 5.16 and 5.17.

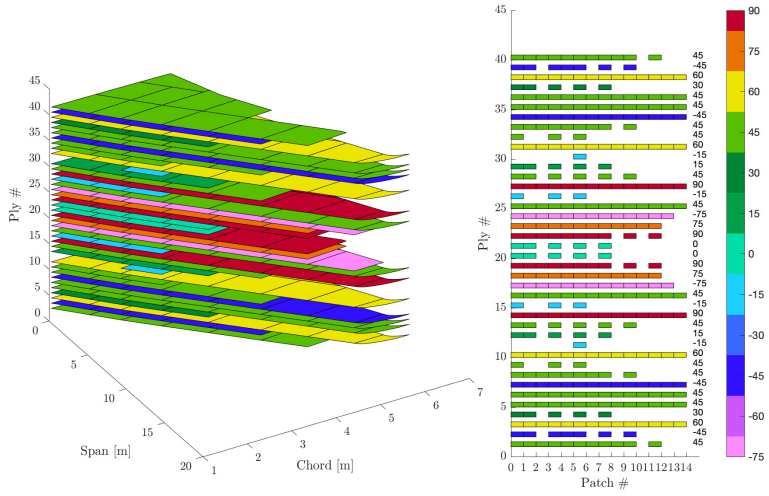


**Figure 5.16:** Retrieved stacking sequence for the upper wing skin - case D.

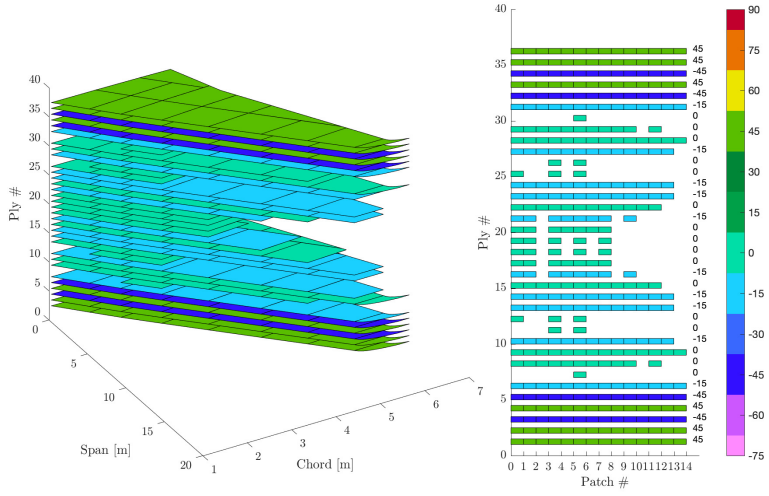


**Figure 5.17:** Retrieved stacking sequence for the lower wing skin - case D.

As seen in Figures 5.13, the proposed strategy and the GA tool used in this dissertation result in a continuous optimum that can be closely matched by a discrete

blended stacking sequence. However, as the match does not reach 100%, some of the mechanical constraints are no longer satisfied, see Figures 5.14 and 5.15. To have a measure of how much the retrieved discrete stacking sequences shall be corrected to satisfy both blending and all mechanical constraints, the following approach is used. First, the stiffness matrices corresponding to the retrieved stacking sequences are computed for all panels. Second, a weight minimisation optimisation is performed with a frozen stiffness matrix but variable thicknesses, allowing the optimiser to increase the thickness where it is needed without modifying the stacking sequence. This approach is by no means intended to retrieve the best-performing and ready-to-manufacture laminate. Still, it can provide a basis for comparing how much extra weight shall be added to satisfy all mechanical constraints. Results of this analysis are shown in Table 5.3 where the weights obtained by this process appear under the column $\overline{W}_{feasible}$. As it can be seen, while the use of blending constraints results in about 5% higher theoretical structural weight at the end of the continuous optimisation, the extra weight to be added to make the structure feasible is lower than in the case where no blending constraints have been used, resulting in a $1.5\% - 3.7\%$ lighter final design. These results justify the need for considering blending early in the design phase.



**Table 5.3:** Weight for different optimisation problems.

| Case | Static | Dynamic | Blending | $\overline{W}_{NRU}$[%] | $\overline{W}$[%] | $\overline{W}_{feasible}$[%] |
|---|---|---|---|---|---|---|
| A | Yes | No | No | 100.00 | 102.16 | 115.42 |
| B | Yes | Yes | No | 100.05 | 102.16 | 117.59 |
| C | Yes | No | Yes | 105.01 | 107.50 | 113.72 |
| D | Yes | Yes | Yes | 105.14 | 108.04 | 113.36 |

A different and more sophisticated GA has been used by Vicente (2019) to retrieve a discrete stacking sequence using the same ONERA regional wing model and cases similar to the cases B and D used in this dissertation. The GA used in the above-mentioned study, called *pyTLO*[1], is capable of using mechanical constraint values and sensitivities to take into account constraints violation during stacking sequence retrieval. Besides, the GA allows for the addition or removal of plies where it sees fit. *PyTLO* was able to retrieve a fully feasible and blended discrete structure with a weight increment of 5% if blending were used in the continuous optimisation and a fully feasible and blended discrete structure with a weight increment of 35% if blending constraints were not used in the continuous optimisation showing the capability of the blending constraints in retrieving a more ready-to-manufacture continuous design.

[1] `https://gitlab.com/FGS_SSR/pytlo`

# 6

# EFFECT OF HIGH-FIDELITY AERODYNAMIC DRAG ON AEROELASTIC TAILORING

This chapter applies the optimisation strategy presented in Chapter 4 to the ONERA regional wing model introduced in Section 4.1. This second application adds the surrogate model described in Chapter 3 and aims at performing a trade-off study of conflicting objectives: structural weight minimisation and aerodynamic drag minimisation.

Section 6.1 focuses on the creation of the surrogate model based on the model reduction introduced in Chapter 3. This includes the retrieval of the constant projection matrix, the truncation during SVD and PCA and the surrogate model selection. Section 6.2 applies the surrogate model to two studies: Section 6.2.2 focuses on the effect of the aerodynamic constraint on the wing optimisation, while Section 6.2.3 focuses on the validation of the results with respect to CFD.

## 6.1 MODEL REDUCTION AND SURROGATE MODEL CREATION

This section applies the approximation of the wing structural displacement and the subsequent surrogate model selection and assessment as described in Chapter 3. In particular, Section 6.1.1 covers the approximation of the wing structural displacement presented in Section 3.1.1, while Section 6.1.2 covers the surrogate model selection from Section 3.1.2.

### 6.1.1 PROJECTION MATRIX VIA SINGULAR VALUE DECOMPOSITION AND TRUNCATION

As described in Section 3.1.1, to reduce the dimensionality of the surrogate model, the wing structural displacements are projected onto a constant projection basis. This means that the projection basis is independent of the design variables used during the optimisation. To retrieve such basis, the proposed approach consists of performing a DOE of the structural design variables and extract natural modes and aeroelastic displacements under $1g$ cruise condition as shown in Figure 3.1. For this DOE, a total of 400 different wing structures are generated, and for each structure, the first 50 modes are computed. The results are split into a training and test set with an 80/20 ratio as suggested in Hastie et al. (2017).

A singular value decomposition is then applied to $\mathbf{\Phi}$, the set of natural modes from all structures, to determine $\mathbf{L}$ the smallest set of orthonormal vectors required to describe the column space of $\mathbf{\Phi}$. Finally, a truncation over the number of columns of $\mathbf{L}$ is performed to obtain the projection basis $\tilde{\mathbf{L}}$. The decision on how many column vectors to retain is based on the displacement residual $\mathbf{u}_{res}$.

Figure 6.1a shows the mean and maximum values of the Euclidian norm of the residual displacement $\mathbf{u}_{res} = \mathbf{u}_E - \tilde{\mathbf{u}}_E$ for the training and test sets. Figure 6.1b shows the mean and maximum values of the maximum absolute residual displacement. From Figure 6.1b, it is possible to notice that with 100 modes, the mean values of all the maximum absolute difference between $\mathbf{u}_E$ and $\tilde{\mathbf{u}}_E$ is about 1 mm, approximately 0.006% of the wingspan. Moreover, it is possible to see that the truncated orthogonal projection basis $\tilde{\mathbf{L}}$ results in the same projection quality for both the training and the test set, meaning that it guarantees an adequate projection basis for the whole design space. Therefore, for this application, the first 100 columns of the matrix $\mathbf{L}$ will be used as a projection basis and will compose the matrix $\tilde{\mathbf{L}}$, this means that $n_L = 100$ in Equation (3.5). Further reduction is presented in Section 3.1.2 as an input of 100 generalized coordinates is too big to build a robust surrogate model.

Appendix C shows the first nine structural modes from $\mathbf{\Phi}$ and the first nine modes

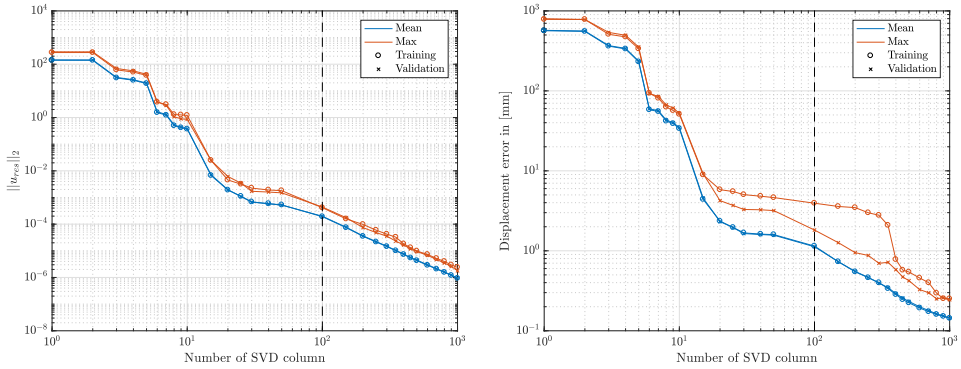


**(a)** Variation of the Euclidian norm of the residual displacement as a function of the number of SVD columns.

**(b)** Variation of the displacement error as a function of the number of SVD columns.

**Figure 6.1:** Effect of the truncation after SVD on the Euclidean norm of the residual displacement and the displacement error. The vertical dashed line represents the truncation at $n_L = 100$.

obtained after the transformation in $\tilde{\mathbf{L}}$ by SVD, ordered by decremental singular value.

### 6.1.2 Generalized coordinate reduction via principal component analysis

As described in Section 3.1.2, to further reduce the surrogate model dimensionality, all inputs should be non-correlated. To achieve that and eliminate the potential correlation between the generalised coordinates ($\boldsymbol{p}$) obtained by projecting structural displacement on the projection matrix $\tilde{\mathbf{L}}$, see Equation (3.6), a principal component analysis is performed on the generalised coordinates.

Figure 6.2a shows the correlation between the first 50 generalized coordinates ($\boldsymbol{p}$) obtained when using $\tilde{\mathbf{L}}$ as projection basis. The 'chessboard' distribution of high positive and high negative correlation, especially among the first 15 generalised coordinates, shows the presence of highly correlated data. Figure 6.2b shows the correlation between the new set of coordinates ($\boldsymbol{\nu}$) obtained from the PCA. It is possible to see that all the new coordinates are non-correlated and, therefore, they are better suited to be used in creating the surrogate model.

While the truncation of $\tilde{\boldsymbol{L}}$ has shown, see Figure 6.1b, that 100 column vectors provide adequate residual error for the whole design space, the reduction on principal components number needs to be more extensive in order to result in fewer required generalized coordinates. Ideally, ($\boldsymbol{\nu}$) should be as small as possible

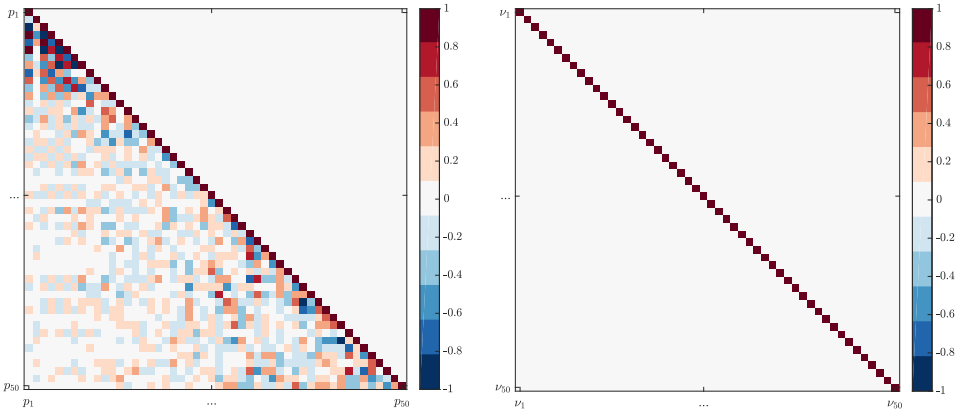


**(a)** Correlation matrix among the generalized coordinated ($\boldsymbol{p}$) obtained when projecting structural displacement over $\tilde{\mathbf{L}}$.

**(b)** Correlation matrix among the principal coordinated ($\boldsymbol{\nu}$) obtained after performing a PCA.

**Figure 6.2:** Correlation matrices of the generalized coordinates ($\boldsymbol{p}$) and the principal coordiantes ($\boldsymbol{\nu}$).



without compromising too much model accuracy.

The effect of reduction in principal components can be seen in Figures 6.4a and 6.4b. As expected, for a number of principal components ($\boldsymbol{\nu}$) that tends to 100, the values of Euclidean norm of the residual displacement and maximum absolute error reach the same values obtained in Figures 6.1a and 6.1b as the model reaches the same dimensionality as the starting model after SVD. If fewer principal components are considered, there is an increase in both the Euclidean norm and the maximum absolute value of the residual displacement. One way to decide where to truncate after PCA transformation is to investigate the variance ratio and its cumulated value in Figure 6.3. Unless there is a sudden drop in the variance ratio, there is no general agreement on what the proper threshold level is.

In this work, it has been decided to truncate the number of principal components to the first 13 ($n_\Psi = 13$). This truncation level of the new generalized coordinates results in a mean of all maximum absolute errors of less than 2.5 mm, see Figure 6.4b, approximately 0.015% of the wingspan. With $n_\Psi$ selected, Equation (3.9) can be used to compute $\tilde{\boldsymbol{\Psi}}$ and $\mathbf{p}_{mean}$. Figures 6.5 and 6.6 show the absolute displacement and twist error between the real displacement and the approximated one for different values on truncation level at different wingspan positions (i.e. 50%, 80%, 100%, winglet tip). The results for the truncation at $n_\Psi = 13$ are summarized in Table 6.1.

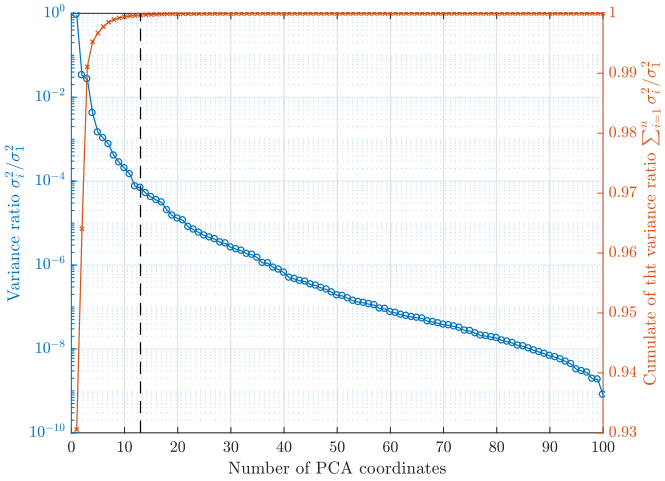


**Figure 6.3:** Variance ratio associated with each principal component and its cumulated value.

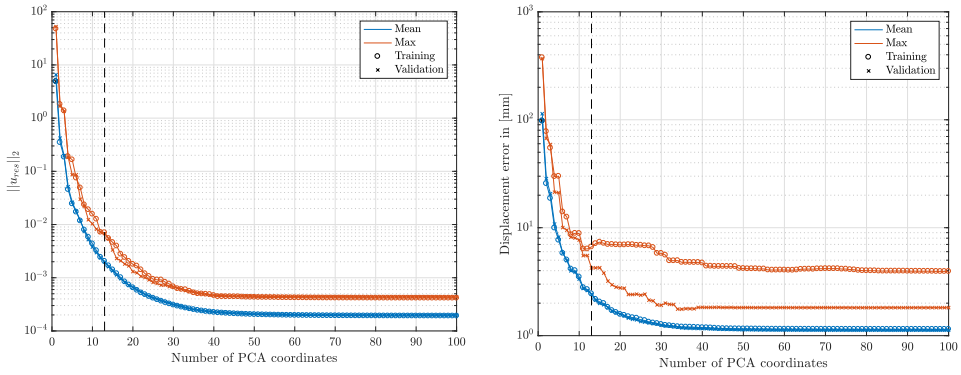


**(a)** Euclidian norm of the residual displacement

**(b)** Maximum absolute value of the residual displacement

**Figure 6.4:** Effect of the truncation after PCA on the Euclidean norm of the residual displacement and on the displacement error

Appendix C shows the first nine modes from the final PCA-modes.

**Table 6.1:** Mean values of the maximum structural deformation approximation error for both displacement and twist.

| Span-wise position | Displacement error [mm] | Twist error[deg] |
|---|---|---|
| 50% | 0.445 | 0.0166 |
| 80% | 0.342 | 0.0162 |
| 100% | 0.506 | 0.0856 |
| Winglet tip | 0.852 | 0.0978 |

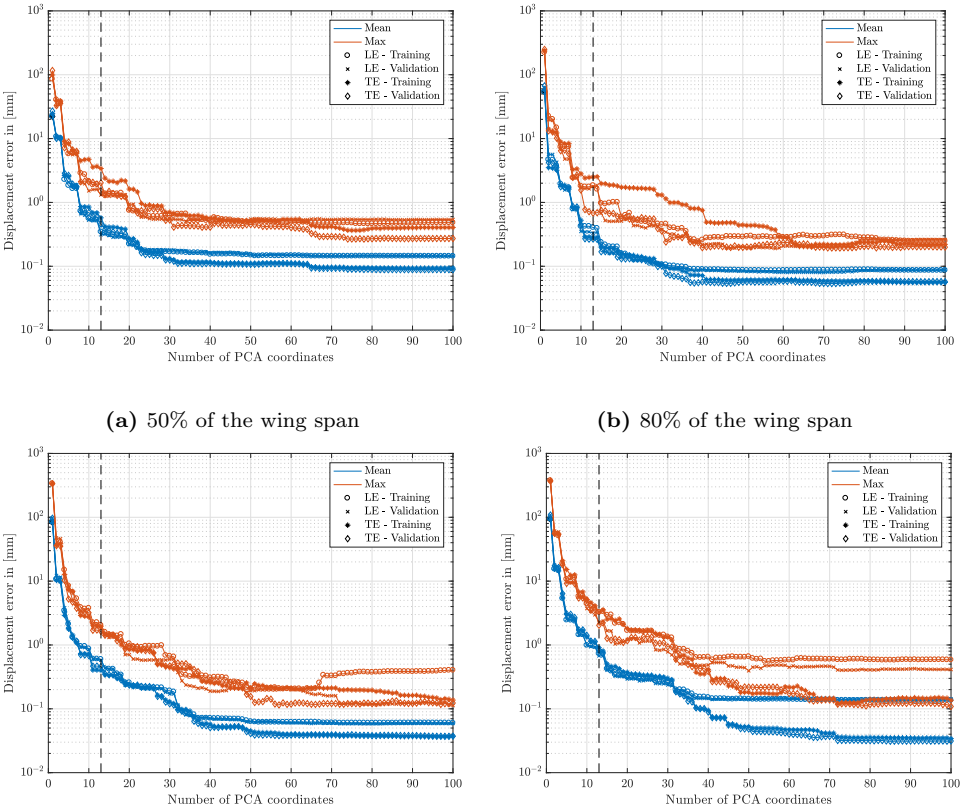


**(a)** 50% of the wing span

**(b)** 80% of the wing span

**(c)** 100% of the wing span

**(d)** Winglet tip

**Figure 6.5:** Absolute error in displacement at different spanwise wing locations.



### 6.1.3 DESIGN OF EXPERIMENT AND MESH DEFORMATION

Once all quantities involved in the approximation of the structural displacements are defined, it is possible to use this approximation in a Design of Experiment and generate all structural deflections needed to create the surrogate model for aerodynamic drag.

As per Equation (3.12), the design space for the surrogate model is composed of the 13 principal components ($\nu_i$) plus the angle of attack ($\alpha$), while $\tilde{\mathbf{L}}$, $\tilde{\mathbf{\Psi}}$, $\mathbf{p}_{mean}$ have been obtained in Sections 6.1.1 and 6.1.2 and stored. The 400 randomly generated structures used in Section 6.1.1 to retrieve the constant projection matrix and the principal components are here used to estimate a realistic range of the principal coordinate to be used in the DOE. The obtained range is then doubled

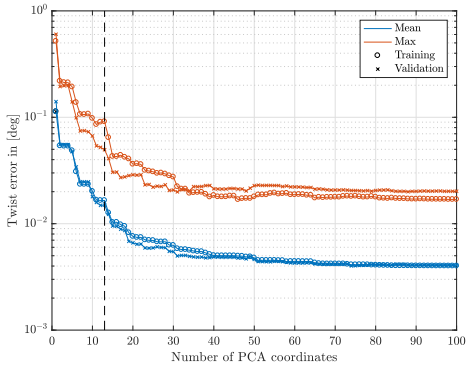


**(a)** 50% of the wing span

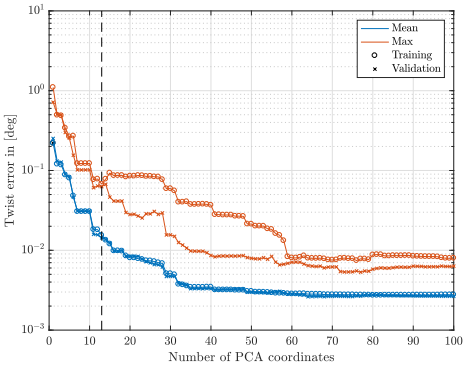


**(b)** 80% of the wing span

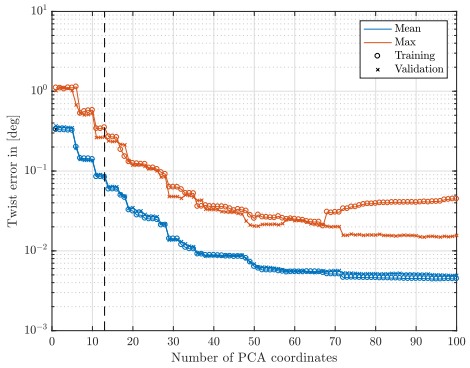


**(c)** 100% of the wing span

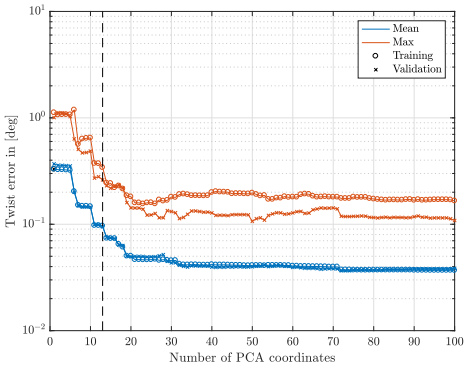


**(d)** Winglet tip

**Figure 6.6:** Absolute error in local wing twist at different spanwise wing location

to take into account a wider range of displacements. To evenly sample the design space, the Halton sequence is used (Halton, 1960). This sequence is deterministic, but thanks to its low discrepancy property, it can sample the design space uniformly. A total of 1000 points has been used in the DOE.

From each point of the DOE, the angle of attack is directly inserted as a parameter inside the CFD solver *elsA* (Cambier et al., 2011) and the generalized coordinates are used to compute the corresponding elastic displacement ($\mathbf{u}_E$) using Equation (3.11). The retrieved structural displacements are then splined, by means of Thin Plate Spline (TPS) (Duchon, 1977), onto the aerodynamic wetted surface using the python tool *Cassiopee* (Benoit et al., 2015). Then, the aerodynamic mesh is deformed accordingly by using *elsA*. For each point of the DOE, a rigid RANS computation is run with the Spalart-Allmaras turbulence model, and the

resulting drag coefficient is stored for surrogate model selection and assessment.

### 6.1.4 MODEL SELECTION, VALIDATION AND PERFORMANCE

The surrogate model selection is based on the results of the K-fold cross-validation described in Section 3.2.2 over a grid search that runs over a manually specified subset of the hyperparameter space. Therefore, each model is evaluated via the K-fold cross-validation, and the hyperparameters associated with the best RMSE and regression error characteristics (REC) (Bi and Bennett, 2003) performance are extracted.

The REC curve is defined as a cumulative distribution of the model error. It presents on the x-axis the error and on the y-axis the percentage of data points that are fit within the error. This curve allows to compare the range of errors between different models and complements the information provided by the RMSE. The ideal surrogate model should have 100% of the predicted outcome at 0% error tolerance. This means having a REC composed only by a horizontal line at the ordinate value 100%. The area under the REC curve is used to compare the REC performance between models, and in this dissertation, the area is computed only between the RMSE of 0 and 10 drag counts.



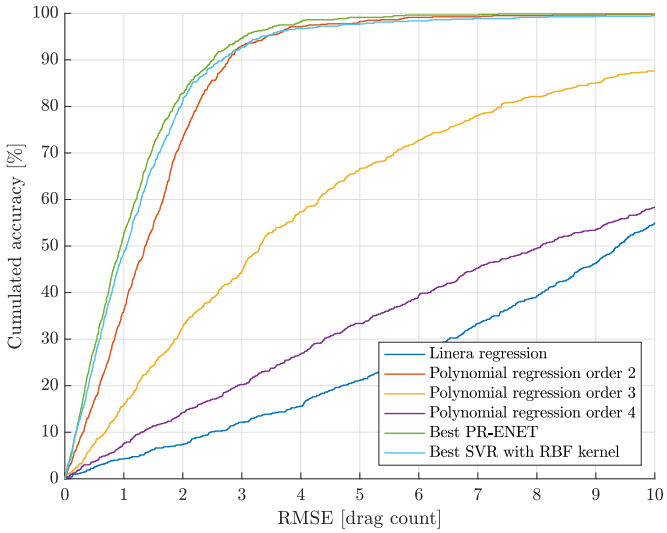


**Figure 6.7:** REC curves for the different models.

Figure 6.7 shows the REC curves for the best models considered in this dissertation, while Figure 6.8 compares the RMSE and the REC area from all models. As shown in Figure 6.7, the best polynomial regression with elastic net regularisation

(PR-ENET) model performs better than all other models. This model resulted in 52.6% of the data points having an RMSE of less than 1 drag count (d.c.) and 82.8% of the data points having an RMSE of less than 2 d.c. From Figure 6.8, it is possible to see that the best PR-ENET model performs better than the other models also in terms of mean errors, having an RMSE of approximately 1.55 d.c. The grey markers identify the performance of all the models tested with different hyperparameters. The hyperparameters of the best performing models are shown in Table 6.2 together with their RMSE and REC area.

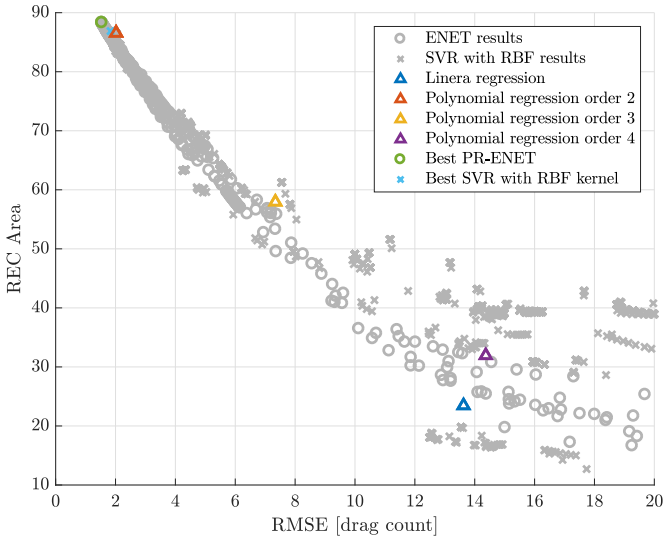


**Figure 6.8:** Comparison RMSE and REC area for the different models.

**Table 6.2:** Best performing hyperparameters for the different models and their RMSE and REC areas.

| Surrogate Model | Hyperparameter | | Cross validation | |
|---|---|---|---|---|
| | Name | Value | RMSE | REC area |
| Linear Regression | - | - | 13.63 | 23.45 |
| Polynomial Regression | k | 2 | 2.03 | 86.56 |
| Polynomial Regression with ENET | k | 3 | 1.55 | 88.31 |
| | $\alpha$ | 1.0 | | |
| | $\lambda$ | $5.46E-4$ | | |
| SVR with RBF kernel | $\gamma$ | $1.7E-3$ | 1.83 | 86.88 |
| | $\epsilon$ | $1.3E-2$ | | |
| | C | $3.5E+3$ | | |

Given the results summarized in Table 6.2, the polynomial regression with ENET is the model used to approximate aerodynamic drag. To validate the model and

estimate its performance against unseen data, the model is tested once again with the test set and predicted drag coefficients have an RMSE of 1.29 d.c. The comparison between the test set and predicted outputs are shown in Figure 6.9. The selected surrogate model, together with its hyperparameters, cross-validation RMSE and REC and generalisation error, is shown in Table 6.3

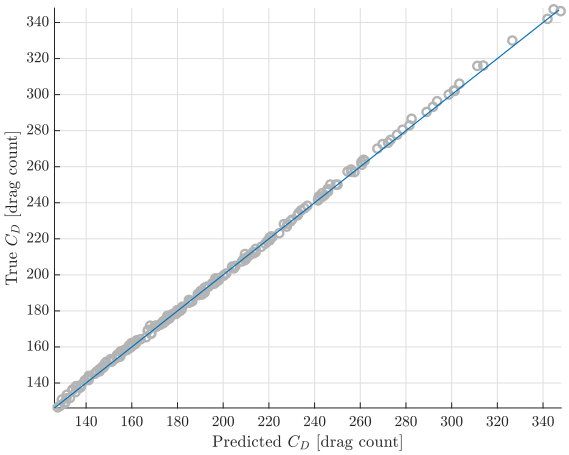


**Figure 6.9:** Comparison between predicted output and true output from the test set.



**Table 6.3:** Surrogate model used to approximate aerodynamic drag with hyperparameter values, K-fold cross-validation performance and generalisation error.

| Surrogate Model | Hyperparameter | | Cross validation | | Generalisation |
|---|---|---|---|---|---|
| | Name | Value | RMSE | REC area | RMSE |
| Polynomial Regression with ENET | k | 3 | 1.55 | 88.31 | 1.29 |
| | $\alpha$ | 1.0 | | | |
| | $\lambda$ | 5.46E-4 | | | |

## 6.2 MULTI-OBJECTIVE OPTIMISATION OF A REGIONAL AIRCRAFT WING

This section presents the results of the multi-objective optimisation of the ONERA regional wing model. Both structural weight and aerodynamic drag are considered during the optimisation. The multi-objective optimisation is translated into a constrained Pareto optimisation, as further explained in Section 6.2.1, to show the effect the aerodynamic drag constraint has on structural sizing. Different optimised structures are compared, and a final validation is performed to check if the aerodynamic drag computed by the surrogate models agrees with the full-order CFD analysis.

### 6.2.1 Optimisation strategy to obtain Pareto front

The optimisation strategy used in this section is presented in Section 4.2 together with the ONERA regional wing model and all the constraints considered during the optimisation. Chapter 5 presents the first application of such optimisation. However, by integrating the surrogate model for aerodynamic drag, see Section 4.2.7, it is now possible to perform a multi-objective optimisation.

The approach used in this dissertation to perform multi-objective optimisation is the $\epsilon$-constraint method (Haimes et al., 1971). While the weighted sum method (Zadeh, 1963) combines the different objectives into a single function through weighting parameters, the $\epsilon$-constraint method turns a multi-objective optimisation into single-objective optimisation by incorporating all but one objective as constraints. A parametric variation of the constrained objective function ($f_2 \leq \epsilon_i$) is then performed to obtain a Pareto front, see Figure 6.10. Examples of a bi-objectives optimisation written with the weighted sum and with the $\epsilon$-constraint method are presented in Equations (6.1) and (6.2), were $\mathbf{x} \in S$ represents the constraints applied to the design variable $\mathbf{x}$.

$$\boxed{\text{Weighted sum method}}$$

$$\begin{aligned} \text{Minimize} \quad & I(\mathbf{x}) = w_1 f_1(\mathbf{x}) + w_2 f_2(\mathbf{x}) \\ \text{subject to} \quad & \mathbf{x} \in S \end{aligned} \tag{6.1}$$

$$\Big\downarrow \text{ is transformed into}$$

$$\boxed{\epsilon\text{-constraint method}}$$

$$\begin{aligned} \text{Minimize} \quad & f_1(\mathbf{x}) \\ \text{subject to} \quad & f_2(\mathbf{x}) \leq \epsilon_i \\ & \mathbf{x} \in S \end{aligned} \tag{6.2}$$

In the weight sum method, the scaling of the objective functions directly impacts the results, and thus, the weights need to be carefully selected to obtain a Pareto-optimal solution in a desired region of the objective space or to avoid solutions being dominated by a single objective. The $\epsilon$-constraint method does not have such a problem, and setting one of the objectives as a constraint requires little additional effort and gives direct control over the region of the Pareto front to investigate. Another advantage of the $\epsilon$-constraint is its applicability to either convex or non-convex problems. However, the range of objective functions needs to be known a priori in order to properly constrain one of the functions.

In this dissertation, the $\epsilon$-constraint method is implemented with the weight minimisation as the objective function and with the drag coefficient minimisation as

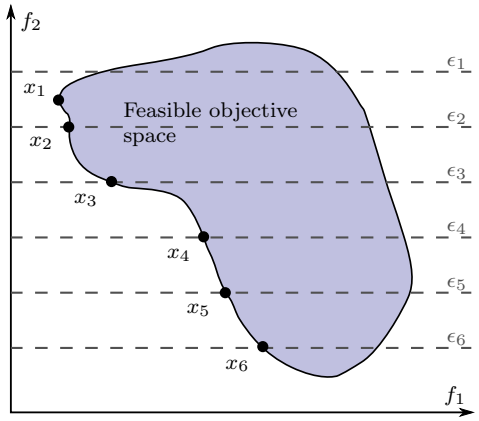


**Figure 6.10:** Representation of the $\epsilon$-constraint method.

the constraint objective as shown in Equations (6.3).

$$\begin{aligned} \text{Minimize} \quad & W(\mathbf{x}) \\ \text{subject to} \quad & C_D(\mathbf{x}) \leq \epsilon_i \\ & \mathbf{x} \in S \end{aligned} \tag{6.3}$$



### 6.2.2 RESULTS OF THE OPTIMISATION

This study examines two different wing designs, as detailed in Table 6.4. The first design, referred to as the unblended wing, has been optimized to account for both static and dynamic loads, all the constraints outlined in Section 4.2, with the exception of the blending constraints. The second design, referred to as the blended wing, includes the blending constraints.

**Table 6.4:** Characteristics of for different optimisation cases.

| Case | Static | Dynamic | Drag | Blending |
|---|---|---|---|---|
| Unblended | Yes | Yes | Yes | No |
| Blended | Yes | Yes | Yes | Yes |

Figure 6.11 shows the Pareto fronts resulting from the bi-objective optimisations performed on the unblended and blended wings. As the figure shows, the two objectives considered during the optimisation (i.e. weight minimisation and drag coefficient minimisation) are conflicting objectives, as the reduction of one results in the increment of the other. As also shown in Section 5.2, the introduction of the blending constraints resulted in a weight increment between 3.8% and 5.9%,

in line with the results from Chapter 5; however, there is no significant impact on the trend of the Pareto front.

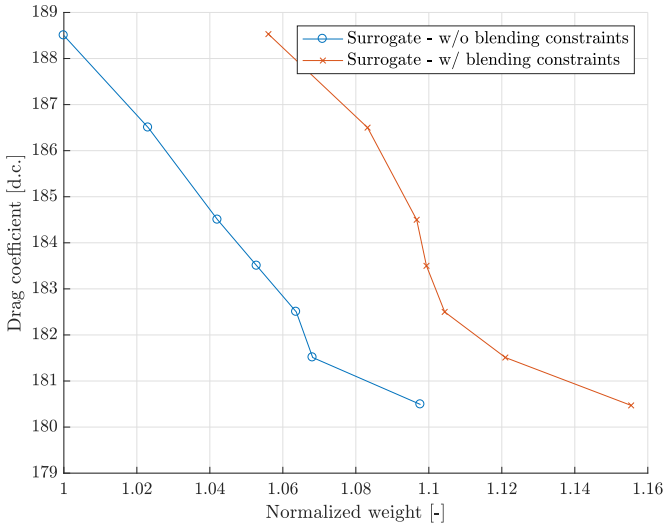


**Figure 6.11:** Pareto fronts obtained from the bi-objective optimisation.



For the sake of clarity, from here until the end of the section, only the results of the blended wing optimisation are presented. The results from the unblended wing can be found in Appendix D.

Figures 6.12 to 6.15 show the evolution of the thickness and stiffness distribution for different drag coefficient constraints, from $C_D = 188.5$ d.c. to $C_D = 180.5$ d.c., these values are the two end points of the graph in Figure 6.11.

From Figure 6.12, it is possible to see that for low structural weight and high drag coefficient, the optimiser favours structures with higher thickness towards the leading edge and with upper wing skin stiffness direction oriented towards the leading edge. These design choices favour a wing wash-out behaviour that results in lower lift distribution at the wingtip, reducing wing root bending moment and thus lowering structural weight. To compensate for the reduction of lift at the wingtip, the aircraft needs to fly at a higher angle of attack such that the lift equals the weight of the aircraft. This situation increases the aircraft's drag and reduces its cruise performance. For a more stringent constraint on the drag coefficient, see Figures 6.15, the optimiser favours structure with chordwise thickness more evenly distributed and with upper wing skin stiffness distribution aligned with the main wing axis. This results in a stiffer wing in bending with less wash-out behaviour that results in higher wing loading and, thus structural weight but allows the aircraft to fly at a lower angle of attack.

Figure 6.16 presents the vertical displacement and twist angle of the wing for

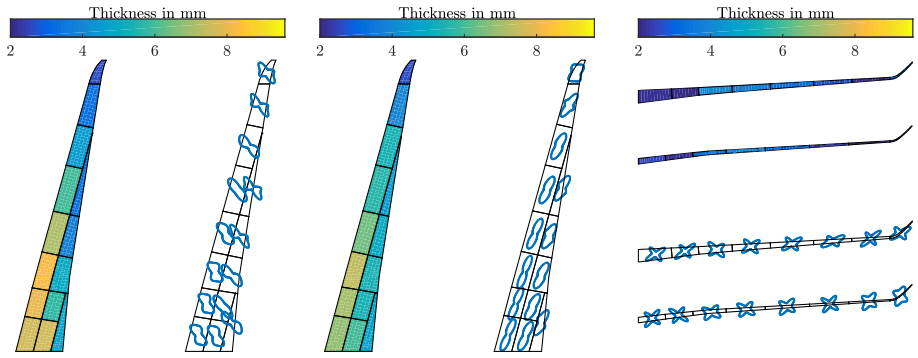


**(a)** Upper wing skin **(b)** Lower wing skin **(c)** Wing front and rear spars

**Figure 6.12:** Wing thickness and stiffness distributions for blended continuous optimum with $C_D \leq 188.5$ d.c.

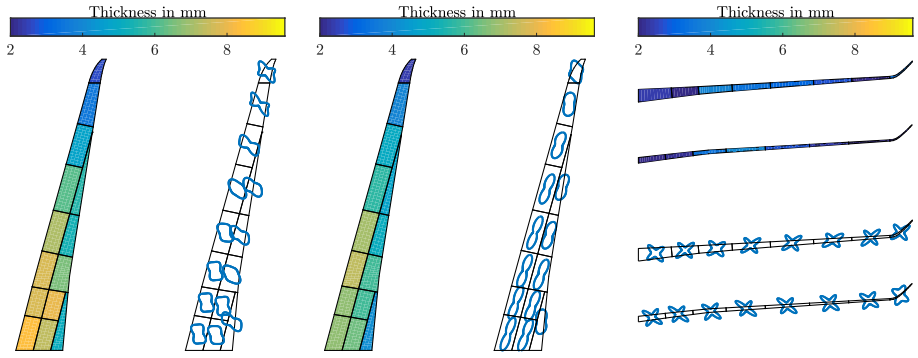


**(a)** Upper wing skin **(b)** Lower wing skin **(c)** Wing front and rear spars

**Figure 6.13:** Wing thickness and stiffness distributions for blended continuous optimum with $C_D \leq 184.5$ d.c.

various blended structures along the Pareto front. The twist angle measurement is relative to the freestream direction, rather than the aircraft's longitudinal axis, thereby reflecting the different angles of attack required to trim the different wings. This figure illustrates that the optimal solution for weight reduction results in a more flexible wing with greater wash-out angles compared to the solution focused on minimizing $C_D$, which leads to a stiffer wing. Additionally, the angles of attack under trim conditions for these solutions are depicted in Figure 6.17. Here, it is shown that lower angles of attack are associated with heavier weights but reduced drag coefficients.

The most active mechanical constraints and their associated load cases are presen-

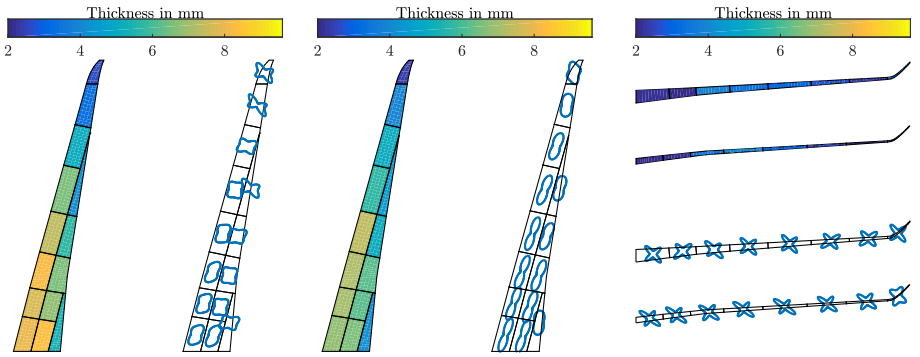


**(a)** Upper wing skin **(b)** Lower wing skin **(c)** Wing front and rear spars

**Figure 6.14:** Wing thickness and stiffness distributions for blended continuous optimum with $C_D \leq 182.5$ d.c.

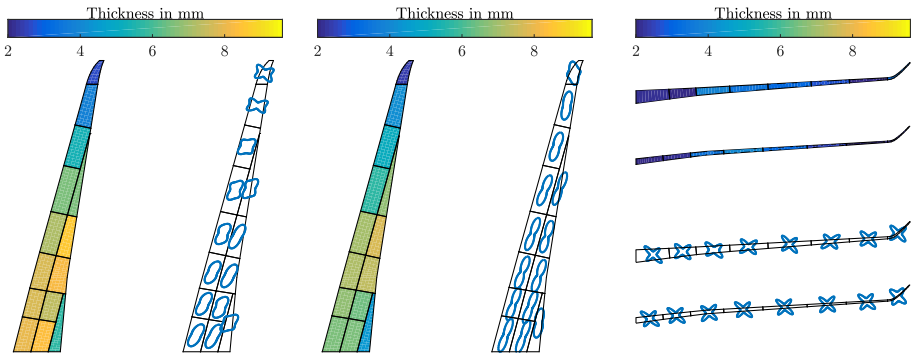


**(a)** Upper wing skin **(b)** Lower wing skin **(c)** Wing front and rear spars

**Figure 6.15:** Wing thickness and stiffness distributions for blended continuous optimum with $C_D \leq 180.5$ d.c.

ted in Figures 6.18 and 6.19, respectively, and it can be observed that, while the wing is mainly sized by buckling, the load cases associated with gust become one of the predominant sizing cases with the tightening of the aerodynamic drag constraints and the reduction in wash-out behaviour of the wing.

### 6.2.3 Validation with CFD

Validation of the results is performed by comparing the Pareto front, shown in Figure 6.11 which was constructed with the surrogate model, to full-order model CFD results. To do so, the wing structural displacement at cruise condition is extracted from the optimum solution and splined onto the aerodynamic mesh.

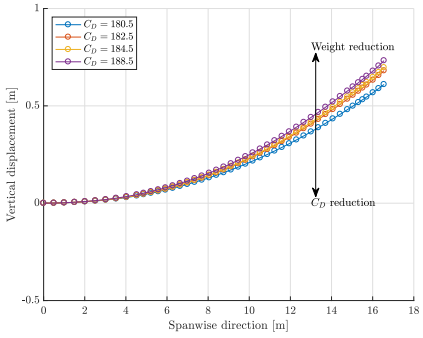


**(a)** Wing vertical displacement

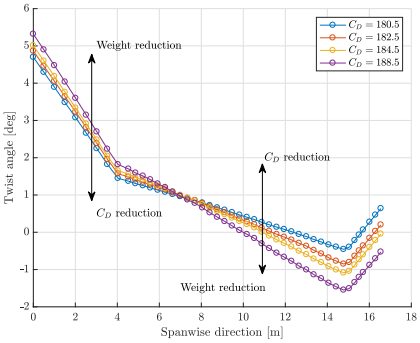


**(b)** Wing twist angle with respect to airstream

**Figure 6.16:** Comparison between different blended structures obtained with different constraints on $C_D$

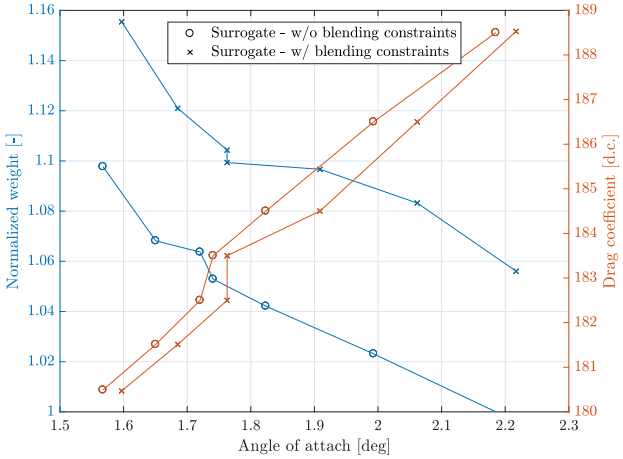


**Figure 6.17:** Trim angles for different results optimum on the Pareto from and the corresponding weight and drag coefficient.

This aerodynamic mesh is then deformed accordingly, and finally, *elsA* is used to run a rigid RANS computation on the deformed mesh with the Spalart-Allmaras turbulence model. Comparison between the results obtained with the surrogate model and with CFD are shown in Figure 6.20 while Figure 6.21 shows the relative and absolute errors. The absolute error varies between 0.9 and 1.6 d.c. which is well in line with the estimated surrogate model generalisation RMSE of 1.29 d.c. presented in Table 6.3. The surrogate model constantly overestimates the drag coefficient for all the points on the Pareto fronts; however, the two lines have the same trend.

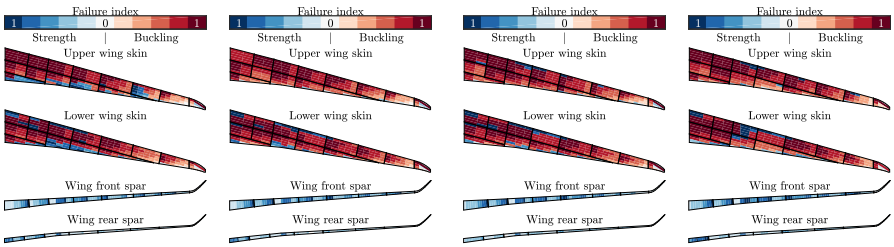


**(a)** $C_D \leq 188.5$ d.c. **(b)** $C_D \leq 184.5$ d.c. **(c)** $C_D \leq 182.5$ d.c. **(d)** $C_D \leq 180.5$ d.c.

**Figure 6.18:** Comparison between the most active mechanical constraints for different blended structures obtained with different constraints on $C_D$

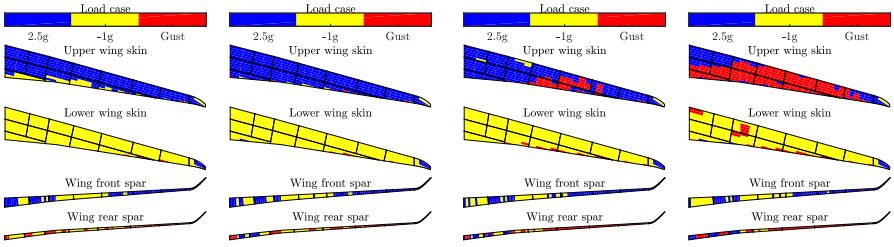


**(a)** $C_D \leq 188.5$ d.c. **(b)** $C_D \leq 184.5$ d.c. **(c)** $C_D \leq 182.5$ d.c. **(d)** $C_D \leq 180.5$ d.c.

**Figure 6.19:** Comparison between the load cases associated with the most active mechanical constraints for different blended structures obtained with different constraints on $C_D$

The wing normalised lift distribution and the normalised cumulative lift distribution are presented in Figure 6.22 and show, for low wing structural weight and high drag, how the lift distribution is shifted inboard compared to cases with low drag. Moreover, the lower weight is visible by comparing the cumulated lift at the wing root. These two effects are the result of wing wash-out behaviour. It should be noted here that the normalised cumulated lift curves at the wing root do match the trend shown in Figure 6.20 but not the correct weight ratios. The reason is that Figure 6.20 only consider the structural masses affected by the optimisation process while lift in Figure 6.22b also includes non-structural masses such as fuel, payload and other concentrated masses and structural masses non affected by the optimisation (e.g. the wing spars).

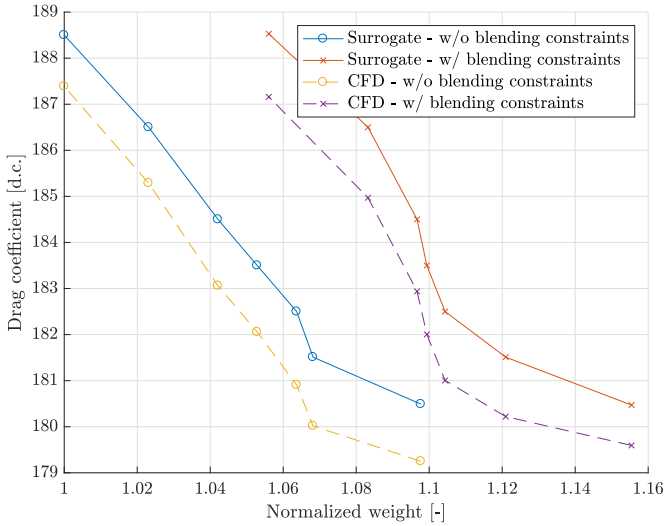


**Figure 6.20:** Comparison between the Pareto front obtained with the surrogate model and the drag coefficient obtained via CFD.



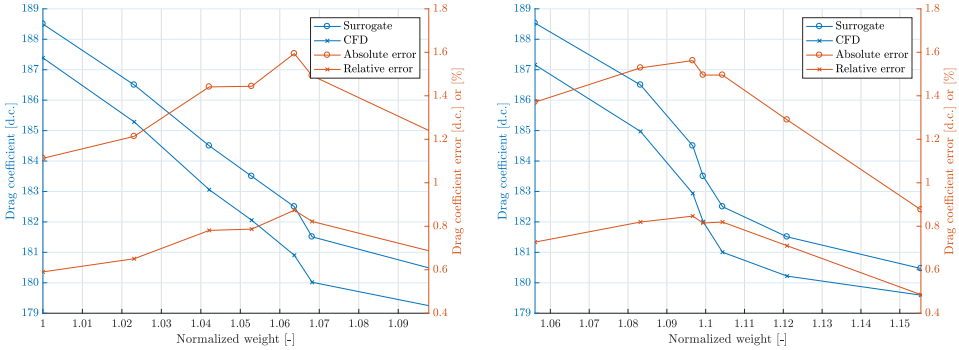


**(a)** Structure optimised without blending constraints

**(b)** Structure optimised with blending constraints

**Figure 6.21:** Absolute and relative error between surrogate model and CFD results.

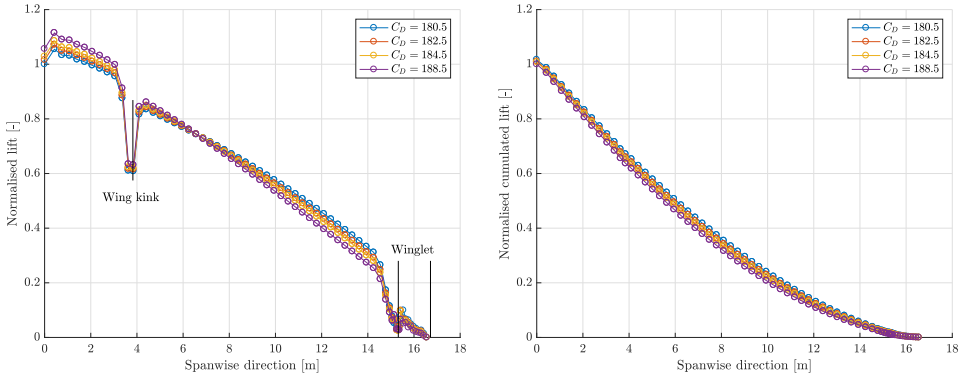


**(a)** Normalised spanwise lift distribution.

**(b)** Normalised spanwise cumulative lift distribution.

**Figure 6.22:** Spanwise lift distribution and its cumulate for different results optimum on the Pareto from and the corresponding weight and drag coefficient.

# 7

# Conclusions and Recommendations

As outlined in Chapter 1, aeroelastic tailoring has the potential to increase aircraft fuel efficiency by both reducing structural weight and improving aerodynamic drag by using the directional stiffness properties of composite materials. To get the most out of composite materials, variable stiffness composite structures are used where the material distribution and/or stacking sequence are allowed to vary over the structural domain. To ensure a smooth and gradual variation between the different regions of the structural domain, blending needs to be enforced at all levels of the optimisation process to ensure both structural continuity and an almost ready-to-manufacture results.

The objective of this dissertation is to:

*develop a preliminary wing design framework to perform aeroelastic tailoring, considering both structural weight and high fidelity aerodynamic drag while enforcing composite blending.*

The main objective of this dissertation is reached in two steps. In the first step, an aeroelastic tailoring framework that includes both static and dynamic loads is set up in the commercial tool Nastran. In this framework, composite material is optimised by means of lamination parameters, and blending constraints have been implemented during the continuous optimisation to obtain a closer "ready-

to-manufacture" continuous design. In the second step, a surrogate model based on a rigid CFD (Computational Fluid Dynamic) analysis has been developed and used to include high-fidelity aerodynamic drag in the analysis and perform multi-objective optimisations. The surrogate relies on an original reduction technique used to approximate the wing structural deflection with a limited number of inputs. The surrogate model has been integrated into the commercial FEM software Nastran via Direct Matrix Abstraction Program and third-party integration software capability and applied to a realistic industrial case.

The conclusions of this dissertation can be found in Section 7.1, while Section 7.2 presents recommendations for future research activities.

## 7.1 CONCLUSIONS

This section contains the main conclusions of this dissertation.

### 7.1.1 EFFECT OF BLENDING CONSTRAINTS ON CONTINUOUS OPTIMUM AND STACKING SEQUENCE RETRIEVAL



A set of blending constraints in the lamination parameter space, introduced in Section 2.4, is used to enforce blending during the gradient-based continuous optimisation. These constraints link the number of ply-drops between adjacent composite patches and the allowed change in lamination parameters, limiting the change in stiffness to the change in thickness between patches.

The direct effect of using blending constraints during the continuous optimisation is a reduction of the lamination parameters design space. This reduction in design space results in heavier optimised structures (approximately 5%) compared to the case where blending constraints are not implemented. However, the use of these constraints allowed to obtain more gradual thickness and stiffness changes between adjacent panels by removing those areas where it is impossible to find a blended solution from the design space.

By looking at the solutions found by the optimiser, all retrieved wings had thickness concentrated at the leading edge and close to the root. This solution results in a wing elastic axis located close to the leading edge and thus creates a wing wash-out effect under bending that shifts the lift distribution towards the wing root, resulting in a lighter wing design. The introduction of the blending constraints does not significantly alter this thickness distribution but drastically reduces thickness and stiffness jumps across patches.

Once an optimum design is obtained using lamination parameters, each wing patch's stiffness matrix and thickness are defined. However, a stacking sequence

retrieval process is necessary to obtain the discrete stacking sequence needed to build the structure. The stacking sequence retrieval has been performed in this dissertation by a simple genetic algorithm that only aimed at minimising the RMSE (Root Mean Square Error) between the lamination parameters from the continuous optimum and the retrieved discrete stacking sequence without taking into account any mechanical performance. The GA (Genetic Algorithm) is guide-based and therefore could only retrieve blended stacking sequences.

The main effect of the blending constraints on the stacking sequence retrieval is the reduction of about 60% in the lamination parameters RMSE between the discrete stacking sequence and the continuous optimum, showing that the continuous design obtained with blending constraints is much closer to the discrete solution. In the studies performed in this dissertation, even when blending constraints have been included, the stacking sequence retrieval step never managed to find a discrete solution with zero RMSE; therefore, the retrieved structure always resulted in some failed constraints. Nevertheless, the smaller RMSE significantly reduces the number of failed elements ($44\% - 54\%$), the mean failure indices ($10\% - 15\%$) and the maximum failure indices ($19\% - 43\%$) for both strength and buckling.

The presence of some failed constraints required some adjustments in the form of thickness correction to satisfy all mechanical constraints. As a consequence, while the use of blending constraints results in about 5% heavier continuous design compared to a design obtained without blending constraints, the retrieved and corrected stacking sequence capable of satisfying all mechanical constraints is $1.5\% - 3.7\%$ lighter. These results justify the need to account for blending in the design phase as early as possible to reduce the final step weight penalty.



### 7.1.2 Impact of the dynamic loads on continuous optimum

Dynamic loads have been included in the optimisations through an equivalent static load (ESL) method. The ESL computes static loads capable of generating the same displacement fields of the transient load at critical time steps. These static loads are then considered independent from the design and used during the optimisation, relying on a weak coupling between the transient simulations and the optimiser.

The inclusion of dynamic loads did not result in a significant change in the thickness and stiffness distributions for the composite regional wing model under study. The contained impact of the gusts on the final design can be seen in the weight difference $< 0.5\%$ but also in the limited areas of the wing associated with high failure indices for the mechanical constraints coming from the additional dynamic loads.

Even if gust loads have not been found to have a significant impact on the design under consideration, it is recognised that both static and dynamic loads shall

be taken into consideration since the early design phase (Kenway et al., 2014; Lancelot and De Breuker, 2016; Werter, 2017) to provide the optimiser with all the relevant load cases. To this end, the ESL has proved its capability to include dynamic loads inside a commercial optimisation tool even without utilizing the sensitivity of the loads.

### 7.1.3 Effect of high fidelity aerodynamic drag on aeroelastic tailoring

To overcome the panel methods limitation in computing only induced drag, a surrogate model of the total drag based on rigid high-fidelity CFD analyses has been developed and implemented into the optimisation process to perform a multi-objective trade-off between weight and aerodynamic drag minimisation.

The first step in creating the surrogate model was to derive an approximation of the wing elastic displacement with minimum residual error, valid for the entire optimisation process. To achieve this, an original reduction technique based on classical modal projection and advanced statistical techniques has been developed in order to approximate the wing structural deflection with a limited number of inputs, suitable for machine learning models. The resulting model, with 13 principal coordinates, is capable of approximating the wing displacements with a maximum absolute error that averages at 2.5 mm, approximately 0.015% of the wingspan.



In the second step, the retrieved model was used in a design of experiment (DOE) to generate several deflected structures. These structures, together with a range of angles of attack, have been used as inputs for the rigid CFD analyses, and the resulting drag coefficients have been used to generate the surrogate model. A polynomial regression with elastic net regularisation (PR-ENET) model has been used to fit the data coming from the DOE, and the resulting model had a generalisation RMSE of 1.29 d.c., approximately 0.7% of lowest drag obtained in this dissertation.

The multi-objective optimisation allowed the retrieval of two Pareto fronts: one obtained with blending constraints and one without. The presence of the blending constraints does not impact the trend of the Pareto fronts but, as shown earlier, results in heavier design between 3.8% and 5.9% at the end of the continuous optimisation. The Pareto fronts show that when structural weight minimisation is privileged, the optimiser favours structures with wash-out behaviour that reduces the lift at the wingtip and, thus, the wing root bending moment and the structural weight. To maintain a lift equal to the aircraft's weight, the aircraft needs to fly at a higher angle of attack, increasing the aerodynamic drag. If, instead, the drag coefficient minimisation is privileged, the optimiser results in a stiffer wing with less wash-out behaviour but allows the aircraft to fly at a lower angle of attack.

Validation of the results against the full order model CFD shows the absolute error in the drag coefficient $C_D$ varies between 0.9 and 1.6 d.c., in line with the estimated generalisation RMSE of 1.29 d.c.

## 7.2 RECOMMENDATIONS

The framework presented in this dissertation is a step towards including structural analysis, aerodynamic drag and composite manufacturing constraints early in the aircraft design process. However, several aspects have not been considered; therefore, this section presents some recommendations for further development of the proposed framework.

From the structural modelling side, local buckling in the upper and lower wing skin is computed via a closed formula suitable for computing buckling under biaxial loading of a simply supported plate. The formula does not consider the effects of shear fluxes and non-orthotropic composite bending stiffness effects (i.e. $D_{13}$ and $D_{23}$ non-zero) that degrade buckling critical factors. A different formulation could be implemented via the Rayleigh-Ritz method to overcome these limitations. In addition, local buckling could also be extended to the front and rear spars, and both strength and bucking could be extended to ribs and stringers.

Considering interlaminar shear stress in composite design is crucial for ensuring the structural integrity and longevity of composite materials. Interlaminar shear stresses can lead to delamination, a predominant failure mode in composites. Several factors influence these stresses. On the laminate level these factors are the Poisson's ratio and coefficient of thermal expansion (CTE) mismatch between adjacent plies, the number of identical contiguous plies and the number of ply drops at the same location can exacerbate these stress concentrations. Additionally, other aspects include out-of-plane loads, bending of curved sections, and the presence of bonded joints. Addressing these factors in the design phase can mitigate the risk of delamination, leading to more robust and reliable composite structures.

About the use of the surrogate models to include aerodynamic drag during structural optimisation, Chapter 6 showed the capability of the proposed framework to produce trade-off studies between weight minimisation and aerodynamic drag minimisation. However, the study does not identify what solution leads to the most efficient aircraft. To achieve this, the Breguet range equation could be used and integrated into a single objective function containing both the aircraft weight and the drag. Also, multipoint optimisation could be included to take into account the estimate of the aircraft drag at different mass configurations and, therefore, the different trim angles of attack and wing elastic deflections.

The surrogate model presented in this dissertation is based on the aircraft's angle

of attack and the wing elastic deflection. However, the approach presented in this dissertation could be extended to include aerodynamic shape changes. For example, by adding parameters linked to the winglet length, sweep and cant angles, it would be possible to optimise both wing structure and winglet shape to achieve a certain target in weight and drag. In case the simple methods considered in this dissertation would not produce sufficiently accurate results, more sophisticated models like Artificial Neural Network (ANN) and Kriging should be considered or even Mixtures of Experts (MoE) which would allow to consider multi-regime behaviour in one sole equation.

Finally, by including both winglet shape optimisation and multipoint in the structural optimisation, it would be possible to investigate both a single solution for the different flight regimes (e.g. cruise, climb and descent) or, by assuming some winglet morphing capabilities, unique solutions for the different flight phases.

Concerning the tools adopted during the optimisations, the GA used in this work for stacking sequence retrieval had access only to the target lamination parameters from the continuous optimum and the discrete stacking sequences and had the sole objective of minimising the RMSE between the two sets of lamination parameters. By providing the GA with additional information, such as critical constraint values and their sensitivity with respect to lamination parameters from the continuous optimisation (like in Irisarri et al. (2011) and Vicente (2019)), it will be possible to take into account constraints violation during stacking sequence retrieval. This would allow the provision of discrete stacking sequences that satisfy all constraints and thus be one step closer to delivering a "ready-to-manufacture" design.

# BIBLIOGRAPHY


M. M. Abdalla, S. Setoodeh, and Z. Gürdal. Design of variable stiffness composite panels for maximum fundamental frequency using lamination parameters. *Composite Structures*, 81(2):283 – 291, 2007. ISSN 0263-8223. doi: https://doi.org/10.1016/j.compstruct.2006.08.018.

M. M. Abdalla, Z. Gürdal, and C. Kassapoglu. Formulation of composite laminate robustness constraint in lamination parameters space. In *50th AIAA/ASME/ASCE/AHS/ASC Structures, Structural Dynamics, and Materials Conference, Structures, Structural Dynamics, and Materials and Co-located Conferences, ()*, 2009. doi: http://dx.doi.org/10.2514/6.2009-2478.

D. M. Acosta, M. D. Guynn, R. A. Wahls, and R. Del Rosario. *Next Generation Civil Transport Aircraft Design Considerations for Improving Vehicle and System-Level Efficiency.* 2013. doi: 10.2514/6.2013-4286. URL https://arc.aiaa.org/doi/abs/10.2514/6.2013-4286.

D. B. Adams, L. T. Watson, Z. Gürdal, and C. M. Anderson-Coo. Genetic algorithm optimization and blending of composite laminates by locally reducing laminate thickness. *Advances in Engineering Software*, 35(1):35-43, 2004.

Airbus. *Global Market Forecast 2023*, 2023. URL https://www.airbus.com/sites/g/files/jlcbta136/files/2023-06/Airbus%20Global%20Market%20Forecast%202023-2042%20Presentation.pdf.

J. A. Bailie, R. P. Ley, and A. Pasricha. *A summary and review of composite laminate design guidelines. Technical report NASA, NAS1-19347.* Northrop Grumman - Military Aircraft Systems Division, 2002.

C. Benoit, S. Pron, and S. Landier. Cassiopee: A cfd pre- and post-processing tool. *Aerospace Science and Technology*, 45:272 – 283, 2015. ISSN 1270-9638. doi: https://doi.org/10.1016/j.ast.2015.05.023. URL http://www.sciencedirect.com/science/article/pii/S1270963815001777.

D. Bettebghor and N. Bartoli. Approximation of the critical buckling factor for composite panels. *Structural and Multidisciplinary Optimization*, 46(4):561–584, Oct 2012. ISSN 1615-1488. doi: 10.1007/s00158-012-0784-6.

D. Bettebghor, C. Blondeau, D. Toal, and H. Eres. Machines vecteurs supports pour l'approximation de contraintes de couplage en optimisation composite. CSMA 2019 - 14me Colloque National en Calcul des Structures, May 2019. doi: 10.2514/6.2016-4122.

J. Bi and K. P. Bennett. Regression error characteristic curves. In *Proceedings of the Twentieth International Conference on International Conference on Machine Learning*, ICML'03, page 4350. AAAI Press, 2003. ISBN 1577351894.

M. W. Bloomfield, C. G. Diaconu, and P. M. Weaver. On feasible regions of lamination parameters for lay-up optimization of laminated composites. *Proceedings of the Royal Society A: Mathematical, Physical and Engineering Sciences*, 465 (2104):1123–1143, 2009a.

M. W. Bloomfield, J. E. Herencia, and P. M. Weaver. Enhanced two-level optimization of anisotropic laminated composite plates with strength and buckling constraints. *Thin-Walled Structures*, 47(11):1161 – 1167, 2009b. ISSN 0263-8231. doi: https://doi.org/10.1016/j.tws.2009.04.008. URL http://www.sciencedirect.com/science/article/pii/S0263823109001104.

N. P. Bons and J. R. R. A. Martins. Aerostructural design exploration of a wing in transonic flow. *Aerospace*, 7(8):118, Aug 2020. ISSN 2226-4310. doi: 10.3390/aerospace7080118. URL http://dx.doi.org/10.3390/aerospace7080118.

T. R. Brooks, G. K. W. Kenway, and J. R. R. A. Martins. Benchmark aerostructural models for the study of transonic aircraft wings. *AIAA Journal*, 56 (7):2840–2855, 2018. doi: 10.2514/1.J056603. URL https://doi.org/10.2514/1.J056603.

T. R. Brooks, J. R. R. A. Martins, and G. J. Kennedy. High-fidelity aerostructural optimization of tow-steered composite wings. *Journal of Fluids and Structures*, 88:122 – 147, 2019. ISSN 0889-9746. doi: https://doi.org/10.1016/j.jfluidstructs.2019.04.005. URL http://www.sciencedirect.com/science/article/pii/S0889974618306340.

D. A. Burdette and J. R. R. A. Martins. Design of a transonic wing with an adaptive morphing trailing edge via aerostructural optimization. *Aerospace Science and Technology*, 81:192 – 203, 2018. ISSN 1270-9638. doi: https://doi.org/10.1016/j.ast.2018.08.004. URL http://www.sciencedirect.com/science/article/pii/S1270963818308344.

L. Cambier, M. Gazaix, S. Heib, S. Plot, M. Poinot, J.-P. Veuillot, J.-F. Boussuge, and M. Montagnac. An overview of the multi-purpose elsa flow solver. *Aerospace Lab Journal*, 2, 2011.

R. Carmichael and L. Erickson. *PAN AIR - A higher order panel method for predicting subsonic or supersonic linear potential flows about arbitrary configurations*. doi: 10.2514/6.1981-1255. URL https://arc.aiaa.org/doi/abs/10.2514/6.1981-1255.

F. G. Di Vincenzo. Hybrid static aeroelasticity new capabilities - cfd data management, 06 2012.

J. K. S. Dillinger. *Static Aeroelastic Optimization of Compisite Wing with Variable Stiffness Laminates*. PhD thesis, Delft University of Technology, 2014.

J. K. S. Dillinger, T. Klimmek, M. M. Abdalla, and Z. Gürdal. Stiffness optimization of composite wings with aeroelastic constraints. *Journal of Aircraft*, 50 (4):1159–1168, 2013. doi: 10.2514/1.C032084.

J. K. S. Dillinger, M. M. Abdalla, Y. M. Meddaikar, and T. Klimmek. Static aeroelastic stiffness optimization of a forward swept composite wing with cfd-corrected aero loads. *CEAS Aeronautical Journal*, 10(4):1015–1032, 2019. doi: 10.1007/s13272-019-00397-y. URL https://doi.org/10.1007/s13272-019-00397-y.

J. Duchon. Splines minimizing rotation-invariant semi-norms in sobolev spaces. In Walter Schempp and Karl Zeller, editors, *Constructive Theory of Functions of Several Variables*, pages 85–100, Berlin, Heidelberg, 1977. Springer Berlin Heidelberg. ISBN 978-3-540-37496-1.

EASA. *CS25 - Certification Specifications and Acceptable Means of Compliance for Large Aeroplanes - Amendment 21*. March 2018.

European Commission. *Flightpath 2050: Europe's vision for aviation*, 2011. EUR 098 EN.

A. I. J. Forrester and A. J. Keane. Recent advances in surrogate-based optimization. *Progress in Aerospace Sciences*, 45(1):50 – 79, 2009. ISSN 0376-0421. doi: https://doi.org/10.1016/j.paerosci.2008.11.001. URL http://www.sciencedirect.com/science/article/pii/S0376042108000766.

H. Fukunaga and H. Sekine. A laminate design for elastic properties of symmetric laminates with extension-shear or bending-twisting coupling. *Journal of Composite Materials*, 28(8):708–731, 1994. doi: 10.1177/002199839402800802. URL https://doi.org/10.1177/002199839402800802.

H. Ghiasi, D. Pasini, and L. Lessard. Optimum stacking sequence design of composite materials part i: Constant stiffness design. *Composite Structures*, 90:1–11, 2009. February.

H. Ghiasi, K. Fayazbakhsh, D. Pasini, and Larry Lessard. Optimum stacking sequence design of composite materials part ii: Variable stiffness design. *Composite Structures*, 93:1–13, June 2010.

J. P. Giesing, T. P. Kalman, and W. P. Rodden. Subsonic unsteady aerodynamics for general configurations. *Tech. Rep. AFFDL-TR-71-5, Part II, Vol. II, Air Force Flight Dynamics Laboratory*, 1972.

G. H. Golub and C. Reinsch. Singular value decomposition and least squares solutions. *Numerische Mathematik*, 14(5):403–420, 1970. doi: 10.1007/BF02163027. URL https://doi.org/10.1007/BF02163027.

J. L. Grenestedt and P. Gudmundson. Layup optimization of composite material structures. In Pauli PEDERSEN, editor, *Optimal Design with Advanced Materials*, pages 311 – 336. Elsevier, Oxford, 1993. ISBN 978-0-444-89869-2. doi: http://dx.doi.org/10.1016/B978-0-444-89869-2.50027-5.

Z. Gürdal, R. T. Haftka, and P. Hajela. *Design and Optimization of Laminated Composite Materials*. Wiley, West Sussex, UK, 1999.

R. T. Haftka and Z. Gürdal. *Elements of Structural Optimization*, volume 11. Springer, West Sussex, UK, 1992. doi: 1007/978-94-011-2550-5.

R. T. Haftka and J. L. Walsh. Stacking-sequence optimization for buckling of laminated plates by integer programming. *AIAA Journal*, 30(3):814–819, 1992. doi: 10.2514/3.10989. URL https://doi.org/10.2514/3.10989.

R. T. Haftka and L. T. Watson. Multidisciplinary design optimization with quasiseparable subsystems. *Optimization and Engineering*, 6(1):9–20, Mar 2005. ISSN 1573-2924. doi: 10.1023/B:OPTE.0000048534.58121.93.

Y. Y. Haimes, L. S. Lasdon, and D. A. Wismer. On a bicriterion formulation of the problems of integrated system identification and system optimization. *IEEE Transactions on Systems, Man, and Cybernetics*, SMC-1(3):296–297, 1971.

J. H. Halton. On the efficiency of certain quasi-random sequences of points in evaluating multi-dimensional integrals. *Numerische Mathematik*, 2(1):84–90, 1960. doi: 10.1007/BF01386213. URL https://doi.org/10.1007/BF01386213.

V. B. Hammer, M. P. Bendse, R. Lipton, and P. Pedersen. Parametrization in laminate design for optimal compliance. *International Journal of Solids and Structures*, 34(4):415 – 434, 1997. ISSN 0020-7683. doi: https://doi.org/10.1016/S0020-7683(96)00023-6. URL http://www.sciencedirect.com/science/article/pii/S0020768396000236.

M. Harmin, A. Abdelkader, J. Cooper, and F. Bron. *Aeroelastic Tailoring of Metallic Wing Structures*. 2011. doi: 10.2514/6.2011-1712. URL https://arc.aiaa.org/doi/abs/10.2514/6.2011-1712.

T. Hastie, R. Tibshirani, and J. Friedman. *The Elements of Statistical Learning*. Springer, 2017. doi: https://doi.org/10.1007/978-0-387-84858-7.

J. Herencia, P. Weaver, and M. Friswell. *Morphing wing design via aeroelastic tailoring*. 2007a. doi: 10.2514/6.2007-2214. URL https://arc.aiaa.org/doi/abs/10.2514/6.2007-2214.

J. E. Herencia, P. M. Weaver, and M. I. Friswell. Optimization of long anisotropic laminated fiber composite panels with t-shaped stiffeners. *AIAA Journal*, 45 (10):2497–2509, 2018/09/10 2007b. doi: 10.2514/1.26321.

ICAO. *Environmental Report 2022*, 2022. URL https://www.icao.int/environmental-protection/Documents/EnvironmentalReports/2022/ICAO%20ENV%20Report%202022%20F4.pdf.

ICAO. *ICAO forecasts complete and sustainable recovery and growth of air passenger demand in 20232*, 2023. URL https://www.icao.int/Newsroom/NewsDoc2023Fix/COM.02.23.EN.pdf.

S. T. IJsselmuiden, M. M. Abdalla, and Z. Gürdal. Implementation of strength-based failure criteria in the lamination parameter design space. *AIAA Journal*, 46(7):1826–1834., 2008.

S. T. IJsselmuiden, M. M. Abdalla, O. Seresta, and Z. Gürdal. Multi-step blended stacking sequence design of panel assemblies with buckling constraints. *Composites Part B: Engineering*, 40(4):329 – 336, 2009. ISSN 1359-8368. doi: http://dx.doi.org/10.1016/j.compositesb.2008.12.002.

S. T. IJsselmuiden, M. M. Abdalla, and Z. Gürdal. Optimization of variable-stiffness panels for maximum buckling load using lamination parameters. *AIAA Journal*, 48(1):134–143, 2018/09/10 2010. doi: 10.2514/1.42490.

F.-X. Irisarri, M. M. Abdalla, and Z. Grdal. Improved shepard's method for the optimization of composite structures. *AIAA Journal*, 49(12):2726–2736, 2011. doi: 10.2514/1.J051109. URL https://doi.org/10.2514/1.J051109.

F.-X. Irisarri, A. Lasseigne, F.-H. Leroy, and R. Le Riche. Optimal design of laminated composite structures with ply drops using stacking sequence tables. *Composite Structures*, 107:559 – 569, 2014. ISSN 0263-8223. doi: http://dx.doi.org/10.1016/j.compstruct.2013.08.030.

S. Jeong, M. Murayama, and K. Yamamoto. Efficient optimization design method using kriging model. *Journal of Aircraft*, 42(2):413–420, 2005. doi: 10.2514/1.6386. URL http://dx.doi.org/10.2514/1.6386.

P. Jin, X. Zhong, J. Yang, and Z. Sun. Blending design of composite panels with lamination parameters. *The Aeronautical Journal*, 120(1233):1710–1725, November 2016.

J.-C. Jouhaud, P. Sagaut, M. Montagnac, and J. Laurenceau. A surrogate-model based multidisciplinary shape optimization method with application to a 2d subsonic airfoil. *Computers and Fluids*, 36(3):520 – 529, 2007. ISSN 0045-7930. doi: https://doi.org/10.1016/j.compfluid.2006.04.001. URL http://www.sciencedirect.com/science/article/pii/S0045793006000582.

K. Jovanov. *High-Fidelity Load and Gradient Corrections for Static Aeroelastic Tailoring of Composite Wings*. PhD thesis, Delft University of Technology, 2019.

C. Jutte and B. K. Stanford. Aeroelastic tailoring of transport aircraft wings: State-of-the-art and potential enabling technologies. Technical report, April 2014.

M. Kameyama and H. Fukunaga. Optimum design of composite plate for aeroelastic characteristics using lamination parameters. *Computers and Structures*, 85(3-4):213–224, February 2007.

B. S. Kang, W. S. Choi, and G. J. Park. Structural optimization under equivalent static loads transformed from dynamic loads based on displacement. *Structural and Multidisciplinary Optimization*, 79(2):145–154, 2001.

B. S. Kang, G. J. Park, and J. S. Arora. A review of optimization of structures subjected to transient loads. *Structural and Multidisciplinary Optimization*, 31 (2):81–95, 2006.

C. Kassapoglou. *Design and Analysis of Composite Structures: With Applications to Aerospace Structures*. Wiley, West Sussex, UK, 2013.

G. J. Kennedy and J. R. R. A. Martins. A parallel aerostructural optimization framework for aircraft design studies. *Structural and Multidisciplinary Optimization*, 50(6):1079–1101, 2014. doi: 10.1007/s00158-014-1108-9. URL https://doi.org/10.1007/s00158-014-1108-9.

G. Kenway, G. Kennedy, and J. R. R. A. Martins. Aerostructural optimization of the Common Research Model configuration. In *15th AIAA/ISSMO Multidisciplinary Analysis and Optimization Conference*, June 2014.

G. K. W. Kenway and J. R. R. A. Martins. Multipoint high-fidelity aerostructural optimization of a transport aircraft configuration. *Journal of Aircraft*, 51(1): 144–160, 2014. doi: 10.2514/1.C032150. URL https://doi.org/10.2514/1.C032150.

G. Kreisselmeier and R. Steinhauser. Systematic control design by optimizing a vector performance index. *IFAC Proceedings Volumes*, 12(7):113 – 117, 1979. ISSN 1474-6670. doi: https://doi.org/10.1016/S1474-6670(17)65584-8. URL http://www.sciencedirect.com/science/article/

pii/S1474667017655848. IFAC Symposium on computer Aided Design of Control Systems, Zurich, Switzerland, 29-31 August.

B. P. Kristinsdottir, Z. B. Zabinsky, M. E. Tuttle, and S. Neogi. Optimal design of large composite panels with varying loads. *Composite Structures*, 51(1):93 – 102, 2001. ISSN 0263-8223. doi: https://doi.org/10.1016/S0263-8223(00)00128-8.

J. N. Krone. *Divergence elimination with advanced composites*. 1975. doi: 10.2514/6.1975-1009. URL https://arc.aiaa.org/doi/abs/10.2514/6.1975-1009.

P. Lancelot and R. De Breuker. Aeroelastic tailoring for gust load alleviation. In *11th ASMO/ISSMO/NOED2016 International Conference of Numerical Optimization Methods for Engineering Design*, July 2016.

R. Le Riche and R. T. Haftka. Optimization of laminate stacking sequence for buckling load maximization by genetic algorithm. *AIAA Journal*, 31(5):951–956, 1993. doi: 10.2514/3.11710. URL https://doi.org/10.2514/3.11710.

S. Lebofsky, E. Ting, N. T. Nguyen, and K. V. Trinh. *Aeroelastic Modeling and Drag Optimization of Flexible Wing Aircraft with Variable Camber Continuous Trailing Edge Flap*. American Institute of Aeronautics and Astronautics, 2014. doi: doi:10.2514/6.2014-2443. URL http://dx.doi.org/10.2514/6.2014-2443.

R. P. Liem, G. K. W. Kenway, and J. R. R. A. Martins. Multimission aircraft fuel-burn minimization via multipoint aerostructural optimization. *AIAA Journal*, 53(1):104–122, 2015. doi: 10.2514/1.J052940. URL https://doi.org/10.2514/1.J052940.

B. Liu. *Two-Level Optimization of Composite Wing Structure Based on Panel Genetic Optimization*. PhD thesis, Univeristy of Flodida, 2001.

B. Liu, R. T. Haftka, and P. Trompette. Maximization of buckling loads of composite panels using flexural lamination parameters. *Structural and Multidisciplinary Optimization*, 26(1):28–36, 2004. doi: 10.1007/s00158-003-0314-7. URL https://doi.org/10.1007/s00158-003-0314-7.

D. Liu, V. V. Toropov, O. M. Querin, and D. C. Barton. Bilevel optimization of blended composite wing panels. *Journal of Aircraft*, 48(1), 2011.

J. Liu, W. P. Song, Z. H. Han, and Y. Zhang. Efficient aerodynamic shape optimization of transonic wings using a parallel infilling strategy and surrogate models. *Structural and Multidisciplinary Optimization*, 55(3):925–943, 2017. doi: 10.1007/s00158-016-1546-7. URL https://doi.org/10.1007/s00158-016-1546-7.

T. Macquart. Optibless - an open-source toolbox for the optimisation of blended stacking sequences. In *In The seventeenth European Conference on Composite Materials (ECCM17)*, June 2016.

T. Macquart, M. T. Bordogna, P. Lancelot, and R. De Breuker. Derivation and application of blending constraints in lamination parameter space for composite optimisation. *Composite Structures*, 135:224 – 235, 2016. ISSN 0263-8223. doi: http://dx.doi.org/10.1016/j.compstruct.2015.09.016.

J. R. R. A. Martins, J. J. Alonso, and J. J. Reuther. High-fidelity aerostructural design optimization of a supersonic business jet. *Journal of Aircraft*, 41(3): 523–530, 2004. doi: 10.2514/1.11478. URL https://doi.org/10.2514/1.11478.

J. R. R. A. Martins, J. J. Alonso, and J. J. Reuther. A coupled-adjoint sensitivity analysis method for high-fidelity aero-structural design. *Optimization and Engineering*, 6(1):33–62, 2005. doi: 10.1023/B:OPTE.0000048536.47956.62. URL https://doi.org/10.1023/B:OPTE.0000048536.47956.62.

M. Miki. Material design of composite laminates with required in-plane elastic properties. *In Progress in science and engineering of composites (eds T. Hayashi, K. Kawata & S. Umekawa)*, 1:1725–1731, 1982.

MSC Software. *MSC Nastran Version 68 Aeroelastic Analysis User's Guide*, 2014a.

MSC Software. *MSC Nastran 2014.1 Design Sensitivity and Optimization User's Guide*, 2014b.

M. M. Munk. Propeller containing diagonally disposed fibrous material, 1949.

R. M. Paiva, A. R. D. Carvalho, C. Crawford, and A. Suleman. Comparison of surrogate models in a multidisciplinary optimization framework for wing design. *AIAA Journal*, 48(5):995–1006, 2010. doi: 10.2514/1.45790. URL http://dx.doi.org/10.2514/1.45790.

G. J. Park. Technical overview of the equivalent static loads method for nonlinear static response structural optimization. *Structural and Multidisciplinary Optimization*, 43:319–337, 2006.

Ö. Petersson. *Optimization of Aircraft Wings Including Dynamic Aeroelasticity and Manufacturing Aspects*. AIAA, 2018/08/03 2009. doi: 10.2514/6.2009-2226.

D. Rajpal, E. Gillebaart, and R. De Breuker. Preliminary aeroelastic design of composite wings subjected to critical gust loads. *Aerospace Science and Technology*, 85:96 – 112, 2019. ISSN 1270-9638. doi: https://doi.org/10.1016/j.ast.2018.11.051.

G. Raju, Z. Wu, and P. Weaver. On further developments of feasible region of lamination parameters for symmetric composite laminates. In *55th AIAA/ASME/ASCE/AHS/ASC Structures, Structural Dynamics, and Materials Conference, AIAA SciTech, (AIAA 2014-1374)*, 2014. doi: http://dx.doi.org/10.2514/6.2014-1374.

C.C. Rasmussen, R.A. Canfield, and M. Blair. Optimization process for configuration of flexible joined-wing. *Structural and Multidisciplinary Optimization*, 37(3):265, 2008. ISSN 1615-1488. doi: 10.1007/s00158-008-0229-4. URL http://dx.doi.org/10.1007/s00158-008-0229-4.

L. Reimer, M. Ritter, R. Heinrich, and W. Krüger. CFD-based Gust Load Analysis for a Free-flying Flexible Passenger Aircraft in Comparison to a DLM-based Approach. In *22nd AIAA Computational Fluid Dynamics Conference*, June 2015.

O. Seresta, M. Abdalla, and Z. Gurdal. A genetic algorithm based blending scheme for design of multiple composite laminates. In *50th AIAA/ASME/ASCE/AHS/ASC Structures, Structural Dynamics, and Materials Conference, Structures*, 2009. doi: http://dx.doi.org/10.2514/6.2009-2699.

S. Setoodeh, M. M. Abdalla, and Z. Gürdal. Combined topology and fiber path design of composite layers using cellular automata. *Structural and Multidisciplinary Optimization*, 30(6):413–421, 2005. doi: 10.1007/s00158-005-0528-y. URL https://doi.org/10.1007/s00158-005-0528-y.

S. Setoodeh, M. M. Abdalla, S. T. IJsselmuiden, and Zafer Grdal. Design of variable-stiffness composite panels for maximum buckling load. *Composite Structures*, 87(1):109 – 117, 2009. ISSN 0263-8223. doi: https://doi.org/10.1016/j.compstruct.2008.01.008. URL http://www.sciencedirect.com/science/article/pii/S0263822308000135.

M. H. Shirk, T. J. Hertz, and T. A. Weisshaar. Aeroelastic tailoring - theory, practice, and promise. *Journal of Aircraft*, 23(1):6–18, 1986. doi: http://dx.doi.org/10.2514/3.45260.

A. J. Smola and B. Schölkopf. A tutorial on support vector regression. *Statistics and Computing*, 14(3):199–222, 2004. doi: 10.1023/B:STCO.0000035301.49549.88. URL https://doi.org/10.1023/B:STCO.0000035301.49549.88.

W. Song and A. J. Keane. Surrogate-based aerodynamic shape optimization of a civil aircraft engine nacelle. *AIAA Journal*, 45(10):2565–2574, 2017/05/28 2007. doi: 10.2514/1.30015. URL http://dx.doi.org/10.2514/1.30015.

G. Soremekun, Z. Gürdal, C. Kassapoglou, and D. Toni. Stacking sequence blending of multiple composite laminates using genetic algorithms. *Composite Structures*, 56(1):53 – 62, 2002. ISSN 0263-8223. doi: http://dx.doi.org/10.1016/S0263-8223(01)00185-4.

B. K. Stanford and C. V. Jutte. Comparison of curvilinear stiffeners and tow steered composites for aeroelastic tailoring of aircraft wings. *Computers & Structures*, 183:48 – 60, 2017. ISSN 0045-7949. doi: https://doi.org/10.1016/j.compstruc.2017.01.010. URL http://www.sciencedirect.com/science/article/pii/S0045794916305569.

B. K. Stanford, C. V. Jutte, and K. Chauncey Wu. Aeroelastic benefits of tow steering for composite plates. *Computers & Structures*, 118:416 – 422, 2014. ISSN 0263-8223. doi: https://doi.org/10.1016/j.compstruct.2014.08.007. URL http://www.sciencedirect.com/science/article/pii/S0263822314003973.

J. Stegmann and E. Lund. Discrete material optimization of general composite shell structures. *International Journal for Numerical Methods in Engineering*, 62(14):2009–2027, 2005. doi: 10.1002/nme.1259. URL https://onlinelibrary.wiley.com/doi/abs/10.1002/nme.1259.

O. Stodieck, J. E. Cooper, P. M. Weaver, and P. Kealy. Improved aeroelastic tailoring using tow-steered composites. *Composite Structures*, 106:703 – 715, 2013. ISSN 0263-8223. doi: https://doi.org/10.1016/j.compstruct.2013.07.023. URL http://www.sciencedirect.com/science/article/pii/S0263822313003462.

O. Stodieck, J. E. Cooper, P. M. Weaver, and P. Kealy. Aeroelastic tailoring of a representative wing box using tow-steered composites. *AIAA Journal*, 55 (4):1425–1439, 2017. doi: 10.2514/1.J055364. URL https://doi.org/10.2514/1.J055364.

E. Torenbeek. *Advanced Aircraft Design: Conceptual Design, Analysis and Optimization of Subsonic Civil Airplanes*. Wiley, West Sussex, UK, 2013.

S. W. Tsai and H. T. Hahn. *Introduction to composite materials*. Technomic Publishing Co, 1980.

S. W. Tsai and N. J. Pagano. Invariant properties of composite materials. *Ft. Belvoir Defense Technical Information Center*, 1968.

US Department of Defense. *MIL-HDBK-17-3F. Military handbook, polymer matrix composites*. US Department of Defense, 2002.

J. van Campen, O. Seresta, M. M. Abdalla, and Z. Gürdal. General blending definitions for stacking sequence design of composite laminate structure. pages 7–10. 49th AIAA/ASME/ASCE/AHS/ASC structures, structural dynamics, and materials, 2008.

V. Vapnik. *The Nature of Statistical Learning Theory*. Springer, New York, 1995.

G. Verchery. Les invariants des tenseurs dordre 4 du type de llasticit. In Jean-Paul Boehler, editor, *Mechanical Behavior of Anisotropic Solids / Comportment Mchanique des Solides Anisotropes*, pages 93–104. Springer Netherlands, 1982. ISBN 978-94-009-6829-5. doi: 10.1007/978-94-009-6827-1_7.

F. Vicente. Stacking sequence retrieval of large composite structures in bi-step optimization strategies using mechanical constraints. Master's thesis, Delft University of Technology, 2019.

A. Wächter and L. T. Biegler. On the implementation of an interior-point filter line-search algorithm for large-scale nonlinear programming. *Mathematical Programming*, 106(1):25–57, Mar 2006. ISSN 1436-4646. doi: 10.1007/s10107-004-0559-y.

T. A.. Weisshaar. *Aeroelastic tailoring - Creative uses of unusual materials.* 1987. doi: 10.2514/6.1987-976. URL https://arc.aiaa.org/doi/abs/10.2514/6.1987-976.

N. P. M. Werter. *Aeroelastic Modelling and Design of Aeroelastically Tailored and Morphing Wings.* PhD thesis, Delft University of Technology, 2017.

Z. Wu, G. Raju, and P. Weaver. Feasible region of lamination parameters for optimization of variable angle tow (vat) composite plates. In *54th AIAA/ASME/ASCE/AHS/ASC Structures, Structural Dynamics, and Materials Conference, Structures, Structural Dynamics, and Materials and Co-located Conferences, ()*, 2013. doi: http://dx.doi.org/10.2514/6.2013-1481.

L. Zadeh. Optimality and non-scalar-valued performance criteria. *IEEE Transactions on Automatic Control*, 8(1):59–60, 1963. doi: 10.1109/TAC.1963.1105511.

K.-S. Zhang, Z.-H. Han, W.-J. Li, and W.-P. Song. Coupled aerodynamic/-structural optimization of a subsonic transport wing using a surrogate model. *Journal of Aircraft*, 45(6):2167–2171, 2017/05/28 2008. doi: 10.2514/1.36047. URL http://dx.doi.org/10.2514/1.36047.

H. Zou and T. Hastie. Regularization and variable selection via the elastic net. *Journal of the Royal Statistical Society: Series B (Statistical Methodology)*, 67(2):301–320, 2005. doi: https://doi.org/10.1111/j.1467-9868.2005.00503.x. URL https://rss.onlinelibrary.wiley.com/doi/abs/10.1111/j.1467-9868.2005.00503.x.

# A

# ADDITIONAL COMPATIBILITY CONSTRAINTS

As mentioned in Section 2.3.2, Raju et al. (2014) and Wu et al. (2013) derived the most complete closed formula that defines the feasible design space for both in-plane and out-of-plane lamination parameters.

$$
\begin{aligned}
&5\left(V_{1\mathbf{A}}-V_{1\mathbf{D}}\right)^2-2\left(1+V_{3\mathbf{A}}-2\left(V_{1\mathbf{A}}\right)^2\right)\leq 0 \qquad \text{(A.1)}\\
&-16+32V_{3\mathbf{A}}+40V_{2\mathbf{D}}^2+40V_{1\mathbf{D}}^2+16V_{4\mathbf{A}}^2-80V_{2\mathbf{A}}V_{2\mathbf{D}}+72V_{2\mathbf{A}}^2-80V_{1\mathbf{A}}V_{1\mathbf{D}}\\
&+72V_{1\mathbf{A}}^2-80V_{4\mathbf{A}}V_{1\mathbf{D}}V_{2\mathbf{D}}+80V_{2\mathbf{A}}V_{4\mathbf{A}}V_{1\mathbf{D}}-40V_{3\mathbf{A}}V_{2\mathbf{D}}^2-120V_{3\mathbf{A}}V_{1\mathbf{D}}^2\\
&-32V_{3\mathbf{A}}V_{4\mathbf{A}}^2+80V_{3\mathbf{A}}V_{2\mathbf{A}}V_{2\mathbf{D}}-72V_{3\mathbf{A}}V_{2\mathbf{A}}^2-32V_{3\mathbf{A}}^3+80V_{1\mathbf{A}}V_{4\mathbf{A}}V_{2\mathbf{D}}\\
&-144V_{1\mathbf{A}}V_{2\mathbf{A}}V_{4\mathbf{A}}+240V_{1\mathbf{A}}V_{3\mathbf{A}}V_{1\mathbf{D}}-216V_{1\mathbf{A}}^2V_{3\mathbf{A}}-25V_{1\mathbf{D}}^2V_{2\mathbf{D}}^2\\
&+50V_{2\mathbf{A}}V_{1\mathbf{D}}^2V_{2\mathbf{D}}-105V_{2\mathbf{A}}^2V_{1\mathbf{D}}^2+160V_{3\mathbf{A}}V_{4\mathbf{A}}V_{1\mathbf{D}}V_{2\mathbf{D}}-160V_{3\mathbf{A}}V_{2\mathbf{A}}V_{4\mathbf{A}}V_{1\mathbf{D}}\\
&-40V_{3\mathbf{A}}^2V_{2\mathbf{D}}^2+120V_{3\mathbf{A}}^2V_{1\mathbf{D}}^2+16V_{3\mathbf{A}}^2V_{4\mathbf{A}}^2+80V_{3\mathbf{A}}^2V_{2\mathbf{A}}V_{2\mathbf{D}}-72V_{3\mathbf{A}}^2V_{2\mathbf{A}}^2\\
&+16V_{3\mathbf{A}}^4+50V_{1\mathbf{A}}V_{1\mathbf{D}}V_{2\mathbf{D}}^2+20V_{1\mathbf{A}}V_{2\mathbf{A}}V_{1\mathbf{D}}V_{2\mathbf{D}}+90V_{1\mathbf{A}}V_{2\mathbf{A}}^2V_{1\mathbf{D}}\\
&-160V_{1\mathbf{A}}V_{3\mathbf{A}}V_{4\mathbf{A}}V_{2\mathbf{D}}+288V_{1\mathbf{A}}V_{3\mathbf{A}}V_{2\mathbf{A}}V_{4\mathbf{A}}-240V_{1\mathbf{A}}V_{3\mathbf{A}}^2V_{1\mathbf{D}}-105V_{1\mathbf{A}}^2V_{2\mathbf{D}}^2\\
&+90V_{1\mathbf{A}}^2V_{2\mathbf{A}}V_{2\mathbf{D}}-81V_{1\mathbf{A}}^2V_{2\mathbf{A}}^2+216V_{1\mathbf{A}}^2V_{3\mathbf{A}}^2+50V_{4\mathbf{A}}V_{1\mathbf{D}}V_{2\mathbf{D}}^3\\
&+\ldots
\end{aligned}
$$

$$
\begin{aligned}
&- 150V_{2\mathbf{A}}V_{4\mathbf{A}}V_{1\mathbf{D}}V_{2\mathbf{D}}^2 + 190V_{2\mathbf{A}}^2V_{4\mathbf{A}}V_{1\mathbf{D}}V_{2\mathbf{D}} - 90V_{2\mathbf{A}}^3V_{4\mathbf{A}}V_{1\mathbf{D}} + 50V_{3\mathbf{A}}V_{1\mathbf{D}}^2V_{2\mathbf{D}}^2 \\
&- 100V_{3\mathbf{A}}V_{2\mathbf{A}}V_{1\mathbf{D}}^2V_{2\mathbf{D}} + 210V_{3\mathbf{A}}V_{2\mathbf{A}}^2V_{1\mathbf{D}}^2 - 80V_{3\mathbf{A}}^2V_{4\mathbf{A}}V_{1\mathbf{D}}V_{2\mathbf{D}} \\
&+ 80V_{3\mathbf{A}}^2V_{2\mathbf{A}}V_{4\mathbf{A}}V_{1\mathbf{D}} + 40V_{3\mathbf{A}}^3V_{2\mathbf{D}}^2 - 40V_{3\mathbf{A}}^3V_{1\mathbf{D}}^2 - 80V_{3\mathbf{A}}^3V_{2\mathbf{A}}V_{2\mathbf{D}} + 72V_{3\mathbf{A}}^3V_{2\mathbf{A}}^2 \\
&- 50V_{1\mathbf{A}}V_{4\mathbf{A}}V_{2\mathbf{D}}^3 + 190V_{1\mathbf{A}}V_{2\mathbf{A}}V_{4\mathbf{A}}V_{2\mathbf{D}}^2 - 270V_{1\mathbf{A}}V_{2\mathbf{A}}^2V_{4\mathbf{A}}V_{2\mathbf{D}} + 162V_{1\mathbf{A}}V_{2\mathbf{A}}^3V_{4\mathbf{A}} \\
&- 100V_{1\mathbf{A}}V_{3\mathbf{A}}V_{1\mathbf{D}}V_{2\mathbf{D}}^2 - 40V_{1\mathbf{A}}V_{3\mathbf{A}}V_{2\mathbf{A}}V_{1\mathbf{D}}V_{2\mathbf{D}} - 180V_{1\mathbf{A}}V_{3\mathbf{A}}V_{2\mathbf{A}}^2V_{1\mathbf{D}} \\
&+ 80V_{1\mathbf{A}}V_{3\mathbf{A}}^2V_{4\mathbf{A}}V_{2\mathbf{D}} - 144V_{1\mathbf{A}}V_{3\mathbf{A}}^2V_{2\mathbf{A}}V_{4\mathbf{A}} + 80V_{1\mathbf{A}}V_{3\mathbf{A}}^3V_{1\mathbf{D}} + 210V_{1\mathbf{A}}^2V_{3\mathbf{A}}V_{2\mathbf{D}}^2 \\
&- 180V_{1\mathbf{A}}^2V_{3\mathbf{A}}V_{2\mathbf{A}}V_{2\mathbf{D}} + 162V_{1\mathbf{A}}^2V_{3\mathbf{A}}V_{2\mathbf{A}}^2 - 72V_{1\mathbf{A}}^2V_{3\mathbf{A}}^3 - 25V_{4\mathbf{A}}^2V_{2\mathbf{D}}^4 \\
&+ 100V_{2\mathbf{A}}V_{4\mathbf{A}}^2V_{2\mathbf{D}}^3 - 190V_{2\mathbf{A}}^2V_{4\mathbf{A}}^2V_{2\mathbf{D}}^2 + 180V_{2\mathbf{A}}^3V_{4\mathbf{A}}^2V_{2\mathbf{D}} - 81V_{2\mathbf{A}}^4V_{4\mathbf{A}}^2 \\
&- 50V_{3\mathbf{A}}V_{4\mathbf{A}}V_{1\mathbf{D}}V_{2\mathbf{D}}^3 + 150V_{3\mathbf{A}}V_{2\mathbf{A}}V_{4\mathbf{A}}V_{1\mathbf{D}}V_{2\mathbf{D}}^2 - 190V_{3\mathbf{A}}V_{2\mathbf{A}}^2V_{4\mathbf{A}}V_{1\mathbf{D}}V_{2\mathbf{D}} \\
&+ 90V_{3\mathbf{A}}V_{2\mathbf{A}}^3V_{4\mathbf{A}}V_{1\mathbf{D}} - 25V_{3\mathbf{A}}^2V_{1\mathbf{D}}^2V_{2\mathbf{D}}^2 + 50V_{3\mathbf{A}}^2V_{2\mathbf{A}}V_{1\mathbf{D}}^2V_{2\mathbf{D}} - 105V_{3\mathbf{A}}^2V_{2\mathbf{A}}^2V_{1\mathbf{D}}^2 \\
&+ 50V_{1\mathbf{A}}V_{3\mathbf{A}}V_{4\mathbf{A}}V_{2\mathbf{D}}^3 - 190V_{1\mathbf{A}}V_{3\mathbf{A}}V_{2\mathbf{A}}V_{4\mathbf{A}}V_{2\mathbf{D}}^2 + 270V_{1\mathbf{A}}V_{3\mathbf{A}}V_{2\mathbf{A}}^2V_{4\mathbf{A}}V_{2\mathbf{D}} \\
&- 162V_{1\mathbf{A}}V_{3\mathbf{A}}V_{2\mathbf{A}}^3V_{4\mathbf{A}} + 50V_{1\mathbf{A}}V_{3\mathbf{A}}^2V_{1\mathbf{D}}V_{2\mathbf{D}}^2 + 20V_{1\mathbf{A}}V_{3\mathbf{A}}^2V_{2\mathbf{A}}V_{1\mathbf{D}}V_{2\mathbf{D}} \\
&+ 90V_{1\mathbf{A}}V_{3\mathbf{A}}^2V_{2\mathbf{A}}^2V_{1\mathbf{D}} - 105V_{1\mathbf{A}}^2V_{3\mathbf{A}}^2V_{2\mathbf{D}}^2 + 90V_{1\mathbf{A}}^2V_{3\mathbf{A}}^2V_{2\mathbf{A}}V_{2\mathbf{D}} \\
&- 81V_{1\mathbf{A}}^2V_{3\mathbf{A}}^2V_{2\mathbf{A}}^2 \leq 0
\end{aligned}
\tag{A.2}
$$

# B

# Optimisation results from Chapter 5

## B.1 Case A

### B.1.1 Thickness and stiffness distribution

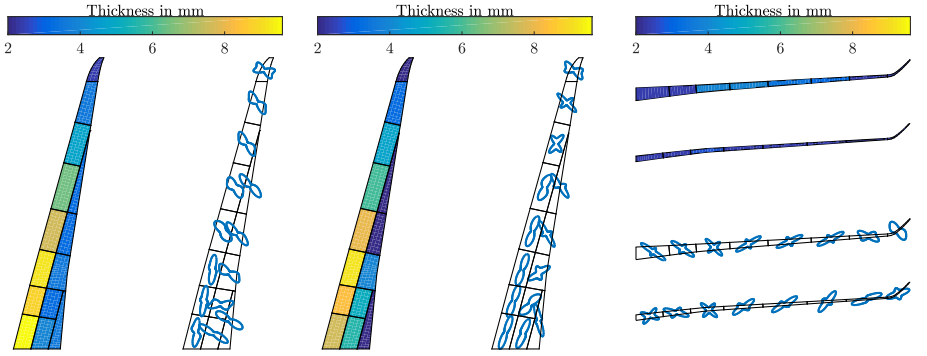


**(a)** Upper wing skin **(b)** Lower wing skin **(c)** Wing front and rear spars

**Figure B.1:** Wing thickness and stiffness distributions.

## B.1.2 MECHANICAL CONSTRAINTS FAILURE INDEX

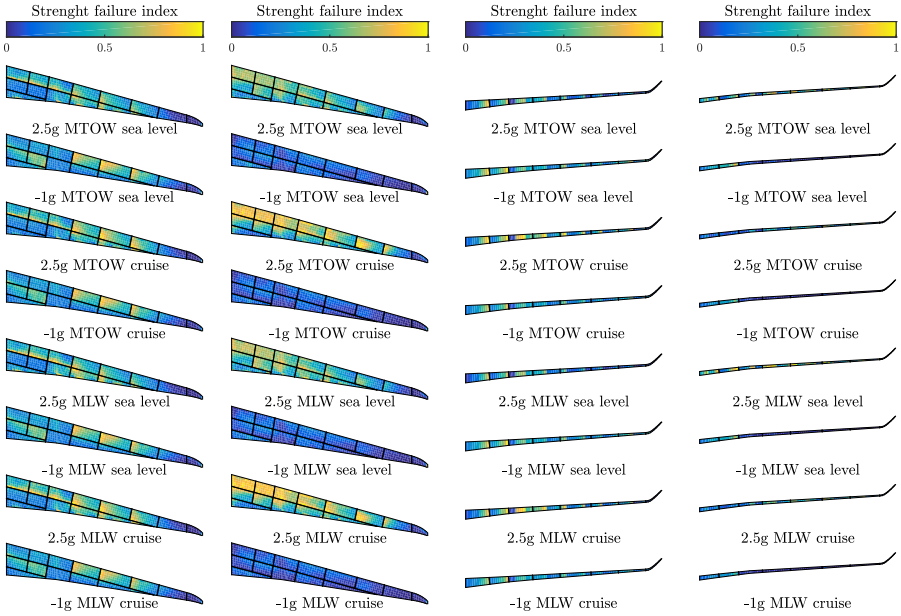


**(a)** Upper Skin **(b)** Lower Skin **(c)** Front Spar **(d)** Rear Spar

**Figure B.2:** Failure indices of the strength constraints at continuous optimum for different load cases.

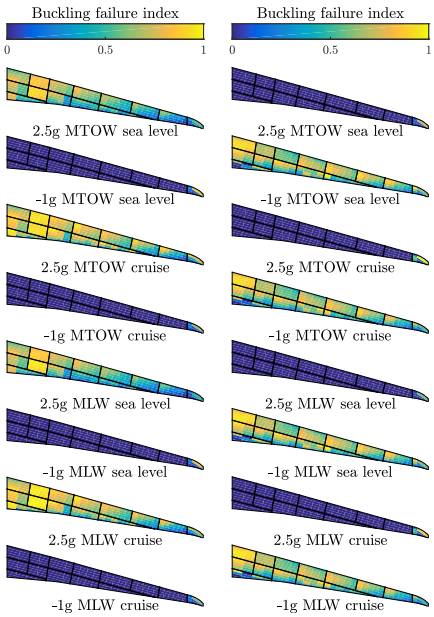


**(a)** Upper Skin **(b)** Lower Skin

**Figure B.3:** Failure indices of the buckling constraints at continuous optimum for different load cases.

## B.1.3 CRITICAL MECHANICAL CONSTRAINTS AND LOAD CASES

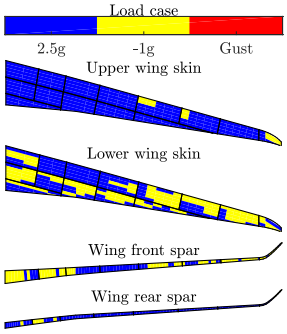


**Figure B.4:** Load-cases associated with the most active mechanical costraints at continuous optimum.

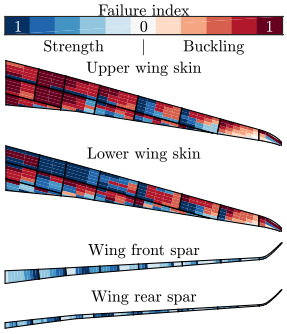


**Figure B.5:** Most critical failure index based on mechanical constraints at continuous optimum.

## B.2 CASE B

### B.2.1 THICKNESS AND STIFFNESS DISTRIBUTION



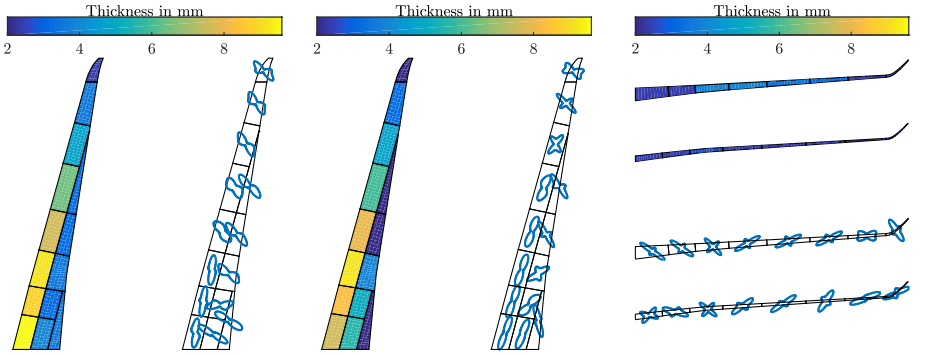


**(a)** Upper wing skin **(b)** Lower wing skin **(c)** Wing front and rear spars

**Figure B.6:** Wing thickness and stiffness distributionss.

## B.2.2 MECHANICAL CONSTRAINTS FAILURE INDEX

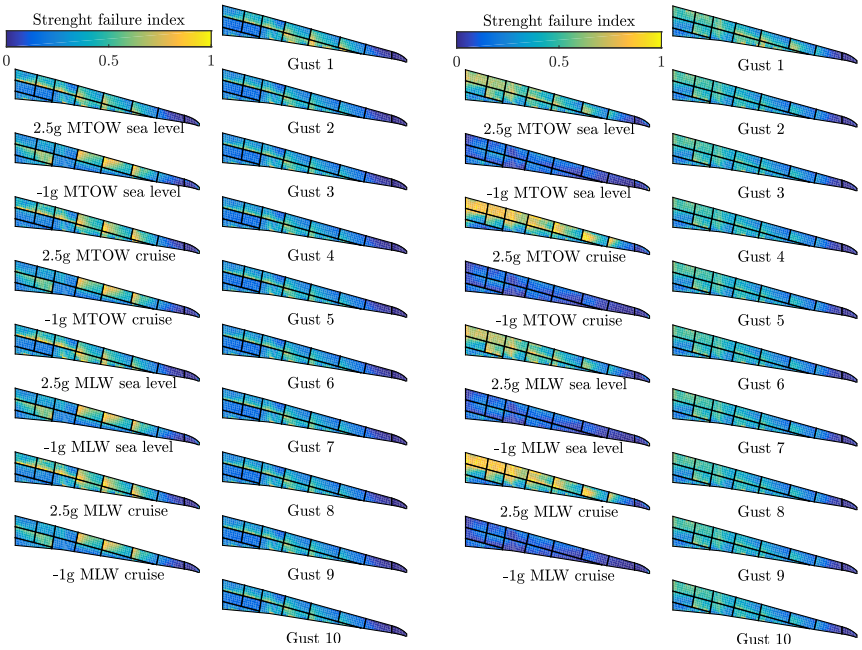


**(a)** Upper Skin **(b)** Lower Skin

**Figure B.7:** Failure indices of the strength constraints at continuous optimum.

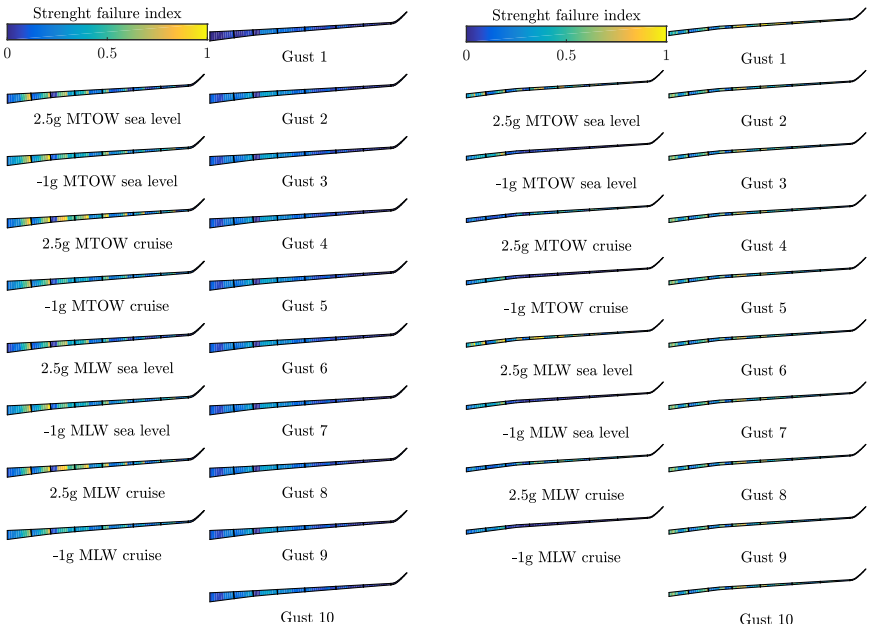


**(a)** Front Spar **(b)** Rear Spar

**Figure B.8:** Failure indices of the strength constraints at continuous optimum.

## B.2.3 CRITICAL MECHANICAL CONSTRAINTS AND LOAD CASES

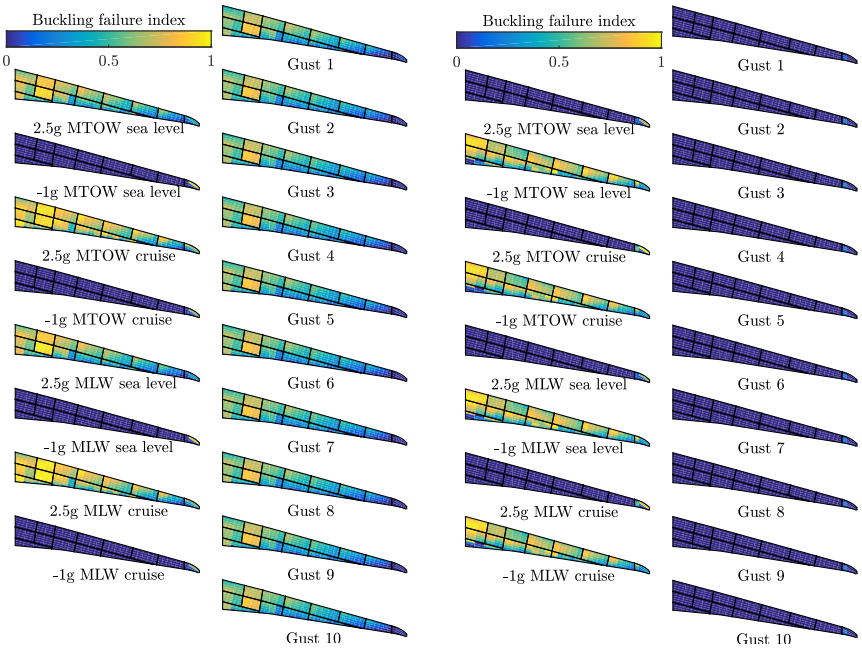


**(a)** Upper Skin **(b)** Lower Skin

**Figure B.9:** Failure indices of the buckling constraints at continuous optimum.

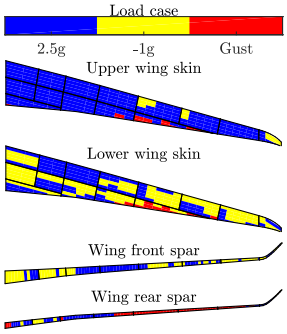


**Figure B.10:** Load-cases associated with the most active mechanical costraints at continuous optimum.

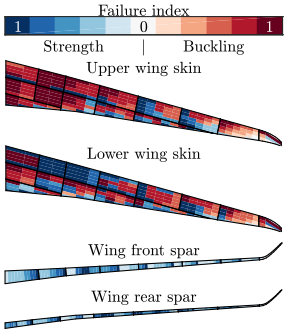


**Figure B.11:** Most critical failure index based on mechanical constraints at continuous optimum.

# B.3 CASE C

## B.3.1 THICKNESS AND STIFFNESS DISTRIBUTION



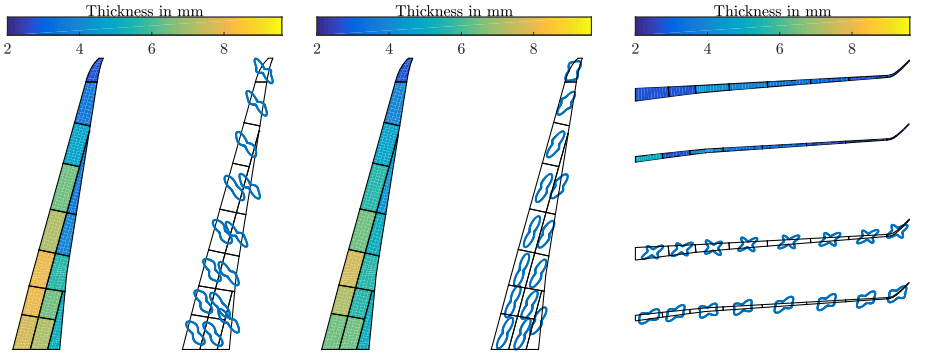


**(a)** Upper wing skin **(b)** Lower wing skin **(c)** Wing front and rear spars

**Figure B.12:** Wing thickness and stiffness distributions.

## B.3.2 MECHANICAL CONSTRAINTS FAILURE INDEX

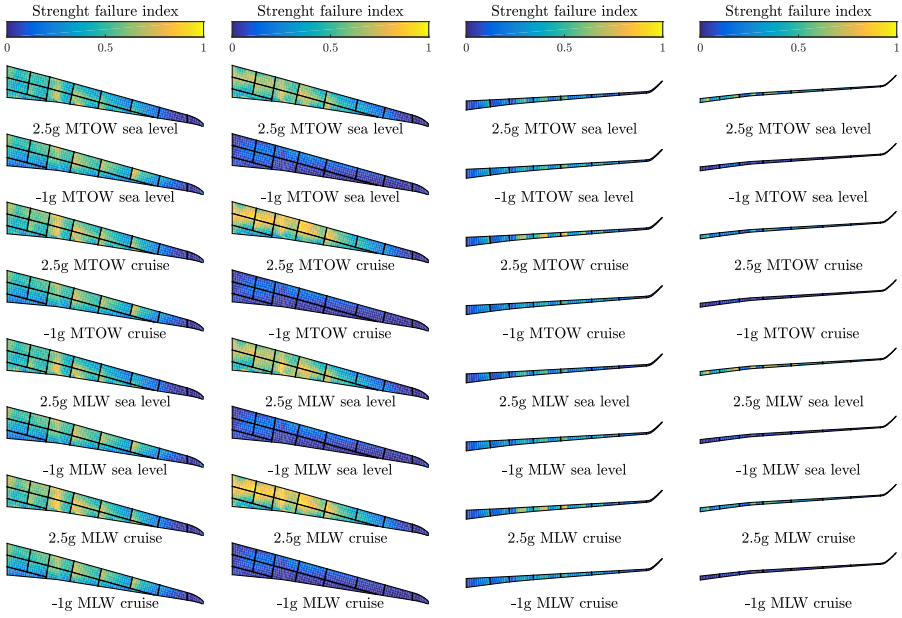


**(a)** Upper Skin **(b)** Lower Skin **(c)** Front Spar **(d)** Rear Spar

**Figure B.13:** Failure indices of the strength constraints at continuous optimum.

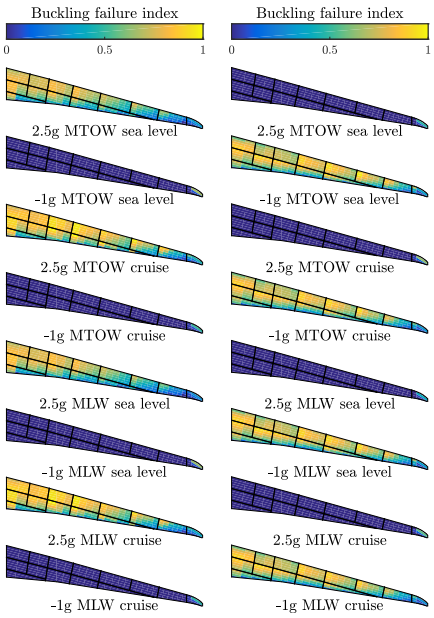


**(a)** Upper Skin **(b)** Lower Skin

**Figure B.14:** Failure indices of the buckling constraints at continuous optimum..

## B.3.3 CRITICAL MECHANICAL CONSTRAINTS AND LOAD CASES

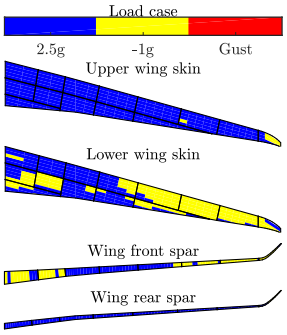


**Figure B.15:** Load-cases associated with the most active mechanical costraints at continuous optimum.

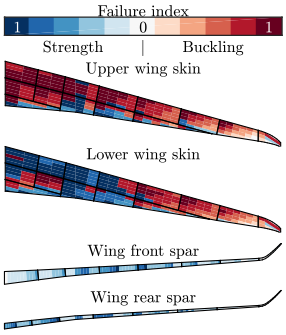


**Figure B.16:** Most critical failure index based on mechanical constraints at continuous optimum.

## B.4 CASE D

### B.4.1 THICKNESS AND STIFFNESS DISTRIBUTION



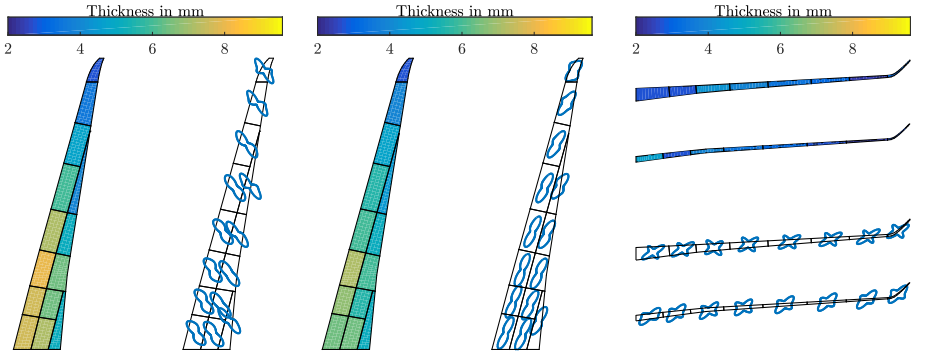


**(a)** Upper wing skin **(b)** Lower wing skin **(c)** Wing front and rear spars

**Figure B.17:** Wing thickness and stiffness distributions.

## B.4.2 MECHANICAL CONSTRAINTS FAILURE INDEX

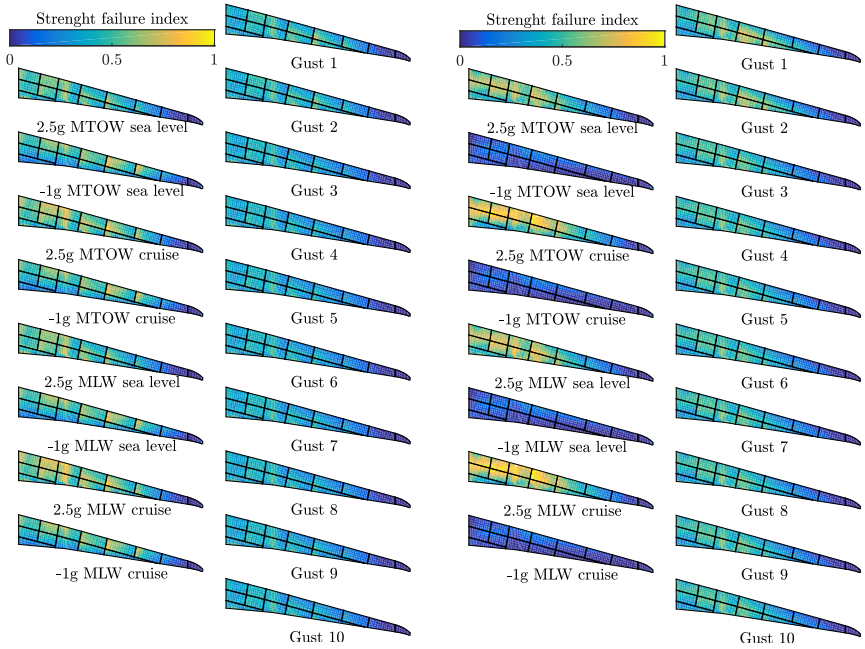


**(a)** Upper Skin **(b)** Lower Skin

**Figure B.18:** Failure indices of the strength constraints at continuous optimum.

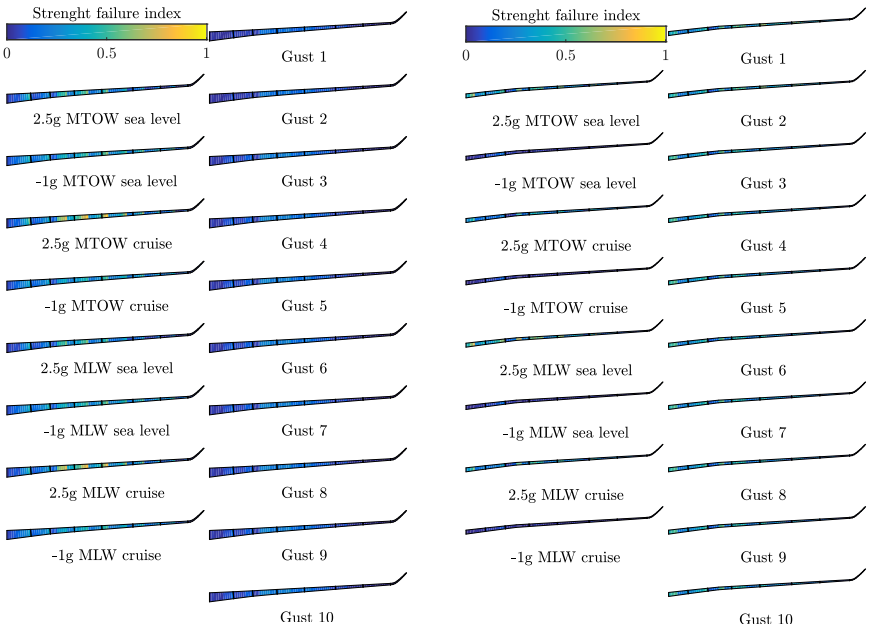


**(a)** Front Spar **(b)** Rear Spar

**Figure B.19:** Failure indices of the strength constraints at continuous optimum.

## B.4.3 CRITICAL MECHANICAL CONSTRAINTS AND LOAD CASES

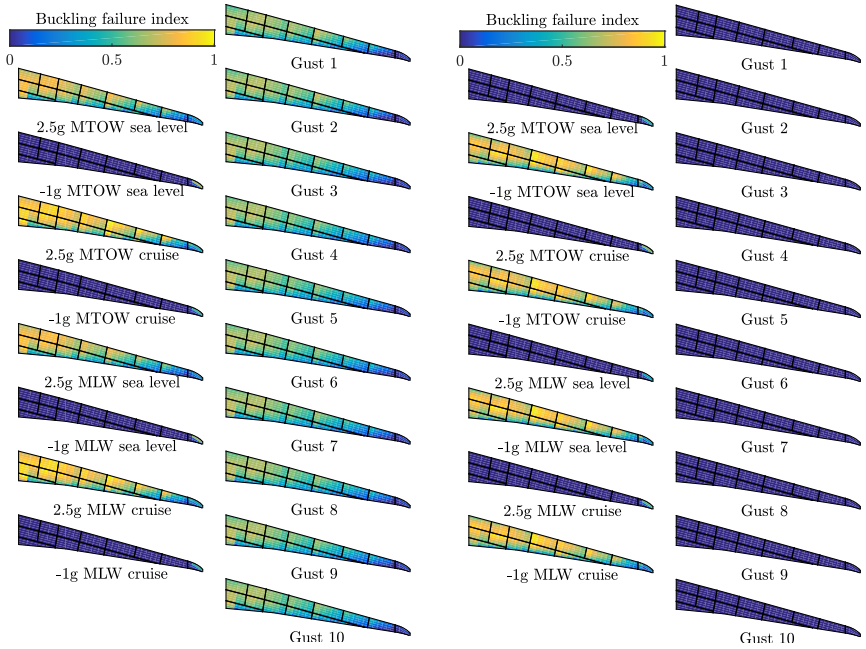


**(a)** Upper Skin **(b)** Lower Skin

**Figure B.20:** Failure indices of the buckling constraints at continuous optimum.

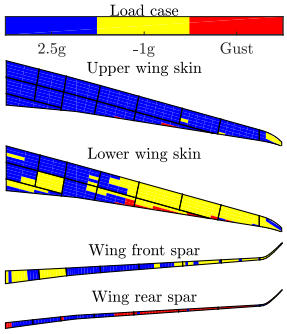


**Figure B.21:** Load-cases associated with the most active mechanical costraints at continuous optimum.

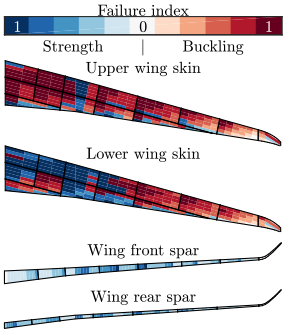


**Figure B.22:** Most critical failure index based on mechanical constraints at continuous optimum.

## B.5 Comparison: Case A - Case B

### B.5.1 Thickness and stiffness distribution



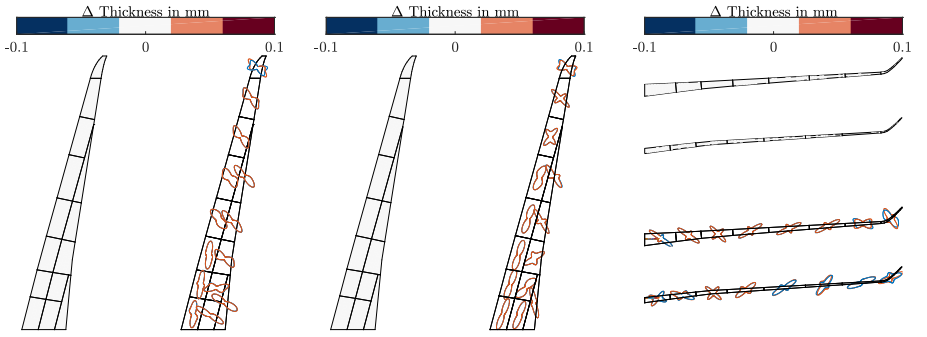


**(a)** Upper wing skin **(b)** Lower wing skin **(c)** Wing front and rear spars

**Figure B.23:** Comparison Case A and Case B.

## B.6 Comparison: Case A - Case C

### B.6.1 Thickness and stiffness distribution

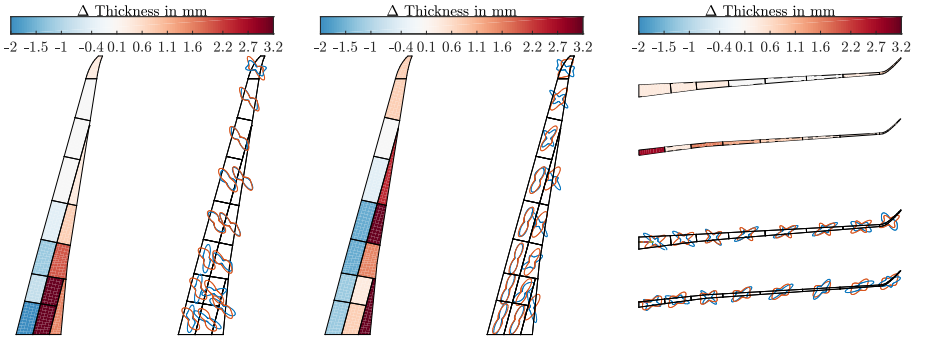


**(a)** Upper wing skin **(b)** Lower wing skin **(c)** Wing front and rear spars

**Figure B.24:** Comparison Case A and Case C.

B

## B.7 Comparison: Case B - Case D

### B.7.1 Thickness and stiffness distribution

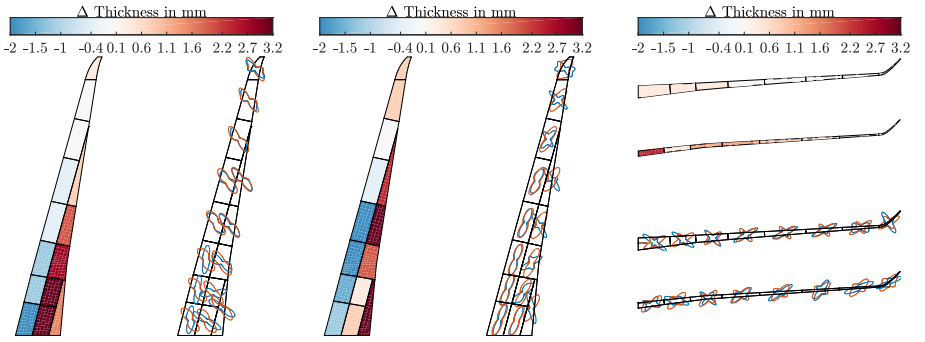


**(a)** Upper wing skin **(b)** Lower wing skin **(c)** Wing front and rear spars

**Figure B.25:** Comparison Case B and Case D.

## B.8 Comparison: Case C - Case D

### B.8.1 Thickness and stiffness distribution

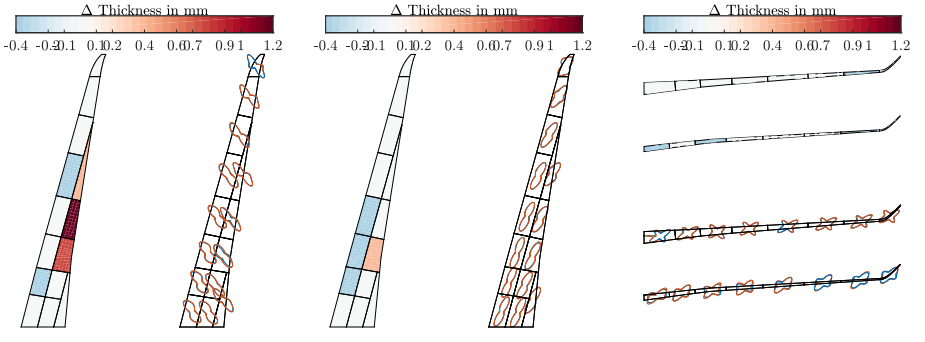


**(a)** Upper wing skin **(b)** Lower wing skin **(c)** Wing front and rear spars

**Figure B.26:** Comparison Case C and Case D.

# C

# STRUCTURAL MODES EVOLUTION

The first nine structural modes from $\mathbf{\Phi}$ in Figures C.1.

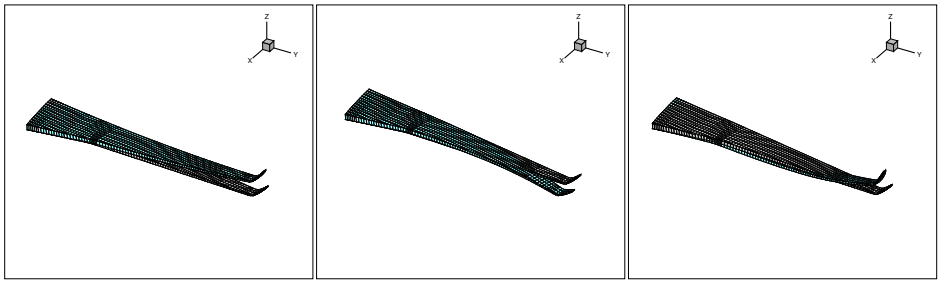

**(a)** Mode 1 **(b)** Mode 2 **(c)** Mode 3

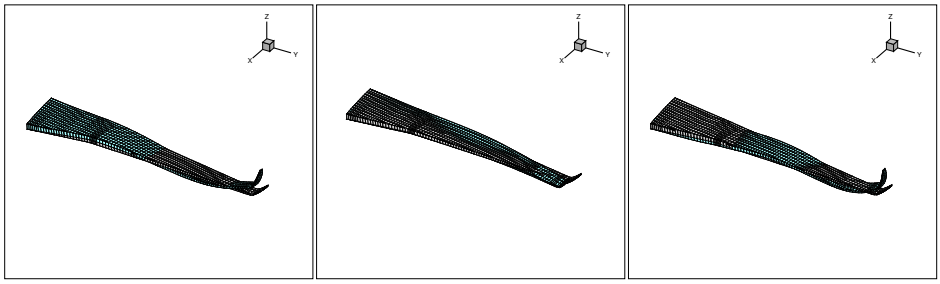

**(d)** Mode 4 **(e)** Mode 5 **(f)** Mode 6

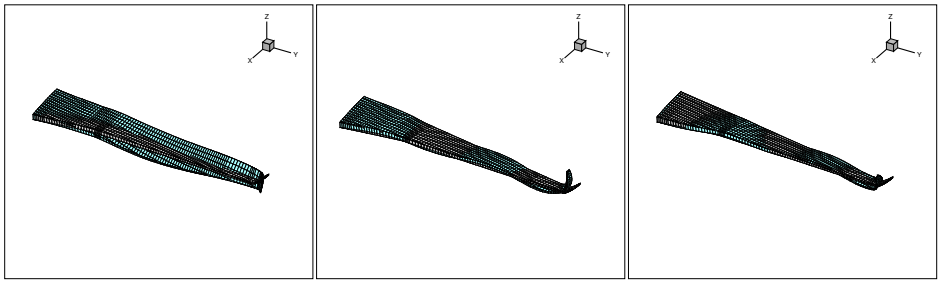

**(g)** Mode 7 **(h)** Mode 8 **(i)** Mode 9

**Figure C.1:** First nine structural modes from $\mathbf{\Phi}$.

The first nine modes after the transformation in $\tilde{\mathbf{L}}$ via SVD are shown in Figure C.2 and are ordered by decremental singular value order.

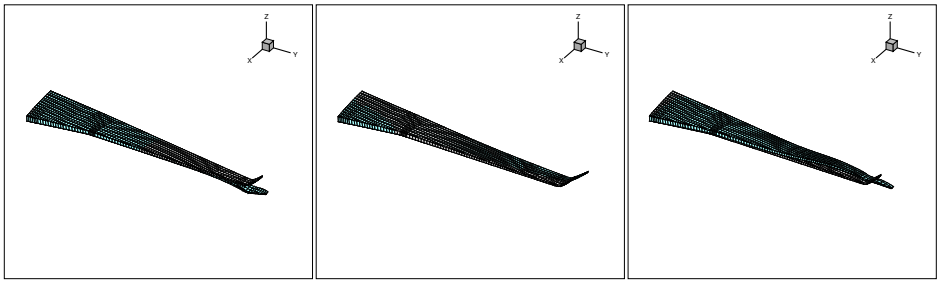

**(a)** Mode 1 **(b)** Mode 2 **(c)** Mode 3

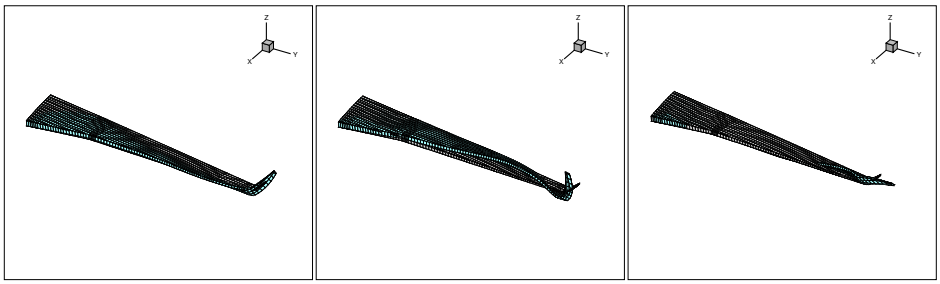

**(d)** Mode 4 **(e)** Mode 5 **(f)** Mode 6

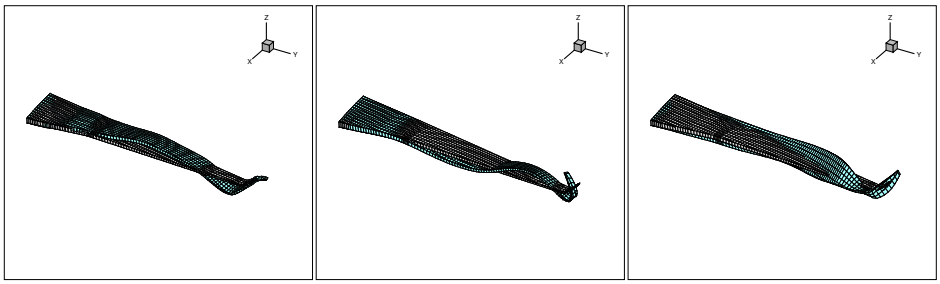

**(g)** Mode 7 **(h)** Mode 8 **(i)** Mode 9

**Figure C.2:** First nine structural modes from $\tilde{\mathbf{L}}$ ordered by decremental singular value order.

The first nine structural modes after PCA reduction ordered by decremental singular value order are shown in Figures C.3.

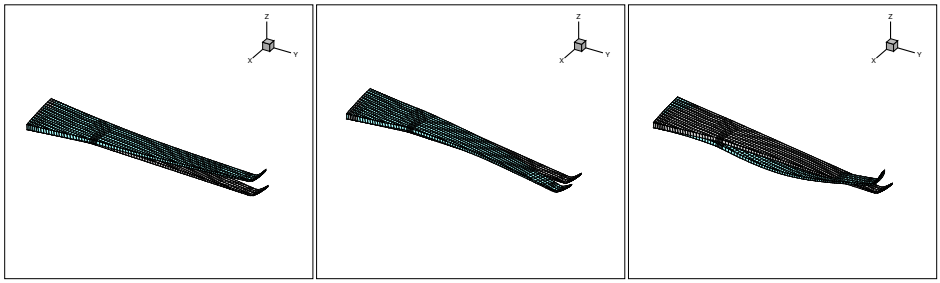

**(a)** Mode 1 **(b)** Mode 2 **(c)** Mode 3

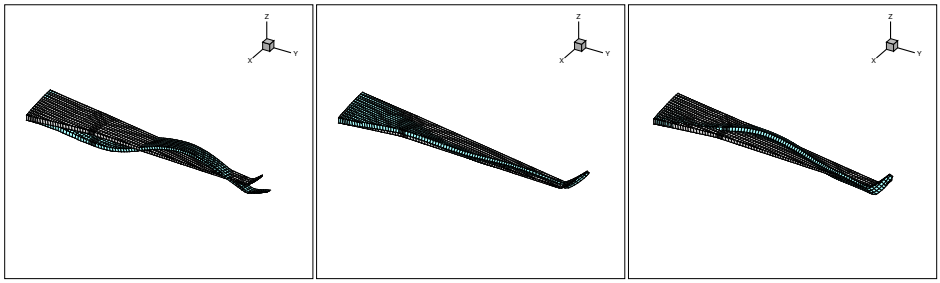

**(d)** Mode 4 **(e)** Mode 5 **(f)** Mode 6

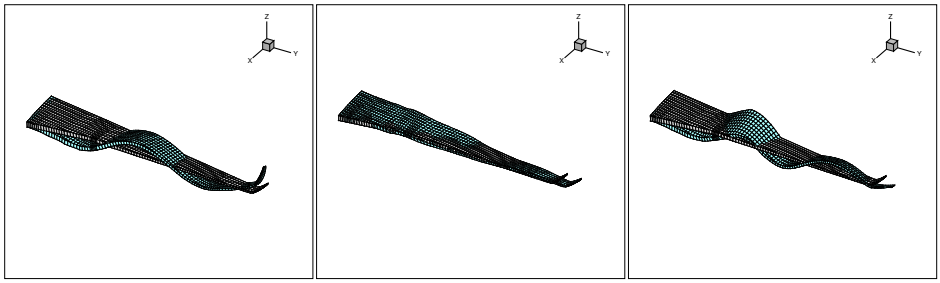

**(g)** Mode 7 **(h)** Mode 8 **(i)** Mode 9

**Figure C.3:** First nine structural modes after PCA reduction ordered by decremental singular value order.

# D

# OPTIMISATION RESULTS FROM CHAPTER 6

# D.1 BLENDED WING

## D.1.1 $C_D \leq 180.5$

### D.1.1.1 THICKNESS AND STIFFNESS DISTRIBUTION

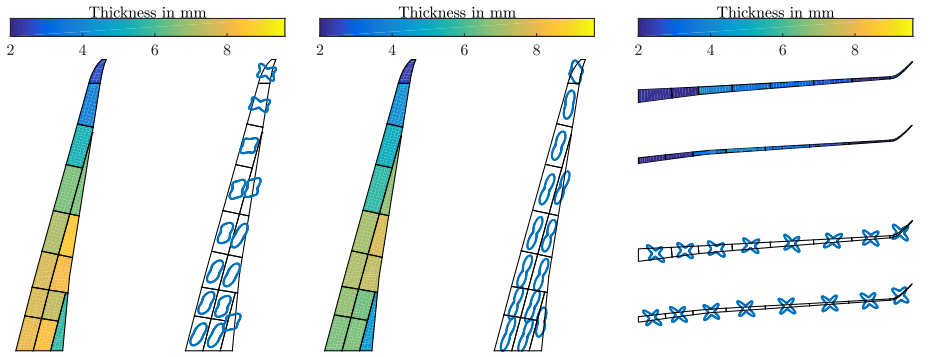


**(a)** Upper wing skin **(b)** Lower wing skin **(c)** Wing front and rear spars

**Figure D.1:** Wing thickness and stiffness distributions.

### D.1.1.2 CRITICAL MECHANICAL CONSTRAINTS AND LOAD CASES

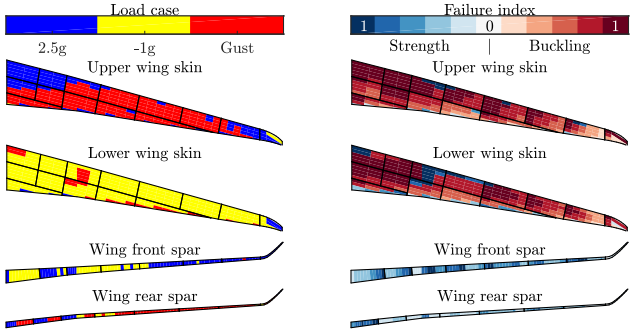


**(a)** Load-cases associated with the most active mechanical costraints at continuous optimum.

**(b)** Most critical failure index based on mechanical constraints at continuous optimum.

## D.1.2 $C_D \leq 182.5$

### D.1.2.1 THICKNESS AND STIFFNESS DISTRIBUTION

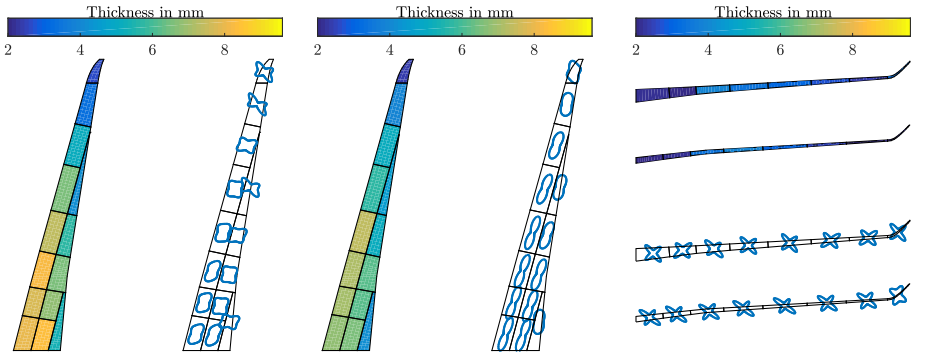


**(a)** Upper wing skin **(b)** Lower wing skin **(c)** Wing front and rear spars

**Figure D.3:** Wing thickness and stiffness distributions.

### D.1.2.2 CRITICAL MECHANICAL CONSTRAINTS AND LOAD CASES

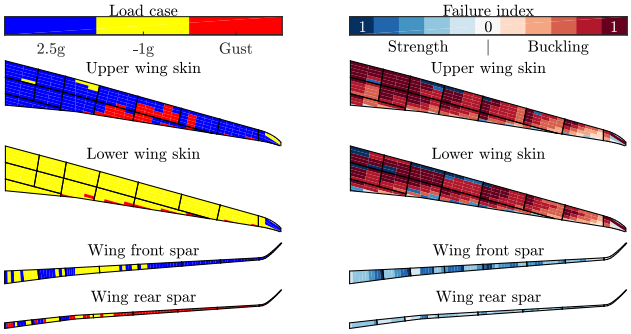


**(a)** Load-cases associated with the most active mechanical costraints at continuous optimum.

**(b)** Most critical failure index based on mechanical constraints at continuous optimum.

## D.1.3 $C_D \leq 184.5$

### D.1.3.1 THICKNESS AND STIFFNESS DISTRIBUTION

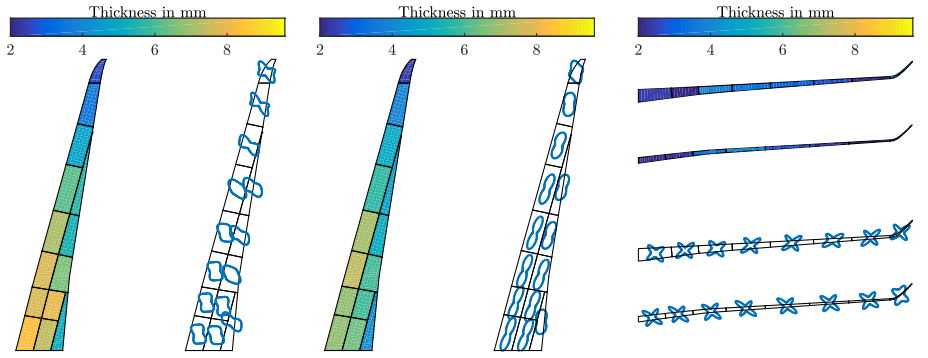


**(a)** Upper wing skin **(b)** Lower wing skin **(c)** Wing front and rear spars

**Figure D.5:** Wing thickness and stiffness distributions.

### D.1.3.2 CRITICAL MECHANICAL CONSTRAINTS AND LOAD CASES

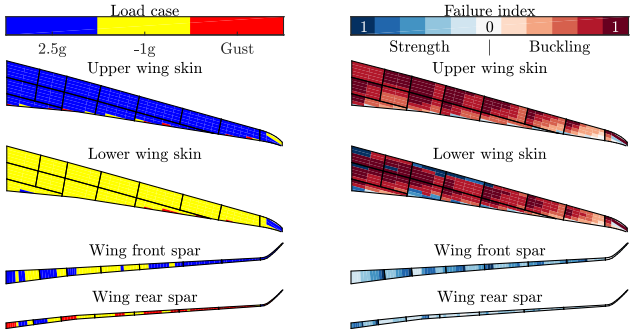


**(a)** Load-cases associated with the most active mechanical costraints at continuous optimum.

**(b)** Most critical failure index based on mechanical constraints at continuous optimum.

## D.1.4 $C_D \leq 188.5$

### D.1.4.1 THICKNESS AND STIFFNESS DISTRIBUTION

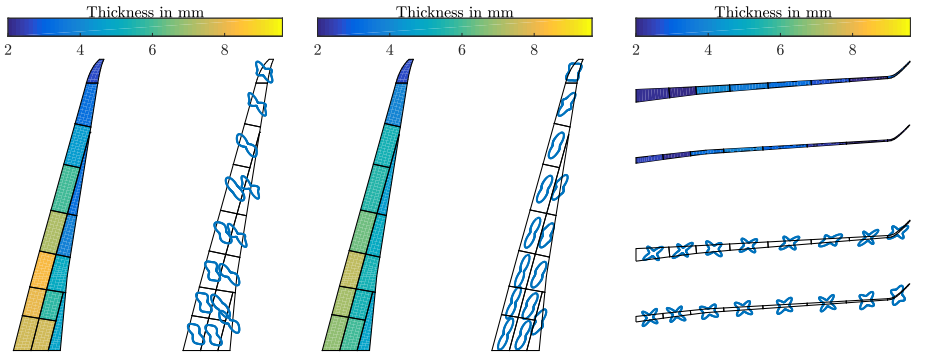


**(a)** Upper wing skin **(b)** Lower wing skin **(c)** Wing front and rear spars

**Figure D.7:** Wing thickness and stiffness distributions.

### D.1.4.2 CRITICAL MECHANICAL CONSTRAINTS AND LOAD CASES

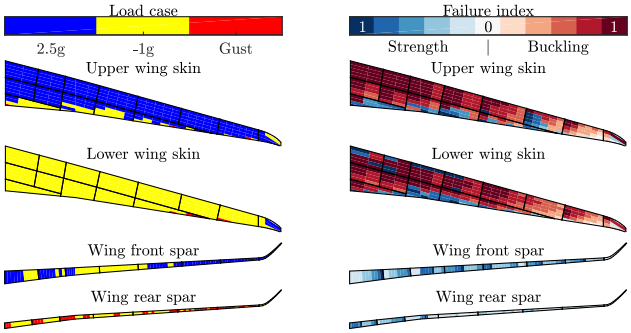


**(a)** Load-cases associated with the most active mechanical costraints at continuous optimum.

**(b)** Most critical failure index based on mechanical constraints at continuous optimum.

### D.1.5 SPANWISE VERTICAL DISPLACEMENT AND TWIST

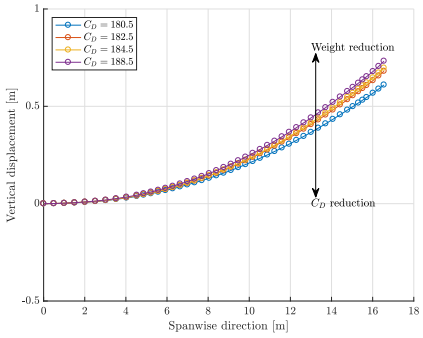


**(a)** Wing vertical displacement

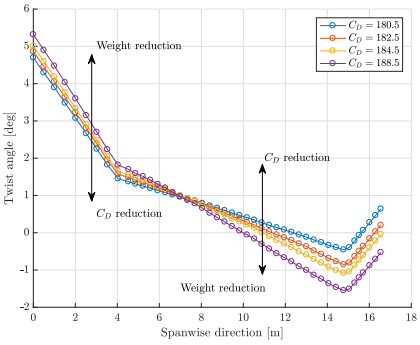


**(b)** Wing twist angle with respect to airstream

**Figure D.9:** Comparison between optimum obtained with blending constraints and with different contraints on $C_D$

# D.2 UNBLENDED WING

## D.2.1 $C_D \leq 180.5$

### D.2.1.1 THICKNESS AND STIFFNESS DISTRIBUTION

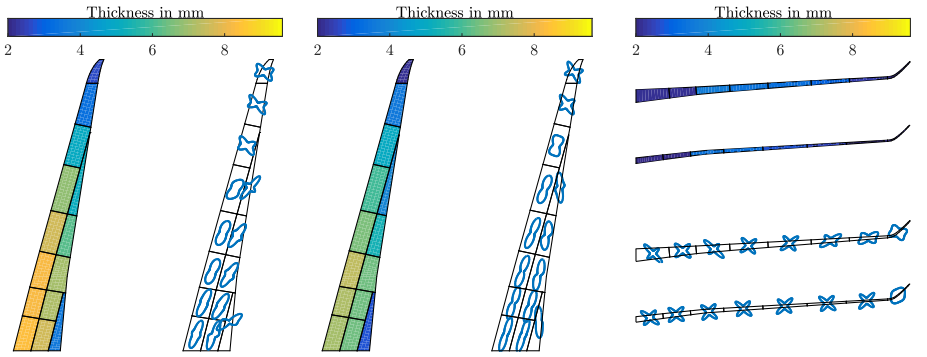


**(a)** Upper wing skin **(b)** Lower wing skin **(c)** Wing front and rear spars

**Figure D.10:** Wing thickness and stiffness distributions.

### D.2.1.2 CRITICAL MECHANICAL CONSTRAINTS AND LOAD CASES

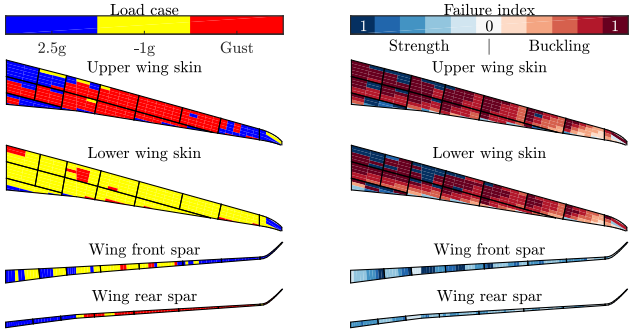


**(a)** Load-cases associated with the most active mechanical costraints at continuous optimum.

**(b)** Most critical failure index based on mechanical constraints at continuous optimum.

## D.2.2 $C_D \leq 182.5$

### D.2.2.1 THICKNESS AND STIFFNESS DISTRIBUTION

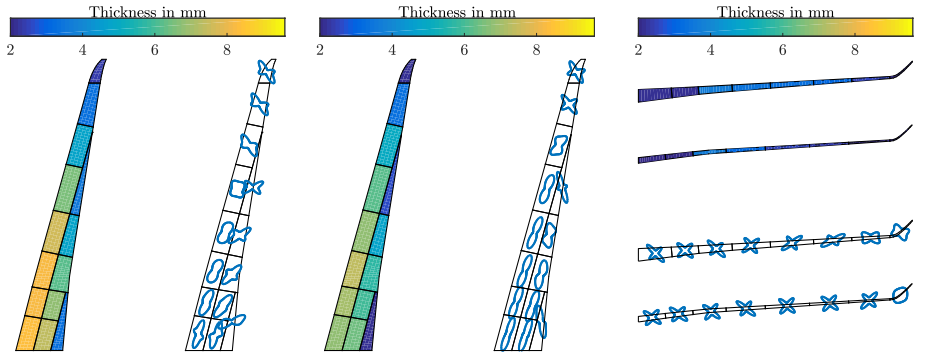


**(a)** Upper wing skin **(b)** Lower wing skin **(c)** Wing front and rear spars

**Figure D.12:** Wing thickness and stiffness distributions.

### D.2.2.2 CRITICAL MECHANICAL CONSTRAINTS AND LOAD CASES

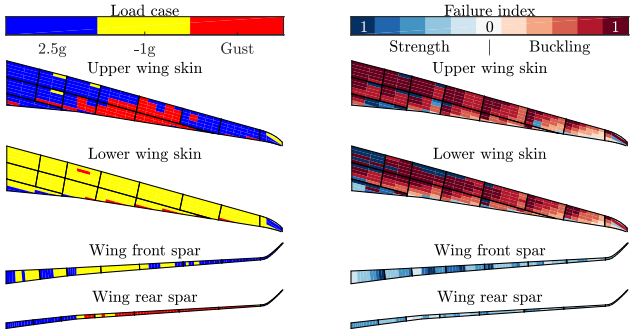


**(a)** Load-cases associated with the most active mechanical costraints at continuous optimum.

**(b)** Most critical failure index based on mechanical constraints at continuous optimum.

## D.2.3 $C_D \leq 184.5$

### D.2.3.1 THICKNESS AND STIFFNESS DISTRIBUTION

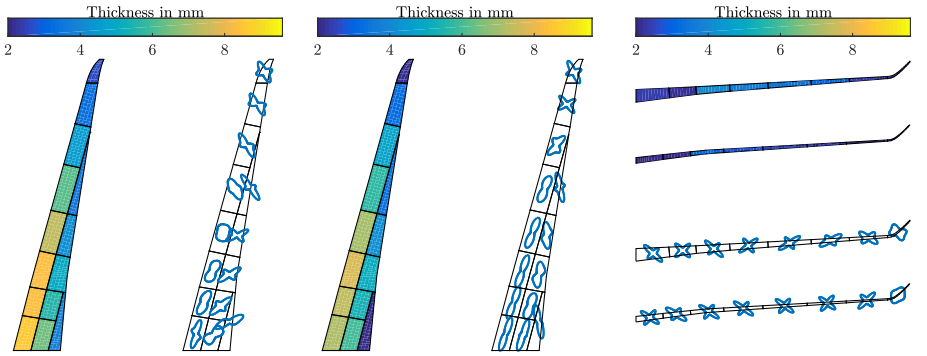


**(a)** Upper wing skin **(b)** Lower wing skin **(c)** Wing front and rear spars

**Figure D.14:** Wing thickness and stiffness distributions.

### D.2.3.2 CRITICAL MECHANICAL CONSTRAINTS AND LOAD CASES

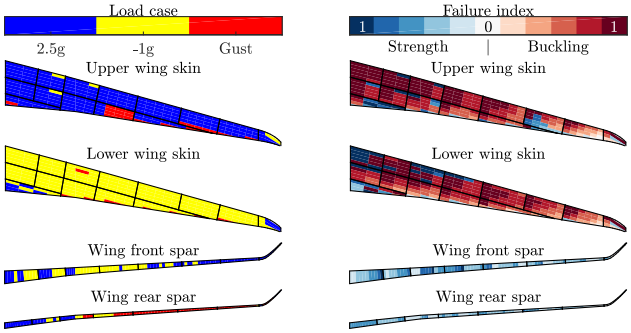


**(a)** Load-cases associated with the most active mechanical costraints at continuous optimum.

**(b)** Most critical failure index based on mechanical constraints at continuous optimum.

## D.2.4 $C_D \leq 188.5$

### D.2.4.1 THICKNESS AND STIFFNESS DISTRIBUTION

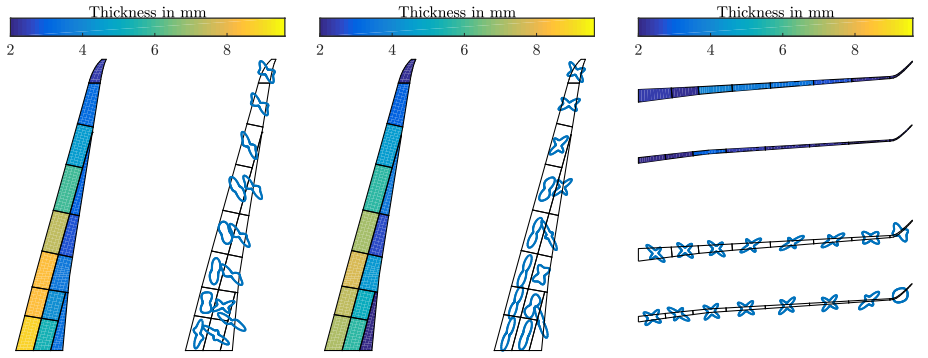


**(a)** Upper wing skin **(b)** Lower wing skin **(c)** Wing front and rear spars

**Figure D.16:** Wing thickness and stiffness distributions.

### D.2.4.2 CRITICAL MECHANICAL CONSTRAINTS AND LOAD CASES

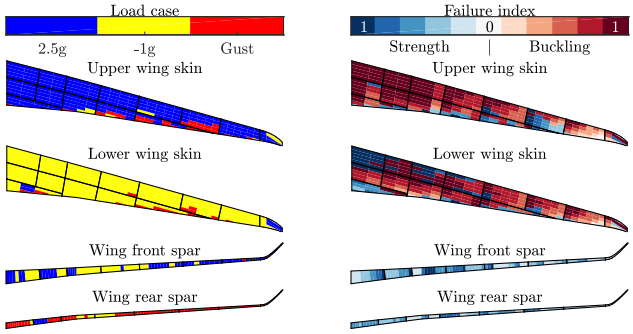


**(a)** Load-cases associated with the most active mechanical costraints at continuous optimum.

**(b)** Most critical failure index based on mechanical constraints at continuous optimum.

### D.2.5 SPANWISE VERTICAL DISPLACEMENT AND TWIST

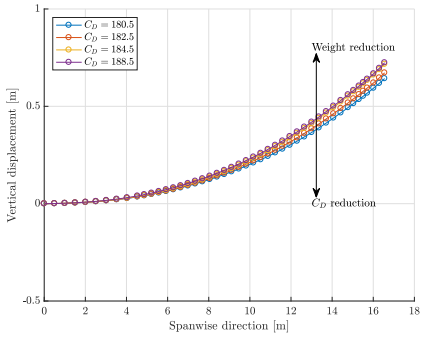


**(a)** Wing vertical displacement

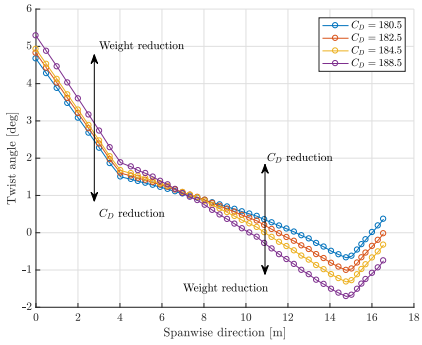


**(b)** Wing twist angle with respect to airstream

**Figure D.18:** Comparison between optimum obtained without blending constraints and with different contraints on $C_D$

# BIOGRAPHICAL NOTE

Marco Tito Bordogna was born on April 12, 1988, in Bergamo, Italy. He began his academic journey in aerospace engineering at the Politecnico di Milano, where he earned his Bachelors degree. Following this, he pursued a Master of Science in Mechanical Engineering, specializing in Lightweight Structures, at the KTH Royal Institute of Technology in Stockholm.

During his Masters studies, Tito undertook an internship at Airbus Defence and Space, which provided him with the first industry experience. His passion for aerospace engineering led him to TU Delft, where he embarked on a PhD in Aerospace Engineering. His research on aeroelastic tailoring is a collaboration between TU Delft and ONERA within the AMEDEO EU Marie Curie program.

Upon the completion of the bulk of his PhD work, Tito moved to Munich and started working as a Loads and Aeroelastic Engineer at Lilium eAircraft GmbH, where he is actively involved in the development of electric vertical takeoff and landing (eVTOL) aircraft. His role at Lilium allows him to apply his knowledge and expertise in aeroelasticity to a new aircraft achitecture.